MATHEMATICAL METHODS AND ALGORITHMS FOR IDENTIFICATION, TRACKING, AND QUANTITATIVE ANALYSIS IN CELLULAR BIOIMAGING

by

FATIMA ZERARI BOUKARI

A DISSERTATION

Submitted in partial fulfillment of the requirements
for the degree of Doctor of Philosophy in the
Mathematics and Physics Graduate Program
of Delaware State University

DOVER, DELAWARE
May 2017

This dissertation is approved by the following members of the Final Oral Review Committee:

Dr. Sokratis Makrogiannis, Committee Chairperson, Department of Physics and Engineering, Delaware State University
Dr. Fengshan Liu, Committee Member, Department of Mathematical Sciences, Delaware State University
Dr. Jinjie Liu, Committee Member, Department of Mathematical Sciences, Delaware State University
Dr. Yuri Markushin, Committee Member, Department of Physics and Engineering, Delaware State University
Dr. Luigi Ferrucci, External Committee Member, Scientific Director National Institute on aging, National Institutes of Health

DEDICATION

To the loving memory of my mother ...
May Allah (SWT) grant you El Jannah. Ameen

ACKNOWLEDGEMENTS

I would like to thank many people who have helped me through the completion of this dissertation. First, I will forever be thankful to my research advisor, Dr. Sokratis Makrogiannis. It has been an honor to be his first Ph.D. student. Over the years, he has taught me much. He provided scientific guidance and has given me a home in his Medical Imaging and VIsual Computing research lab (MIVIC). I am very grateful for his tremendous help and guidance. He is incredibly organized and a great problem solver, he has guided my progress with a keen eye for structure, reminding me of the main objective of the plan and putting me back on track whenever I get lost. With his encouragements and patience, this was very helpful in moving my project forward and reaching our goals. You will never know how much your advice and countless help has meant to me, from showing me new tricks, many insightful suggestions, new tools and ways about medical imaging and computer vision, which are extremely valuable to have my career move forward. I very much appreciate your enthusiasm, intensity and energy to do frequent meetings, offering incredibly timely advice, suggestions and feedback during the entire process. I am forever grateful and indebted to you and can never pay you back for all the help you have provided me. Without your expertise I would not have accomplished as much. I appreciate your help very much. It was an honor to be given the opportunity to work under your mentorship.

Second, I would like to thank my committee members: Dr Sokratis Makrogiannis, Dr Luigi Ferrucci, Dr Fengshan Liu, Dr Jinjie Liu and Dr Yuri Markushin who were more than generous with their interest, expertise, helpful comments and precious time. Thank you for agreeing to serve on my committee and for your contributions to this work.

I would like to extend my thanks to those who offered academic support over the years. I am deeply indebted to all the professors who helped shape my mind from elementary school to the university, thanks to Mme. Hardy Yvonne, Mr. Ballandras, Mr. Lecore et Mr. Denis and all the Delaware State University professors. The work in this dissertation was honored by all their teaching and guidance. Special thanks to all the teachers and professors, who encouraged me to dive into academia and believed in me, who helped set me on my current path, and continue to be an inspiration in my academic career. I Thank all those who taught me and who helped me to fall in love with Mathematics and Physics. I would like to thank all the amazing women in the graduate school office of DESU and all the members of the Optical Science Center for Applied Research (OSCAR) center and Mathematical sciences department who assisted me during this PhD process and were very patient with me when I lack knowledge about paperwork and procedures. I would also thank all the members of

security of DESU, because of them I have safely spent many nights working in the OSCAR facility on this dissertation.

I have been blessed with financial support during this graduate program at DESU, and wish to acknowledge and thank the support by the Center for Research and Education in Optical Sciences and Applications (CREOSA) in Delaware State University funded by NSF CREST-8763 and support by the National Institute of General Medical Sciences of the National Institutes of Health under Award Number SC3GM113754.

I deeply thank our MIVIC research group members and friends that I have had the pleasure to work with or alongside. I also thank my friends for providing support encouragement and friendship.

Although the PhD was my dream, there is nothing more important than my kids. PhD is a difficult and stressful process but Coming home and seeing my kids after a long day of research and writing kept me going when I wanted to give up. These past several years have not been an easy ride, both academically and personally. I especially thank my husband, Hacene, who has been a constant source of support and encouragement during the challenges of graduate school and life. Thank you for backing me up whenever I needed to and keeping me feel that I was still there for my family.

I especially thank my sisters and brothers who provided unconditional love and care. They are and have been my best friends all my life. I have the fortune to have them in my life and I am thankful to them for helping me when I needed it most, for all their advice, constant support and prayers. They have been there for me when the challenges of graduate school seemed too great to overcome. And most importantly I thank my dear parents, without whom none of this would have been possible, thank you for putting me through the best education possible, thank you for pushing me and helping me enjoy learning and taking new heights in life and for encouraging me to follow my dreams. I owe you an immeasurable debt of gratitude for the long, hard hours you worked throughout our youth to give me and my brothers and sisters the opportunity to follow our dreams, thank you for all of the tremendous love you have given us along the way.

Finally, A special thank to my father, Sidi, my eternal cheerleader, who makes everyone of us feel so special. He raised me with a love of science and supported me in all my dreams. His enthusiasm and love for learning is always my greatest inspiration and is the reason why I decided to go to pursue a career in research. Thank you Sidi...

Mathematical Methods and Algorithms for Identification, Tracking, and Quantitative Analysis in Cellular Bioimaging

Fatima Zerari Boukari

Faculty Advisor: Dr. Sokratis Makrogiannis

ABSTRACT

Automated cell segmentation and tracking enables the quantification of static and dynamic cell characteristics and is significant for disease diagnosis, treatment, drug development and several other domains in health and life sciences. The topic of this dissertation is the development of techniques for fully automated cell segmentation, tracking, lineage construction, and quantification. This work concentrates on two areas; cell segmentation and cell tracking.

We pursue a solution of the cell segmentation problem in the joint spatio-temporal domain to overcome weaknesses of previous works that operate only on the spatial domain of each frame. Here we propose a PDE-based formulation of spatio-temporal motion diffusion to detect the cell motion. In addition, we introduce an intensity standardization technique to address intensity variability complicating frame-to-frame analysis in differential techniques. To refine cell delineation accuracy produced by motion diffusion-based segmentation, we propose to use energy minimizing geometric active contours that assume a piece-wise constant image region model as a special case of the Mumford-Shah segmentation framework. Furthermore, we introduce temporal linking of the region-based level sets to allow for faster convergence and to resolve non-convexity that affects energy-based minimization that is typical in image analysis inverse problems.

In the cell tracking part of this work we first propose a variational method for joint local-global optical flow computation to estimate the cell motion. We utilize the predicted cell motion along with cell areas in a probabilistic Maximum Likelihood decision strategy assuming Markov dependency to find cell correspondences between consecutive frames. To perform track linking and to identify the cell states in the time-lapse sequence we find the solution that minimizes a global cost function defined over the set of all cell tracks by a heuristic approach. We represent cell tracks by an acyclic graph that we use to visualize the lineage tree. We use the region centroids to display the cell trajectories. Finally, we compute morphological, motility, diffusivity, and velocity measures using the time-lapse images, the cell label maps, and the tracking data.

We validate the cell segmentation and tracking stages both individually and as a joint system against reference standards that were manually generated. The image sequences and reference standards were obtained from a public database used for international cell tracking competitions. The validation measures quantify the region delineation accuracy by comparing levels of region overlapping and they calculate the cell tracking accuracy by comparison of acyclic graphs constructed from the cell tracks. The proposed techniques produce promising accuracy rates in comparison to the state-of-the-art. The ST-Diff-TCV segmentation technique yields an average DICE score of 89% over all 12 time-lapse image sequences. The automated tracking method using reference masks as input produces an average TRA score of 99%, which validates the tracking stage, and the fully automated system using both the proposed ST-Diff-TCV segmentation and tracking techniques produces an average of 89% with the 8 out of 12 sequences producing $TRA > 91\%$.

TABLE OF CONTENTS

LIST OF TABLES

LIST OF FIGURES AND ILLUSTRATIONS

LIST OF ABBREVIATIONS

CDF	Cumulative Distribution Function
CLGOF	Combined Local-Global Optical Flow
CNR	Contrast-to-Noise Ratio
CV	Chan and Vese
DM	Dissimilarity Measure
DSC	Dice Similarity Coefficient
E-L	Euler Lagrange
FLUO	Fluorescent
GAC	Geodesic Active Contours
GT	Ground Truth
IQ	Image Quality
KDE	Kernel Density Estimation
ML	Maximum Likelihood
MR	Magnetic Resonance
MSC	Mesenchymal Stem Cells
MSD	Mean Squared Displacement
MST	Minimal Spanning Trees
OAG	Oriented Acyclic Graph
OF	Optical Flow
PDF	Probability Density Function
PDE	Partial Differential Equation
PF	Particle Filter
SEG-GT	Ground Truth SEGmentation

SEG-GT-F	Ground Truth SEGmentation Function
SIM	SIMulated dataset
SKIZ	Skeletonization by Influence Zone
SNR	Signal to Noise Ratio
S-T	Spatio-Temporal
ST-Diff	Spatio-Temporal (Non Linear) Diffusion
ST-Diff-TCV	Spatio-Temporal Diffusion Temporally (Linked) Chan Vese
TCV	Temporally (Linked) Chan-Vese
TRA	TRAcking
TRA-GT	TRAcking Ground Truth
TRA-GT-F	TRAcking Ground Truth Function

Chapter I: INTRODUCTION

1.1 Cell Segmentation and Tracking

Studies of living organisms in biology and medicine require the analysis of their static and dynamic properties. Advances in imaging technologies have enabled the acquisition of time-lapse sequences of 2D and 3D data at the cellular and molecular level. Research in medicine and biology has become increasingly dependent on this type of imaging data [49] because it can be used to extract information about cell metabolism, growth, reaction to stimuli, and reproduction [113].

The quantitative analysis of time-lapse microscopy images is a key for detection of disease patterns and can be used in decision making to make a reliable diagnosis. Research in pathology is a very significant step for diagnosis of a large number of diseases including most cancers. Noninvasive cellular imaging allows the tracking of grafted cells as well as the monitoring of their migration, suggesting potential applications to track both cancer and therapeutic stem cells. Cell-based therapy holds great promise for cancer treatment. The ability to non-invasively track the delivery of various therapeutic cells (e.g. T-cells and stem cells) to the tumor site, and subsequent proliferation of these cells, would allow better understanding of the mechanisms of cancer development and intervention. Moreover data collected from individual patients at the anatomical, cellular and molecular levels, offer unprecedented possibilities to design personalized therapies.

Studies of disease mechanisms are valuable for clinical research areas such as stem cell research, tissue engineering, drug discovery, genomics, and proteomics. Morphological changes correlate with disease progression. Study of cell lineage relationships is significant for stem cell research, and disease etiology and progression studies [16, 63]. The statistical analysis of the tracking measurements will assist researchers to more precisely track the genetics of individual cells and detect and understand cell behavior and abnormalities.

High content screening applications in drug discovery require the automated monitoring of cell populations in a high-throughput experiment [1]. These applications depend on accurate cell tracking of individual cells that display various behaviors including mitosis, merging, rapid movement, and entering and leaving the field of view.

Quantitative analysis includes the study of cell morphometry, such as the cells' shape and their dynamic characteristics in a sequence such as the cell lifetime, motility, number of divisions, and morphological changes with time among other characteristics. Cell quantitative analysis consists of the following main stages: cell detection, cell delineation, cell tracking, cell event detection, and construction of cell lineage tree. Cell detection is the localization and identification of the cell in the image sequence. Cell delineation also called segmentation is the process of finding the boundaries of the cell and defining the cell region. Cell tracking is the process of identifying the cells in all frames of the sequence. After cell tracking is completed, we can follow the cells and identify cell events such as migration, mitosis, apoptosis, and new cells entering the field of view. After finding all cell events we can construct the cell lineage tree that stores and visualizes the cell events. Finally we given the cell identifiers and tracking results, we can calculate and visualize cell characteristics and their evolution with time.

1.2 Motivation and Open Problems

The data size of a single cell image sequence is typically in the range of hundreds of megabytes. Diagnosing a disease after manually analyzing numerous data requires intensive and laborious work and long time. Furthermore, manual analysis is dependent on the level of experience of the human operator, and is almost certainly non-reproducible. As a consequence, the use of automatic analysis and quantification can significantly improve the reproducibility, efficiency, and accuracy of quantitative analysis, and overall benefit the patient.

The tasks of automatic cell detection, segmentation, and tracking in time-lapse fluorescent microscopy images pose a difficult problem due to high variability in images because of numerous factors like differences in slide preparation (fluorescent concentration, presence of foreign artifacts, time to prepare the sample, and time between each time lapse image for the same sample, etc) and image acquisition (corruption by different types of noise, specific features of the microscope such as resolution and contrast limitations, etc). To be able to capture fluorescent microscopy images and observe live cell processes, like cell migration apoptosis and proliferation, light exposure is kept minimal to reduce the photodamage, but this reduces the image quality [80, 50, 52].

The aim of this work is to develop automated methods that successfully detect and track cells enabling the analysis of their static and dynamic behavior including cell morphology, cell migration, and changes in cell states (mitosis and apoptosis, for example). To reach these objectives we introduce automated techniques for cell detection, segmentation, tracking, construction of lineage trees of progenitor cells, and cell quantification.

1.3 Background

Cell tracking methodologies involve the tasks of preprocessing, cell segmentation and motion tracking [128, 133, 65, 81, 30, 77, 51]. In this context, segmentation of cells is a particularly challenging task that has a direct impact on the overall quantification process. Image segmentation is a popular field in the domain of image analysis. More specifically, parametric [61] and nonparametric active contour models [75, 38, 48, 87] have been widely used in development of bio-imaging and biomedical image analysis techniques. An interesting aspect in cell analysis methods is the relation between image quality and segmentation accuracy. Many segmentation methods address certain types of datasets; however, for low-quality images and different cell types and shapes, the same methods may yield varying levels of performance.

Cell tracking approaches can be categorized into (i) tracking by detection [129, 2, 56,

65, 32, 72, 106, 12] and (ii) tracking by model evolution [136, 135, 84, 47, 66, 90, 46, 48, 65]. Tracking by detection methods consist of two separate stages; cell segmentation and data association. Cell segmentation is accomplished by image segmentation techniques that we briefly mentioned before. The data association stage involves cell matching and track linking that can be accomplished by probabilistic techniques. Model evolution techniques integrate the stages of segmentation and data association into a joint model that represents the cell regions and their evolution with time. In this framework topological changes may account for cell events. The models are frequently implemented using parametric or geometric active contour models.

1.4 Main Points of Contribution

Overall one may argue that many approaches to cell tracking have been developed in the past, but most are focused on the same type of optical imaging techniques, require extensive post-processing, and are parameter intensive. We propose a method to overcome these challenges to achieve high level of accuracy in these different cases. The key contributions of this dissertation can be grouped as follows:

1.4.1 Cell segmentation

Intensity Standardization to address variability and differences in SNR and CNR In order to obtain more stability in parameter choice, we apply a histogram transformation approach to match the reference background threshold from the intensity distribution of each three consecutive frames to an intensity distribution model learned from all frames of the sequence during the training stage. After this step, each video sequence frame is scaled and transformed into a sequence with background with same order of magnitude for a more robust and a less sensitive parameter choice method.

Spatio-temporal motion diffusion Building upon previous ideas for estimating motion activity using spatio-temporal diffusion [73], here we develop and utilize a heat flow

analogy model in the joint spatio-temporal domain and combine this process with a region-based level-set optimization approach for cell segmentation of images obtained by fluorescence microscopy. Spatial and temporal motion parameters of our model are estimated for each dataset and an optimal Parzen bandwidth parameter is experimentally determined for density estimation of edges and outliers in each dataset. High activity regions are initially detected by solving numerically a system of coupled spatio-temporal nonlinear partial differential diffusion equations on three consecutive frames [10].

Temporally linked level-sets for faster convergence We propose to use the moving delineation curve as an initial level-set to be refined using a region-based process for final segmentation. We validated the joint approach denoted by ST-Diff-TCV [9] over a set of sequences against reference data and compared the segmentation accuracy of the joint spatio-temporal and level-set technique with results derived from Chan-Vese (CV) segmentation [28], a temporally linked level set method that we presented in [11] denoted by TCV, and spatio-temporal diffusion based segmentation only (ST-Diff).

Spatio-temporal cell detection and segmentation advantages An additional contribution of this work is that it can detect and segment newly appearing cells and cells that are hardly detectable using only first order statistical information. This method allows to detect cells that were impossible to detect using the region based CV segmentation because the optimization criterion is defined by the mean intensity inside and outside the level set defined moving curve. Hence, cell regions with low intensity values are considered as part of the background, and the region competition process fails to delineate these cells. However, these regions are detected by the spatio-temporal motion detection method because they are rather detected by their high activity process than by their intensity value, then refined by TCV model to detect the cell boundaries more accurately.

1.4.2 Fully Automated Tracking using Joint Local-Global Optical Flow and Probabilistic Cell Correspondence Measures

Our system automatically constructs the lineages of proliferating migrating cells. Cell lineage is a critical and required step in stem cell research [63]. In addition, division patterns can be correlated with changes in gene expression, and gene mutation. We can trace the roots of manual cell lineage construction techniques in the 19th century. However manual analysis can be a very laborious task with increasing number of cells and time frames. Therefore automated cell lineage construction is very useful as it will enable the use of very large volumes of data for analysis. Dealing with overlapping and clustered cells is a challenge in the case of dense datasets. This creates many errors like false negatives, false positives, false splitting operations and creates lineage tree edges with incorrect semantics. Thus, separating falsely clustered cells is crucial for improving tracking accuracy. In the pre-tracking stage, we propose to use the watershed transform on the Euclidean distance map produced by the segmented cells and then apply the H-minima transform for minima reconstruction to separate overlapping and clustered/touching cells. We also investigate the use of the solidity measure to estimate the number of fused cells. In the main tracking stage we introduce a variational method for joint local-global optical flow computation to estimate cell motion. We utilize the predicted cell motion in a probabilistic Maximum Likelihood Bayesian decision framework assuming Markov dependency to find cell correspondences between consecutive frames. To perform track linking and to identify the cell states in the time-lapse sequence, we find a solution that minimizes a global cost function given cell neighborhood constraints defined over the set of all cell tracks. The proposed system is applicable to varying cell shapes, types, and densities and image sequences of reduced image quality.

1.4.3 Cell Quantification

Our method produces measurements of static cell attributes including area, shape, intensity and their changes with time. Moreover it measures cell centroid localization, cell lifetime, mitosis and apoptosis events. Then it calculates cell motility, diffusivity, and velocity measures. Our methodology constructs an acyclic graph that represents cell tracks, and enables visualization of the lineage tree, quantification of cell events, and detection of potential behavioral anomalies. Overall, this system enables accurate quantitative analysis of cell events, and provides a valuable tool for high-throughput biological studies.

1.5 Dissertation Structure

In Chapter II, we review the previous work in the areas of image segmentation including region-based and model-based segmentation and cell tracking including the tracking by detection and model evolution groups of methods. In Chapter III, we describe the proposed cell segmentation methodology using spatio-temporal motion diffusion, intensity standardization, and temporally linked level sets. In Chapter IV, we report experiments and validate the results produced by our cell segmentation methodologies against manual segmentations. We also discuss our findings and compare the tested methods. Chapter V introduces the cell tracking methodology and the stages of motion prediction, cell matching and cell event detection, and construction and visualization of the cell lineage tree. In Chapter VI, we report results produced by the tracking technique using reference or automated segmentation and validate our results against manually annotated cell tracking and we discuss these results. Furthermore, we include visualizations of the identified cell trajectories and quantification measures. Finally, Chapter VII summarizes the key findings of this research, and provides insight into the applicability of the developed approaches.

Chapter II: CELL SEGMENTATION AND TRACKING BACKGROUND

2.1 Background on Image Segmentation

Cell segmentation is a very important topic in computer vision and image analysis. The goal of image segmentation is to partition a given image into its objects, or to find boundaries of objects. Cell segmentation techniques can be widely categorized into region-based, model-based, and statistical methods. In Figure 2.1 we display the image segmentation taxonomy that we will will discuss in this chapter.

2.1.1 Region-based Methods

Watershed Algorithm

Watershed segmentation is based on topographic concepts and mathematical morphology. It visualizes an image in 3 dimensions: an edge map in two dimensions versus intensity representing the altitude of the topographic surface. We next give the basic terminology for elements used in watershed transform description [121, 111, 55, 83].

Definition 2.1.1 (Gradient minima)**.** The points of regional minimum gradient magnitude of a topographic surface are called *gradient minima*.

Definition 2.1.2 (Catchment basin)**.** The set of points from which, a drop of water would fall to the same minimum, is called a *catchment basin*. Hence, points that fall to the same minimum are grouped together to form the same region.

Definition 2.1.3 (Watershed line)**.** Set of points from which, a drop of water would fall to more than one catchment basin. At these points a dam is built forming a crest line or a *watershed line*.

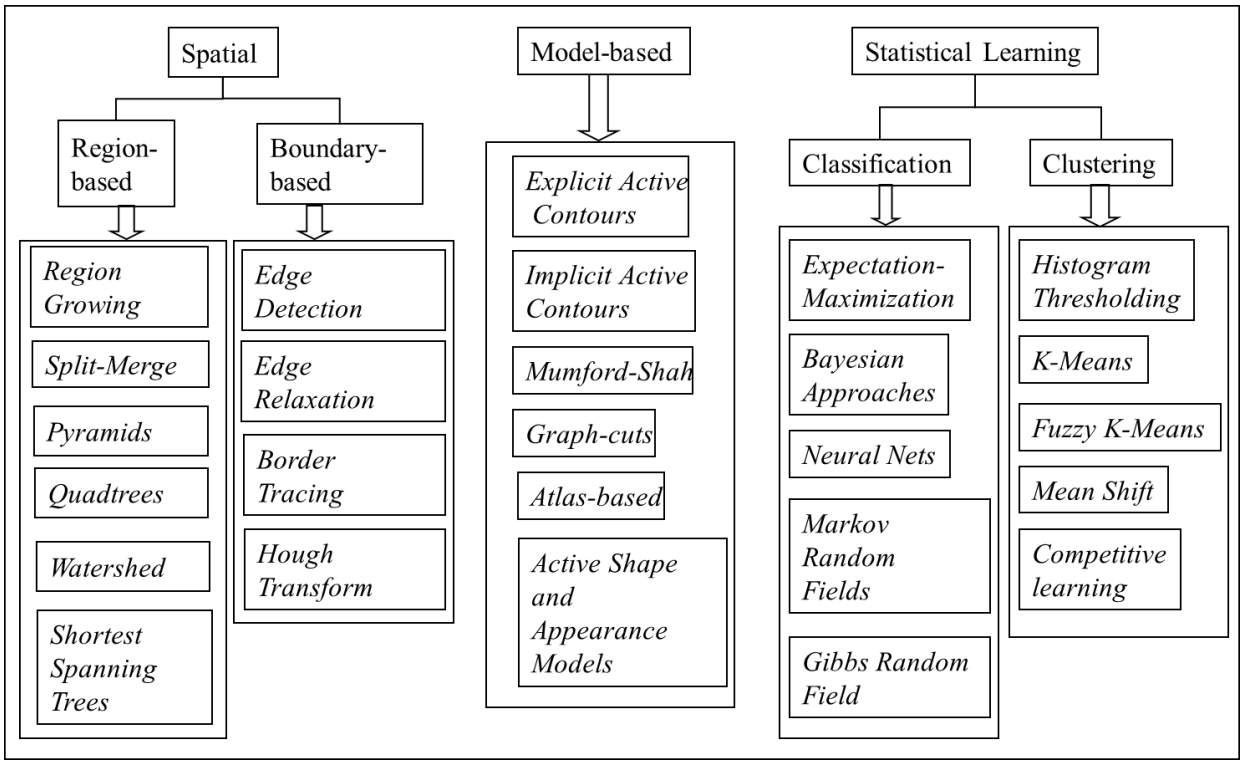

Figure 2.1: Image segmentation taxonomy.

Definition 2.1.4 (Image Gradient)**.** The gradient of an image, defined by intensity function $f(x, y)$ at each image point is a $2D$ vector with the components given by the derivatives in the 2-dimensional domain. At each image location, the gradient vector points to the direction of largest possible intensity increase, and the length of the gradient vector corresponds to the rate of change in that direction. The gradient of an image is given by [55]:

$$\nabla f = \begin{bmatrix} f_x \\ f_y \end{bmatrix} = \begin{bmatrix} \frac{\partial f}{\partial x} \\ \frac{\partial f}{\partial y} \end{bmatrix}, \tag{2.1}$$

where $\frac{\partial f}{\partial x}$ and $\frac{\partial f}{\partial y}$ are the gradients in the x and y directions respectively. The gradient

magnitude $|\nabla f(x,y)|$ and gradient direction ψ are calculated by [83]

$$|\nabla f(x,y)| = \sqrt{\left(\frac{\partial f}{\partial x}\right)^2 + \left(\frac{\partial f}{\partial y}\right)^2} \tag{2.2}$$

$$\psi = tan^{-1}\left[\frac{f_y}{f_x}\right]. \tag{2.3}$$

Considering an image as a topographic surface, the watershed algorithm can be visualized as a flooding process. It starts from the minima of the surface, called *markers*, then finds a path between each pixel of the image and a local minimum. During flooding, valleys called *catchment basins*, are filled with water. When regions belonging to different *catchment basins* are about to merge, dams representing watershed lines are erected between the basins. The watershed lines separate the different regions and produce the segmentation result.

Many watershed algorithms have been suggested in the literature [111]. The first algorithms were developed for elevation models. There are two main techniques for watershed: (i) sorting and flooding, and (ii) gradient following. Sorting and flooding typically construct ordered queues of the image pixel spatial coordinates that are connected to a minimum and sorted by the image gradient. Gradient following methods utilize steepest descent algorithms to determine the paths between image pixels and the gradient minima.

In cell segmentation applications, the watershed algorithm is found to sensitive to noise, and works well for cell regions with very low intensity gradients inside the cells. Otherwise, we may end up with the effect of over-segmentation due to the excessive number of regional minima.

2.1.2 Model-based Methods

These methods propose and use mathematical and physical models to partition an image [39, 85, 61, 134, 127, 130, 64, 28, 120, 86, 76, 74]. The models may evolve by minimizing and energy functional using variational methods, or may be represented directly by PDEs

in which case the solution corresponds to the steady state of the system.

Mumford Shah

In [39, 85], Mumford and Shah formulated an energy minimization problem that allows to compute optimal piecewise-smooth approximations f of a given image f_0 on the image plane Ω. Let $\Omega \subset \mathbb{R}^D$ the image domain of D dimensions and $f : \Omega \to \mathbb{R}$. We assume that Ω is open and bounded. The Mumford Shah formulate segmentation as a solution (f, C) of a piecewise constant function f corresponding to regions R_i and boundaries $C \subset \Omega$ by minimizing the energy functional $\mathcal{E}$

$$\mathcal{E}(f,k) = \int_{\Omega - C} (f - f_0)^2 d\vec{\omega} + \alpha \int_{\Omega - C} |\nabla f|^2 d\vec{\omega} + \beta \int_C d\vec{\omega}, \tag{2.4}$$

where α, β are nonnegative constants and $\int_C d\vec{\omega}$ is total contour length. This approach maximizes the homogeneity inside the segmented regions based on the intensity values.

Even though the Mumford Shah functional can formulate partitioning of an image into disjoint regions and contours, it presents some applicability difficulties. More specifically, it is not differentiable for suitable norms, therefore we cannot use Euler-Lagrange. Also, discretization of the unknown region boundary set may be particularly complicated. Therefore approximations of the functional $\mathcal{E}$ may be utilized to find a solution. The main approximation techniques are by (i) elliptic functionals [4, 3, 104], (ii) introducing second order singular perturbations [15, 13, 21, 23, 22], (iii) introducing nonlocal terms [14], and (iv) using of finite difference methods [27, 26].

The elliptic functional F_ϵ converging to Mumford-Shah energy $\lim_{\epsilon \to 0} \mathcal{E}_\epsilon = \mathcal{E}$ was proposed in [4, 3] and is given by:

$$\mathcal{E}_\epsilon = \int_\Omega (f - f_0)^2 d\vec{\omega} + \int_\Omega v^2 |\nabla f|^2 d\vec{\omega} + \int_\Omega \left(\epsilon |\nabla v|^2 + \frac{1}{4\epsilon}(v-1)^2 \right) d\vec{\omega}, \tag{2.5}$$

where $v(\vec{\omega}) \approx 0$, if $\vec{\omega} \in C$ and $v(\vec{\omega}) \approx 1$, if $\vec{\omega} \notin C$.

Also, specific solutions for the piecewise constant case have been proposed in [29, 28, 116] that we will describe in the next chapter.

Active contour methods

Active contour models are physics-based models that incorporate shape, image-based and external energy terms to delineate image objects. The active contour model deforms under the above energy terms until it reaches equilibrium. They typically seek to minimize an energy functional [90]. In active contour models the contour can be explicitely represented by a parametric curve, as in Snakes [61], or by an implicit representation as in level sets [103, 75, 118, 38, 37].

Parametric Active Contour Models - Snakes

The concept of Snakes introduced by [61], is an energy minimizing active contour model. In general, this technique uses a spline that is deformed by constraints and image forces to match the contours of an object in an image [61, 127, 130, 79, 41]. This method is robust to noise but cannot handle topological changes like merging or splitting of the contour. A snake is represented by a parametric curve

$$v(s) = \sum_{i=0}^{n-1} a_i B_I(s), \tag{2.6}$$

where s is the parameter of a control point on the contour, a_i are the coefficients and B_I are the base functions usually chosen to be splines of order n.

Energy functional

The proposed energy functional of the snake model included internal, image and prior knowledge-based terms.

$$E_{snake} = \int_0^1 (E_{internal}(v(s)) + E_{image}(v(s)) + E_{constraints}(v(s)))\, ds. \tag{2.7}$$

Internal energy

The internal energy term incorporates shape requirements for smoothness and elasticity.

$$E_{internal} = (\alpha(s)\,|v_s(s)|^2) + (\beta(s)\,|v_{ss}(s)|^2) = \left(\alpha(s)\left|\frac{dv}{ds}(s)\right|^2 + \beta(s)\left|\frac{d^2v}{ds^2}(s)\right|^2\right), \tag{2.8}$$

where $v(s) = (x(s), y(s))$ is the location vector of the control point s, and $\alpha(s)$ and $\beta(s)$ are the smoothness and elasticity parameters, respectively.

Image-based Energy

This energy term is used to attract the active contour model toward specific image features such as lines, edges or corners:

$$E_{image} = w_{line}E_{line} + w_{edge}E_{edge} + w_{term}E_{term} \tag{2.9}$$

$$E_{line} = f(\vec{\omega}) \tag{2.10}$$

$$E_{edge} = -|\nabla f(\vec{\omega})|^2 \tag{2.11}$$

$$E_{term} = \frac{\partial \psi}{\partial n_R}. \tag{2.12}$$

So the goal is to minimize the energy J of a contour C,

$$\inf_C J(C) = \alpha \int_0^1 |C'(s)|^2 ds + \beta \int_0^1 |C''(s)|^2 ds - \lambda \int_0^1 g(|\nabla f_0(C(s))|) ds. \tag{2.13}$$

Euler-Lagrange condition for minimization

In variational techniques the energy functional minimizer is found by use of the Euler-Lagrange method summarized as follows:

$$\frac{d}{ds}E_{vs} - E_v = 0 \tag{2.14}$$

$$-\frac{d}{ds}\left[\alpha(s)\frac{dv}{ds}\right] + \frac{d^2}{ds^2}\left[\beta(s)\frac{d^2v}{ds^2}\right] + \nabla E_{ext}\left(v(s)\right) = 0. \tag{2.15}$$

We solve the above equation by assuming that the curve is also a function of time $v = v(s,t)$, setting an initial snake curve and evolving the curve by the following PDE until we reach a steady state $\frac{\partial v}{\partial t} = 0$.

$$\frac{\partial v}{\partial t} - \frac{\partial}{\partial s}\left[\alpha(s)\frac{\partial v}{\partial s}\right] + \frac{\partial^2}{\partial s^2}\left[\beta(s)\frac{\partial^2 v}{\partial s^2}\right] + \nabla E_{ext}\left(v(s)\right) = 0. \tag{2.16}$$

Implicit or geometric active contour models - level sets

Introduced by Osher and Sethian [112] for front propagation, the level set approach is an implicit method that involves curves and hypersurfaces. For image segmentation a 2D curve is embedded within a 3D surface. A curve that is modeled by a physical system evolves by minimizing an energy functional and/or by following a PDE. This is a sophisticated category of techniques that can incorporate intensity, shape and prior statistical knowledge using elegant mathematical techniques [62, 103, 75, 134, 118, 130, 64, 38, 37].

Let $C(\vec{\omega})$ be the boundary of regions in a segmentation problem, with $\vec{\omega} \in \Omega \subset \mathbb{R}^D$, where D is the image domain dimensionality. Let $\phi : \Omega \times T \to \mathbb{R}$ be a Lipshitz continuous

function with $\phi\left(\vec{\omega(t)}, t\right) = 0$, $\forall \omega \in C$. This effectively defines the level set function ϕ as

$$\begin{cases} \phi(x,t) > 0 & \forall x \in \Omega_O \\ \phi(x,t) = 0 & \forall x \in C \\ \phi(x,t) < 0 & \forall x \in \Omega_B, \end{cases} \tag{2.17}$$

where Ω_O is the domain of the object regions, Ω_B is the domain of the background region, and C is the previously defined region boundary set.

We assume that the variation of ϕ is 0:

$$\frac{\partial \phi}{\partial t} + \frac{\partial \phi}{\partial C}\frac{\partial C}{\partial t} = 0 \tag{2.18}$$

$$\Rightarrow \frac{\partial \phi}{\partial t} + \nabla \phi \frac{\partial C}{\partial t} = 0. \tag{2.19}$$

We can use ϕ to define the surface normal vector $\vec{N}$ as follows

$$\vec{N} = -\frac{\nabla \phi}{|\nabla \phi|}. \tag{2.20}$$

If $\phi > 0$ inside the regions and $\phi < 0$ outside of the regions, then $\vec{N}$ points outwards. The normal of the curve and its curvature can be determined directly from the level set function. An example showing a curve during evolution is displayed in in Figure 2.2. A propagating surface moving along the surface normal by mean curvature is governed by

$$\frac{\partial C}{\partial t} = V(\kappa)\vec{N}, \tag{2.21}$$

where $V(\cdot)$ is the speed term and κ denotes the curvature.

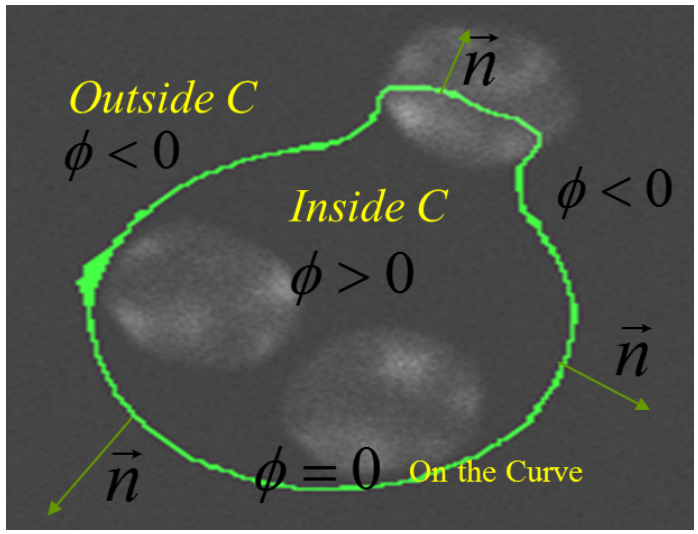

Figure 2.2: Example of a curve during evolution.

It follows that

$$\frac{\partial C}{\partial t} = -V(\kappa)\frac{\nabla\phi}{|\nabla\phi|}. \tag{2.22}$$

Then the level-set evolution PDE becomes

$$\frac{\partial \phi}{\partial t} + \nabla\phi\frac{\partial C}{\partial t} = 0 \tag{2.23}$$

$$\Rightarrow \frac{\partial \phi}{\partial t} + \nabla\phi\left(-V(\kappa)\frac{\nabla\phi}{|\nabla\phi|}\right) = 0 \tag{2.24}$$

$$\Rightarrow \frac{\partial \phi}{\partial t} - V(\kappa)\frac{\nabla\phi\cdot\nabla\phi}{|\nabla\phi|} = 0 \tag{2.25}$$

$$\Rightarrow \frac{\partial \phi}{\partial t} = V(\kappa)\frac{|\nabla\phi|^2}{|\nabla\phi|} \tag{2.26}$$

$$\Rightarrow \frac{\partial \phi}{\partial t} = V(\kappa)|\nabla\phi|. \tag{2.27}$$

Furthermore, curvature κ is given by

$$\kappa = \nabla\cdot\frac{\nabla\phi}{|\nabla\phi|}. \tag{2.28}$$

We can derive a formula for the calculation of ϕ using derivatives in the discrete domain.

Sethian Osher (front propagation)

An early approach to level set segmentation was the method of front propagation proposed in [103, 112]. Here because $V(\kappa) = \kappa$, the level set evolution is strictly guided by the mean curvature

$$\frac{\partial \phi}{\partial t} = |\nabla \phi| \left(\nabla \cdot \frac{\nabla \phi}{|\nabla \phi|} \right). \tag{2.29}$$

This level set does not include any image information and its result can be used as an initial solution for a more advanced level set technique.

Shape detection level sets

The authors in [75] propose to use an edge stopping function $g : \mathbb{R} \to \mathbb{R}$ applied to the intensities of the input image f_0 and solve the PDE

$$\frac{\partial \phi}{\partial t} = g(|\nabla f_0|)|\nabla \phi| \left(\nabla \cdot \frac{\nabla \phi}{|\nabla \phi|} + c \right), \tag{2.30}$$

where c is a constant force that can be used to drive the level set evolution towards one direction.

Geodesic active contours

Another popular level set method called Geodesic Active Contours (GAC) was proposed in [24]. This method seeks to find the path of minimum length

$$\inf_C J(C) = 2 \int_0^1 |C'(s)| g(|\nabla f_0(C(s))|) ds. \tag{2.31}$$

Using the level set formulation, this problem is equivalent to solving the following PDE

$$\frac{\partial \phi}{\partial t} = |\nabla \phi| \left(\nabla \cdot g(|\nabla f_0|) \frac{\nabla \phi}{|\nabla \phi|} + c g(|\nabla f_0|) \right). \tag{2.32}$$

2.1.3 Statistical Methods

Statistical methods typically treat image segmentation as a procedure for creating groups/clusters/classes of samples using algebraic or probabilistic measures of distances between samples, or groups of samples [45].

K-means Clustering

We can find the main regions of an image by applying clustering in the feature space of the pixel intensities. Often times we may include additional features computed from the image for multi-variate clustering. Then we can map the samples from the feature space back onto the image plane to obtain the label map.

K-means is an unsupervised method used to partition a set of n samples $\{\vec{x_i}, i = 1, \ldots, n\}$ where $\vec{x_i} \in \mathbb{R}^D$ and D is the dimensionality of the feature space into k clusters according to some defined distance measure DM, which is usually chosen to be the Euclidean distance. To cluster the data based on the distance of their intensities to the centroid or mean intensities, we need to minimize the objective function J:

$$J(W) = \sum_{j=1}^{k} \sum_{i=1}^{n} w_{ij} DM(\vec{x}_i, \vec{\mu}_j), \tag{2.33}$$

where $\vec{\mu}_j$, with $j = 1, 2, \ldots, k$ denote the k cluster centroids and $W = [w_{ij}]_{n \times k}$ is the cluster membership matrix with

$$w_{ij} = \begin{cases} 1, & \text{if } p = arg \min_j DM(\vec{x}_i, \vec{\mu}_j) \\ 0, & \text{otherwise.} \end{cases} \tag{2.34}$$

Let the dissimilarity measure DM be the Euclidean, that is

$$DM(\vec{x}_i, \vec{\mu}_p) = \|\vec{x}_i - \vec{\mu}_p)\|^2. \tag{2.35}$$

Then we can find the minimizing $\vec{\mu}_p$ by setting the derivative of J with respect to $\vec{\mu}_p$ to 0 and then the estimator becomes

$$\vec{\mu}_p = \frac{\sum_{i=1}^{n} w_{ip}\vec{x_i}}{\sum_{i=1}^{n} w_{ip}}. \tag{2.36}$$

The objective function J is first minimized with respect to w_{ij} and then it is minimized with respect to μ_p till convergence. The main steps of this technique are

Algorithm 1 K-means clustering

Require: Input image samples x_i, number of clusters k

1: Initialize cluster centroids μ_j, $j = 1, 2, \ldots, k$ (usually by random seeding within the variables' range)
2: **repeat**
3: Compute distances $DM(\vec{x_i}, \vec{\mu}_j), \quad i = 1, \ldots, n \quad j = 1, 2, \ldots, k$
4: Assign samples to closest centroid $n = arg\min_j DM(\vec{x}_i, \vec{\mu}_j)$
5: Compute objective function $J(W) = \sum_{j=1}^{k}\sum_{i=1}^{n} w_{ij} DM(\vec{x}_i, \vec{\mu}_j)$
6: **until** There is no change between the current and previous values of J.
7: **return** Labeled image samples (pixels) $l_i = x_i$

The objective function will decrease at each iteration, therefore the algorithm will surely converge. However, it may find a local minimum depending on its initialization and the difficulty of optimization.

Mean shift

Kernel density estimation (KDE)

Finds points with high density in the feature space. To find this high density location, we use a non parametric density estimator by kernel functions. The analogy is that in a continuous function, we move to the optimum by following the gradient descent and converge to a stationary point where the gradient is close to zero. The kernel density estimator of an

unknown density function f is defined as

$$\hat{f}(x) = \frac{1}{nh^d} \sum_{i=1}^{n} \mathcal{K}_{\langle}(x - x_i) \tag{2.37}$$

$$= \frac{1}{nh^d} \sum_{i=1}^{n} \mathcal{K}\Big(\frac{x - x_i}{h}\Big), \tag{2.38}$$

where $\mathcal{K}$ is the kernel and h is a positive value parameter called the bandwidth. Among the different choices of kernels uniform $\Big(\mathcal{K}(u) = \frac{1}{2}\,\mathbf{1}_{\{|u|\leqslant 1\}}\Big)$, biweight$\Big(\mathcal{K}(u) = \frac{15}{16}(1 - u^2)^2\,\mathbf{1}_{\{|u|\leqslant 1\}}\Big)$, triweight $\Big(\mathcal{K}(u) = \frac{35}{32}(1-u^2)^3\,\mathbf{1}_{\{|u|\leqslant 1\}}\Big)$, Silverman $\Big(\mathcal{K}(u) = \frac{1}{2}e^{-\frac{|u|}{\sqrt{2}}}\cdot\sin\left(\frac{|u|}{\sqrt{2}} + \frac{\pi}{4}\right)\Big)$ or Epanechnikov, where $\mathbf{1}_{\{|u|\leqslant 1\}}$ is the indicator function:

$$\mathbf{1}_{\{|u|\leqslant 1\}} := \begin{cases} 1 & \{|u| \leqslant 1\}, \\ 0 & \{|u| > 1\}. \end{cases} \tag{2.39}$$

For the mean shift technique [31, 43, 128, 129], we choose to use the Epanechnikov kernel because it presents the lowest mean square error defined as

$$\mathcal{K}(u) = \frac{3}{4}(1 - u^2)\,\mathbf{1}_{\{|u|\leqslant 1\}}. \tag{2.40}$$

The regional maxima of the density estimation are located at $\nabla\hat{f} = 0$, where

$$\nabla\hat{f}(x) = \frac{2c}{nh^{d+2}} \sum_{i=1}^{n} (x - x_i)\mathcal{K}'\left(\left|\frac{x - x_i}{h}\right|^2\right) \tag{2.41}$$

$$= \frac{2c}{nh^{d+2}} \sum_{i=1}^{n} g\left(\|\,(x - x_i)\,/h\|^2\right)\left(\frac{\sum_{i=1}^{n} x_i \cdot g\left(\|\,(x - x_i)\,/h\|^2\right)}{\sum_{i=1}^{n} g\left(\|\,(x - x_i)\,/h\|^2\right)} - x\right), \tag{2.42}$$

where $g(r) = \mathcal{K}'(r)$.

The mean shift vector $m(x)$ is

$$m(x) = \frac{\sum_{i=1}^{n} x_i \cdot g\left(\left\| \left(x - x_i\right)/h \right\|^2\right)}{\sum_{i=1}^{n} g\left(\left\| \left(x - x_i\right)/h \right\|^2\right)} - x. \tag{2.43}$$

The locations for density estimation are updated as

$$y_{j+1} = \frac{\sum_{i=1}^{n} x_i \cdot g\left(\left\| \left(y_j - x_i\right)/h \right\|^2\right)}{\sum_{i=1}^{n} g\left(\left\| \left(y_j - x_i\right)/h \right\|^2\right)}. \tag{2.44}$$

In [35] the authors proved the following theorem of converge:

Theorem 2.1.5. *If the kernel $\mathcal{K}$ has a convex and monotonically increasing profile, the sequences $\{y_j\}$, $j = 1, 2, \ldots$ and $\{\hat{f}(y_j)\}$, $j = 1, 2, \ldots$ both converge, and $\{\hat{f}(y_j)\}$ increases monotonically.*

The estimation converges to a local maximum of the probability density function that is the density mode, because the magnitude of mean shift vector converges to zero.

Mean shift segmentation is completed in the following steps:

Algorithm 2 Mean shift clustering

Require: Input image samples x_i, kernel parameters

1: For each pixel in the image x_i, set the density estimation location to $y_{i,1} = x_i$
2: Iteratively compute $y_{i,j+1}$ using the mean shift vector computed by (2.44) till convergence to obtain $y_{i,final}$
3: Obtain a filtered image with pixels $z_i = y_{i,final}$
4: Group samples z_i into clusters C_p, $p = 1, \ldots, m$ using as criterion the distance in the joint intensity and spatial domain
5: Assign $l_i = p | z_i \in C_p$ for each pixel $i = 1, \ldots, n$.
6: **return** Labeled image samples (pixels) $l_i = x_i$

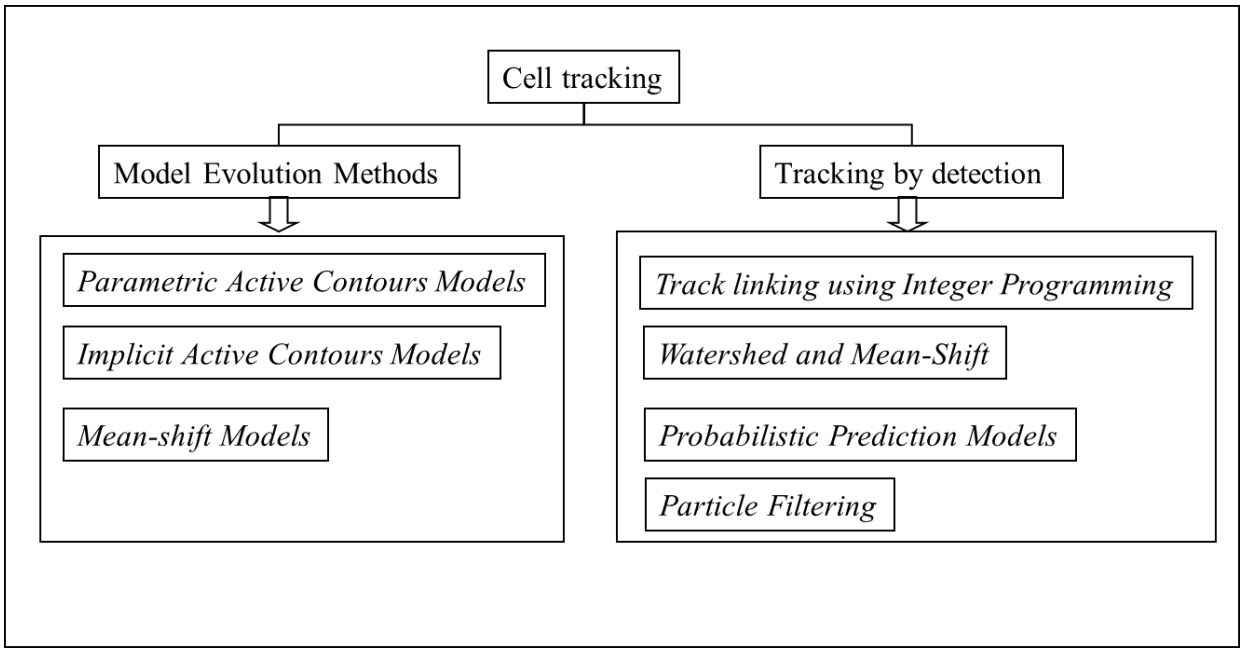

Figure 2.3: Cell tracking taxonomy.

2.2 Background on Cell Tracking

Cell tracking methogologies can be divided into (i) tracking by detection and (ii) tracking by model evolution [2, 65]. In the next subsections we give an overview of these approaches described in Figure 2.3.

2.2.1 Model Evolution Methods

Active contour methods for image segmentation allow a contour to deform to partition an image into regions. Deformable models try to fit one frame and use the result as initialization in the next frame evolution model. The association step is implicitly solved and established. However these techniques may require topology constraints and are computationally demanding especially for sequences of high cell density.

Parametric active contour models

These methods use explicit representations of the cell contours and perform segmentation by energy functional minimization [136, 99]. The classic snake methods cannot address topological changes related to cell events therefore they required some adjustments. Previous works proposed to add repulsive cell-to-cell forces to avoid fusion of touching cells, and incorporated topological operators for cell division [136, 135].

Implicit active contour models

Active contours are often implemented with level sets [90, 89, 47, 46, 48, 66, 65]. The primary drawback, however, is that they are slow to compute. The level set can be initialized manually as an initial contour or automatically exploiting the shape and characteristics of cells to track multiple cells [84]. In [84], the energy functional depends on the gradient magnitude along the boundary and region homogeneity within the boundary and spatial overlap of the detected cells. As a cell moves in the sequence, this method uses the spatial and shape consistency to modify the energy functional

$$\begin{aligned} E(C_i(s)) = &- \int_0^1 g(|\nabla I|)ds \\ &- \kappa \int\int_{\mu(\mathcal{C}_\rangle)} H(x,y)dxdy \\ &+ \int\int_{\mu(\mathcal{C}_\rangle)} (\sum_{j=1, j\neq i} \chi_j(x,y))dxdy, \end{aligned} \tag{2.45}$$

where g is a monotonically normalized increasing function, χ_j is the characteristic function for the Jth curve and $\mu(\mathcal{C}_|)$ is the region bounded by this curve.

$$g(z) = \left(\frac{2}{\sqrt{\pi}}\right) \int_0^z \exp^{-t^2} dt. \tag{2.46}$$

The term $\int_{\mu}\int_{C_{\rangle}} H(x,y)dxdy$ represents the homogeneity of the image inside the region delimited by the boundary C_i [84] also used by [103, 130]. However the method in [84] does not consider touching cells in the solution. We can find detailed discussion on Region-based methods in [100].

Additional techniques propose spatio-temporal segmentation using level sets [88, 90]. These methods include a post-processing stage to separate cell cluster and to form cell trajectories. Post-processing was also proposed in [129, 20] to correct cell fusions.

Zhang et al [132] proposed coupled geometric active contours and used one level set function for each cell. The coupling constraints are applied to avoid cell overlapping. Dufour et al [47] extended this framework to 3D analysis. In a more recent work, Dzyubachyk et al [48] introduced an improved active couple surface technique by addressing sensitivity to energy weights, handled touching cells and entering cells. However, this method is still computationally demanding because multiple level set evolution PDEs needed to be solved. Dufour et al [46] proposed some elegant approaches for multiple cell tracking by means of discrete active meshes that reduces the computational cost. Another proposed solution was to apply topological constraints in the level set evolution equation to prevent cell merging while allowing cell division [60, 67, 87]. In a more recent method [77] the energy functional was solved by applying a fast level set-like and graph cut-based framework without having to numerically solve a PDE. The authors also used a topological prior on the object indicator function to replace coupling of multiple models. In order to overcome the computational cost and long execution time drawbacks of the model evolution methods, we can incorporate the parallelism concept in the implementation and run multiple level set evolution PDEs simultaneously for each frame. This will be very beneficiary to achieve high-speed computation.

Furthermore, the authors in [98, 105, 97] utilize probabilistic motion prediction based on Kalman tracking or Particle Filtering (PF) to complement active contours. Besides level set evolution models, an alternate approach in [40] uses a mean shift model to track centroids

of cells and perform backward tracking to handle cell divisions.

2.2.2 Tracking by Detection

These approaches typically detect the cells in each frame and then match cells between consecutive frames. The first stage is achieved by image segmentation techniques based on intensity, texture or gradient [56, 65, 106]. The second stage is completed by data association and cell correspondence techniques. Usually these techniques use probabilistic functions between frames. Tracking by detection techniques may face challenges in mitosis tracking and when touching cells are segmented as a single cell. Their main advantages are that they
(i) can work on lower imaging frequencies than the model evolution techniques
(ii) involve advanced data association techniques for tracking
(iii) separate the segmentation and tracking tasks, therefore different segmentation techniques can be used with a single tracking algorithm.

Data association is the process of associating some measurements to known cell tracks. This process can use two different approaches:

- Bayesian Computes the full distribution in Data association space based on priors, posterior information

- Non-Bayesian like Nearest Neighbor (works good if solutions are well separated), maximum likelihood estimate from all the Data Association possible solutions.

In previous reports in the literature, the authors in [2] used seeded watershed to address touching cells, followed by feature-based cell matching. They performed image-by-image track linking by means of integer programming. Yang et al [129] proposed to use watershed and mean shift to identify cell cycle progression but did not construct cell lineage.

In the tracking stage, when we encounter increasing cell density, the temporal association step requires sophisticated strategies to deal with one-to-many and many-to-one

matching problems [65, 89, 32]. In [65] image-by-image linking is accomplished using integer programming. Padfield et al [89] introduced a coupled minimum-cost flow algorithm for mitosis and merging events coupled with some operations on particular edges. They used linear programming to choose the edges of graphically represented constraints.

In contrast to image-by-image linking techniques, batch algorithms use information from future frames or whole image sequence to create cell tracks and detect cell events [7, 94, 88]. The authors in [72] proposed a batch algorithm that optimizes a probabilistic scoring function and may address false positives and false negatives in detection stage, clustered cells. It can also handle cell mitosis, apoptosis and other events.

Another subgroup of methods combines detection and data association using probabilistic prediction models. These methods predict global motion and characteristic parameters of the objects. Earlier approaches used Kalman filtering followed by Particle Filtering techniques [110, 109, 107, 108]. In the approach proposed in [128], the authors used marker controlled watershed and region merging with context information for cell detection and delineation. They performed tracking using modified mean shift and Kalman filtering. Next, we describe the original particle filter technique.

Particle filters

Particle filters (PFs) have been used for many tracking applications [33, 98, 97, 109, 94, 108, 68, 69, 106]. They use sets of probabilistically derived samples to describe the most likely states of a system. They use the temporal structure of distributions. Let $X_t = x_1, x_2, ..., x_t$ be the states of a system with respect to time t.

Let $Z_t = z_1, z_2, ..., z_t$ be a sequence of observations related to x_i and let x_t follow the Markovian assumption of dependence on x_{t-1}, $P(x_t)|x_{t-1})$

Let $S_t = (s_{ti}, \pi_{ti})$, $i = 1, \cdots, N$ be a weighted set of N samples s_i and their associated weights π_{t_i}. The measurements are determined using importance sampling. We assign probabilities

Algorithm 3 Particle filter

Require: Input the weighted set of N samples s_i and their associated weights π_{t_i}

Initialize $S_t = (s_{ti}, \pi_{ti}), i = 1, \cdots, N$
Set $c_0 = 0, c_i = c_{i-1} + \pi_{(t-1)i}, i = 1, \cdots, N$
Set $c_i = c_{i-1} + \pi_{(t-1)i}, i = 1, \cdots, N$
(Cumulative probabilities)
repeat
  Generate n^{th} sample of S_t, $j = argmin(c_i > r) \in [0, 1]$
  Prediction step
  Use Markovian behavior of x_t to derive S_{tn}
  In Kalman case:
  $S_{tn} = A_{t-1} S_{(t-1)j} + w_{t-1}$, for matrices A_{t-1} and noise w_{t-1}
  Correction step
  Estimate $\pi_{tn} = P(z_t | x_t = S_{tn}$
until $Iterations = N$
Normalize $\pi_{t_i}, i = 1, \cdots, N$
Estimate $x_t = \sum_{=1}^{N} \pi_{ti} S_{t_i}$, or more generally $f(x_t) = \sum_{=1}^{N} \pi_{ti} f(S_{t_i})$
return

proportional to the importance weights π_{t_i} which are approximations to the probabilities of the samples such that $\sum_{=1}^{N} \pi_k = 1$. Our goal is to derive S_t from S_{t-1}. So, we generate N samples and weights at time t from S_{t-1}, using the Markov assumption and re-weight the result given the observation z_t. We list the main stages of the particle filtering in Algorithm 3. Moreover, Figure 2.4 displays a simulated cell tracking problem with 4 cells and random motion. Particle filters work well for a small number of cells as we can observe in this figure.

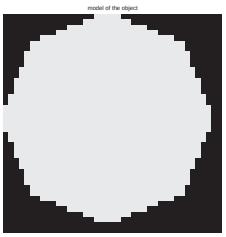

(a) Particle filter object model.

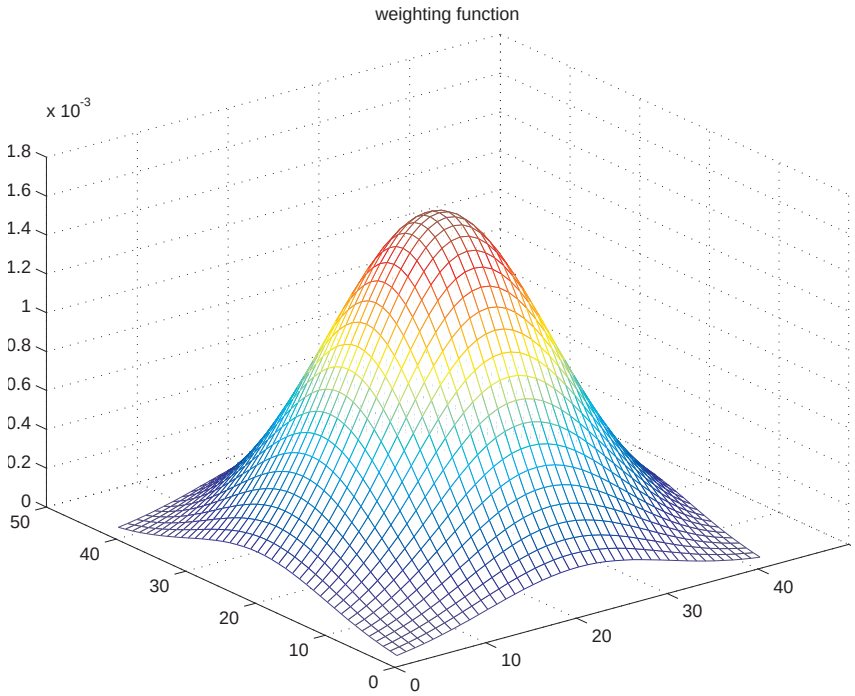

(b) Particle filter weight function.

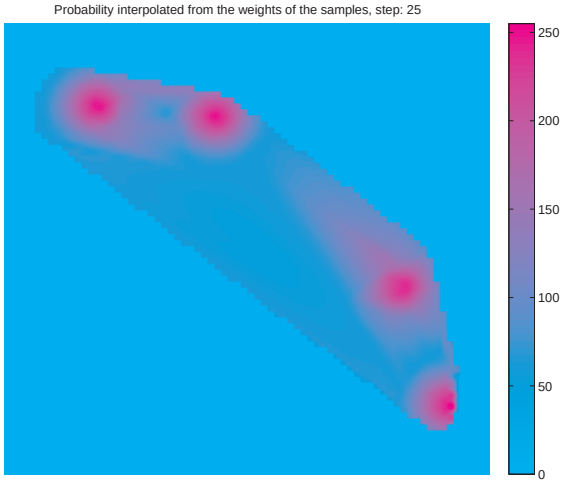

(c) Particle filter probability.

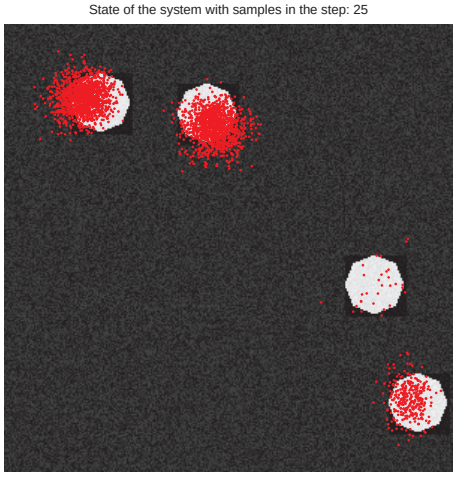

(d) Particle filter state of the system at the 50th iteration with 1500 samples.

Figure 2.4: Example of object tracking using the particle filter technique.

Chapter III: CELL SEGMENTATION

3.1 Region-based Level-set Model with Temporal Linking

In contrast to edge based methods like classical snakes [61] and early level-set methods [75], where an edge detector is used to stop the evolving curve, region-based methods tend to be less sensitive to noise. The use of region-based statistics may prove advantageous for images characterized by edge discontinuity and higher level of noise. The Chan-Vese (CV) method [29, 28, 84] is a region-based active contour model for energy minimization. Here, we describe the theoretical background of Chan-Vese model and its minimization framework. This model is a special case of the Mumford-Shah functional [85] for segmentation using piecewise constant approximation. This model segments an input scalar image $I(x, y)$ with $I : \Omega \to \mathbb{R}$ and $(x, y) \in \Omega \subset \mathbb{R}^2$ into two disconnected regions Ω_1 and Ω_2 representing the foreground and background respectively of low intra-region variance and separated by a smooth closed contour C such that $\Omega = \Omega_1 \cup \Omega_2 \cup C$. Here Ω denotes the image domain. The segmentation of an image is computed by minimizing the following energy functional:

$$\begin{aligned} F(\mathcal{C}, c_1, c_2) =& \mu \cdot length(\mathcal{C}) + \nu \cdot area(\mathcal{C}) \\ &+ \lambda_1 \int_{inside(\mathcal{C})} |I(x, y) - c_1|^2 dxdy \\ &+ \lambda_2 \int_{outside(\mathcal{C})} |I(x, y) - c_2|^2 dxdy, \end{aligned} \tag{3.1}$$

where $\mathcal{C}$ is the evolving curve, c_1 and c_2 are the average intensity levels inside and outside the contour $\mathcal{C}$, and $\mu, \nu, \lambda_1, \lambda_2 \geq 0$ are energy weights. The length of $\mathcal{C}$ and the area are regularizing terms. The idea is to evolve the contour $\mathcal{C}$ from some initialization until the fitting energy is minimized:

$$\inf_{\mathcal{C}, c_1, c_2} F(\mathcal{C}, c_1, c_2). \tag{3.2}$$

This method solves the Mumford-Shah [85] model but restricting the solution to be a piecewise constant with only two regions.

Chan and Vese proposed to use level-set functions to solve this optimization problem. In the level-set method, the contour is represented as the zero level-set of a Lipschitz function $\phi : \Omega \to \mathbb{R}$, where ϕ is positive inside $\mathcal{C}$ and negative outside $\mathcal{C}$:

$$\begin{cases} \phi(x,y) > 0, & \forall x \in \Omega_1 \\ \phi(x,y) = 0, & \forall x \in \Gamma \\ \phi(x,y) < 0, & \forall x \in \Omega_2. \end{cases} \tag{3.3}$$

The closed curve $\mathcal{C}$ that separates the image domain Ω into two distinct regions is defined by $\Gamma(t)$ as

$$\Gamma = \{(x,y) \in \Omega | \phi(x,y) = 0\}. \tag{3.4}$$

Figure 3.1 shows the value of the level set function corresponding to a closed curve $\mathcal{C}$ composed of three circles.

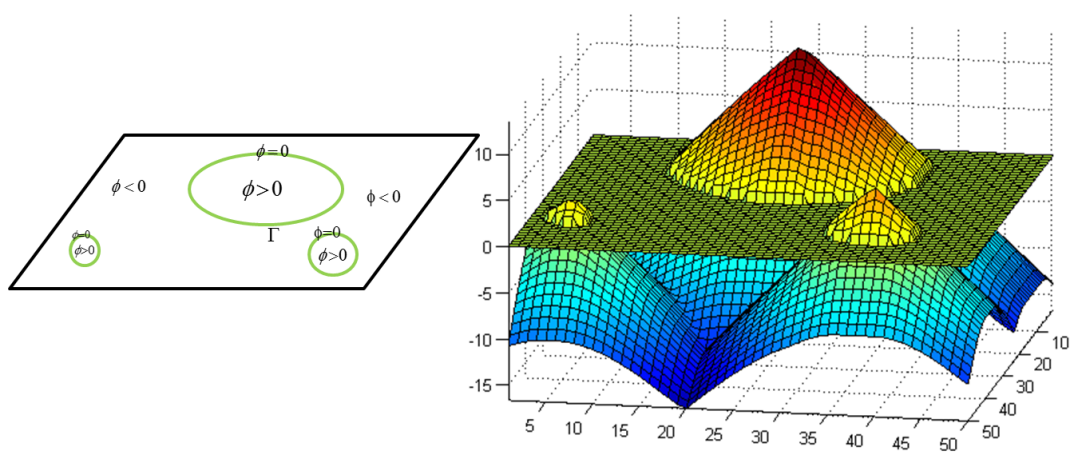

Figure 3.1: Representation of the level set function (right) corresponding to the image (left).

The length and area of $\mathcal{C}$ are regularizing terms that are formulated using the Heaviside

H and Dirac δ functions.The Heaviside step function is a discontinuous function whose value is zero for negative argument and one for integer positive argument. It is an example of the general class of step functions.

$$H(x) = \begin{cases} 1, & x \geq 0, \\ 0, & x < 0, \end{cases} \tag{3.5}$$

where x is a real variable. The Heaviside function can also be defined as the integral of the Dirac delta function: $\frac{dH(x)}{dx} = \delta(x)$. The derivative of the Heaviside function is zero everywhere except in zero where it goes to infinity.

By introducing the characteristic functions χ_1 and χ_2 defining the two regions $\Omega_1(t)$ and $\Omega_2(t)$

$$\chi_1(\phi) = H(\phi(x,y)) = \begin{cases} 1, & (x,y) \in \Omega_1(t), \\ 0, & \text{otherwise}, \end{cases} \tag{3.6}$$

$$\chi_2(\phi) = 1 - H(\phi(x,y)) = \begin{cases} 1, & (x,y) \in \Omega_2(t), \\ 0, & \text{otherwise}, \end{cases} \tag{3.7}$$

we may rewrite (3.1) using (3.6) and (3.7) in terms of H and δ functions. The segmentation of an image domain Ω is computed by minimizing the following energy functional using the level-set function:

$$\begin{aligned} F(\phi, c_1, c_2) =& \mu \int_\Omega \delta(\phi(x,y)) |\nabla H(\phi(x,y))| dxdy + \nu \int_\Omega H(\phi(x,y)) dxdy \\ &+ \lambda_1 \int_\Omega |I(x,y) - c_1|^2 H(\phi(x,y)) dxdy \\ &+ \lambda_2 \int_\Omega |I(x,y) - c_2|^2 (1 - H(\phi(x,y))) dxdy, \end{aligned} \tag{3.8}$$

where

$$c_1(\phi(x,y)) = \frac{\int_\Omega I(x,y)H(\phi(x,y)dxdy}{\int_\Omega H(\phi(x,y))dxdy} \tag{3.9}$$

$$c_2(\phi(x,y)) = \frac{\int_\Omega I(x,y)(1-H(\phi(x,y))dxdy}{\int_\Omega (1-H(\phi(x,y)))dxdy}. \tag{3.10}$$

- The length of $\mathcal{C}$ is $\int_\Omega |\nabla H(\phi(x,y))|dxdy$, because $H(\phi)$ is constant inside and outside the boundary, then the gradient is equal to zero except on the boundary. This gives exactly the number of points on the boundary.

Analytic approximation of the Heaviside

The Heaviside function is not differentiable. So, [28] suggest to use the smoothed heaviside approximation regularized by some $H_\epsilon(x)$ in C^1 so that as $\epsilon \to 0$, $H_\epsilon(x)$ converges to $H(x)$. Among the smooth analytic approximation to the step function we use:

$$H_\epsilon = \lim_{\epsilon \to 0} \left(\frac{1}{2} + \frac{1}{\pi} \arctan(\frac{x}{\epsilon}) \right). \tag{3.11}$$

The Dirac delta function $\delta(x)$ is then regularized to $\delta_\epsilon(x) = \frac{dH_\epsilon}{dx}$

$$\delta_\epsilon(x) = \lim_{\epsilon \to 0} \frac{1}{\pi} \left(\frac{\epsilon}{\epsilon^2 + x^2} \right). \tag{3.12}$$

The Chan-Vese algorithm uses variational calculus methods [5] to evolve the level set function that minimizes some energy functional.

The Gateaux differential or Gateaux derivative is often used to formalize the functional derivative generally used in the calculus of variations and physics. It is a generalization of the concept of directional derivative in differential calculus.

Definition 3.1.1 (Gateau differential)**.** Suppose X and Y are locally convex topolog-

ical vector spaces, $F : X \to Y$. The Gateaux differential $dF(v;\psi)$ of F at $v \in U$ in the direction $\psi \in X$ is defined as

$$dF(u;\psi) = \lim_{\epsilon \to 0} \frac{F(v+\epsilon\psi) - F(v)}{\epsilon} = \frac{d}{d\epsilon} F(v+\epsilon\psi)\bigg|_{\epsilon=0}. \tag{3.13}$$

If the limit exists for all $\psi \in X$, then one says that F is Gateaux differentiable at v. Since $\frac{dH(x)}{dx} = \delta(x)$. By chain rule we obtain

$$|\nabla H(\phi)| = |\delta(\phi)\nabla\phi| = \delta(\phi)|\nabla\phi|. \tag{3.14}$$

In [28] the Euler-Lagrange (E-L) equations and the gradient-descent method were used to derive the following evolution equation for the level-set function ϕ that minimizes the fitting energy using time to parametrize the gradient descent:

$$\begin{aligned}\frac{\partial\phi(t,x,y)}{\partial t} =& \delta(\phi(x,y)) \cdot \left[\mu \cdot div\left(\frac{\nabla\phi(x,y)}{|\nabla\phi(x,y)|}\right) - \nu \right.\\ & \left. - \lambda_1(I-c_1)^2 + \lambda_2(I-c_2)^2\right] \in (0,\infty) \times \Omega,\end{aligned} \tag{3.15}$$

with initial and Neumann boundary conditions

$$\phi(0,x,y) = \phi_0(x,y) \in \Omega, \tag{3.16}$$

$$\frac{\delta(\phi)}{|\nabla\phi|} \cdot \frac{\partial\phi}{\partial\vec{n}} = 0 \in \partial\Omega. \tag{3.17}$$

Discretization

The discretized solution as reported in [28] is

$$\frac{\phi_{i,j}^{n+1}-\phi_{i,j}^{n}}{\Delta t}=\delta_{\epsilon}(\phi_{i,j}^{n})\Bigg[\frac{\mu}{h^2}\Delta_{-}^{x}\left(\frac{\Delta_{+}^{x}\phi_{i,j}^{n+1}}{\sqrt{\left(\frac{\Delta_{+}^{x}\phi_{i,j}^{n}}{h}\right)^2+\frac{\left(\phi_{i,j+1}^{n}-\phi_{i,j-1}^{n}\right)^2}{4h^2}}}\right)$$
$$+\frac{\mu}{h^2}\Delta_{-}^{y}\left(\frac{\Delta_{+}^{y}\phi_{i,j}^{n+1}}{\sqrt{\left(\frac{\Delta_{+}^{y}\phi_{i,j}^{n}}{h}\right)^2+\frac{\left(\phi_{i+1,j}^{n}-\phi_{i-1,j}^{n}\right)^2}{4h^2}}}\right)$$
$$-\nu-\lambda_1(I_{i,j}-c_1(\phi^n))^2+\lambda_2(I_{i,j}-c_2(\phi^n))^2\Bigg], \tag{3.18}$$

where $\Delta_{-}^{x}\phi_{i,j}=\phi_{i,j}-\phi_{i-1,j}$, $\Delta_{+}^{x}\phi_{i,j}=\phi_{i+1,j}-\phi_{i,j}$, $\Delta_{-}^{y}\phi_{i,j}=\phi_{i,j}-\phi_{i,j-1}$, and $\Delta_{+}^{x}\phi_{i,j}=\phi_{i,j+1}-\phi_{i,j}$. Also, h denotes the space steps, Δt denotes the time step, $(x_i,y_j)=(i\cdot h, j\cdot h)$ are the grid points, and $\phi_{i,j}^{n}=\phi(n\Delta t,x_i,y_j)$ represents the approximation of $\phi(t,x,y)$.

Temporally Linked Level-set Segmentation

The initial contour plays a very important part in the convergence of the Chan-Vese evolution process. This approach makes use of temporal connection between consecutive level-set results [28, 86, 90]. That is, when segmenting an image, which is a part of a temporal sequence, we make use of the level-set results reached from minimization of the global energy associated with the contours of the segmented cells found in the previous time point

$$\phi_{n+1}(x,y;0)=\phi_n(x,y;i_{final}),\forall(x,y)\in\Omega, \tag{3.19}$$

where n is the frame number in the time-lapse sequence, and i_{final} is the number of iterations required to converge for frame n. We take the contour result of each frame as the initial contour for the following one. These results are utilized to minimize the energy functional

of the next image. If the segmentation in frame n is accurate, then this initialization will correspond to a point close to the global optimum of the energy functional in frame $n+1$. The main steps of this technique are summarized in Algorithm 4. A flowchart of this algorithm

Algorithm 4 Temporally Linked Chan-Vese Segmentation

Require: frame D_i, curve C of spatio-temporal mask result R_{STM}
1: $\phi^0 \leftarrow$ Initial level-set signed distance (C)
2: **repeat**
3: Each iteration n Update average intensities c_1 and c_2
4: $c_1(\phi^n) \leftarrow$ Mean intensity of image pixels of D_i inside the contour C^n
5: $c_2(\phi^n) \leftarrow$ Mean intensity of image pixels of D_i outside the contour C^n
6: $F(\phi^n, c_1, c_2) \leftarrow$ Normalized energy of image D_i
7: Solve PDE $\frac{\partial \phi(t,x,y)}{\partial t} = 0$ in ϕ^n to obtain ϕ^{n+1} from (3.15) with $c_1(\phi^n)$ and $c_2(\phi^n)$
8: Reinitialize ϕ locally to the signed distance function to the curve
9: **until** Convergence or $n > n_{max}$
10: Apply morphological operations to the segmented regions
11: $R_S \leftarrow$ Thresholding ϕ_{final}
12: **return** Binary mask R_S

is displayed in Figure 3.2.

3.2 Spatio-Temporal Diffusion-based Motion Segmentation

We propose a moving object segmentation approach that includes a statistical intensity standardization stage, followed by a spatio-temporal system of coupled PDEs to apply nonlinear diffusion in the joint spatial and temporal domain [10, 9]. We then apply non-parametric density estimation followed by watershed segmentation and likelihood-based decision function to detect and delineate the moving objects.The main stages of this method are outlined in Figure 3.3.

3.2.1 Frame Intensity Standardization by Histogram Transformation

PDE-based techniques calculate differential approximations; therefore they are sensitive to variations in pixel intensity ranges. The main objective of this stage is first to reduce intensity variations between frames of each sequence, and second, to obtain a robust intensity prior

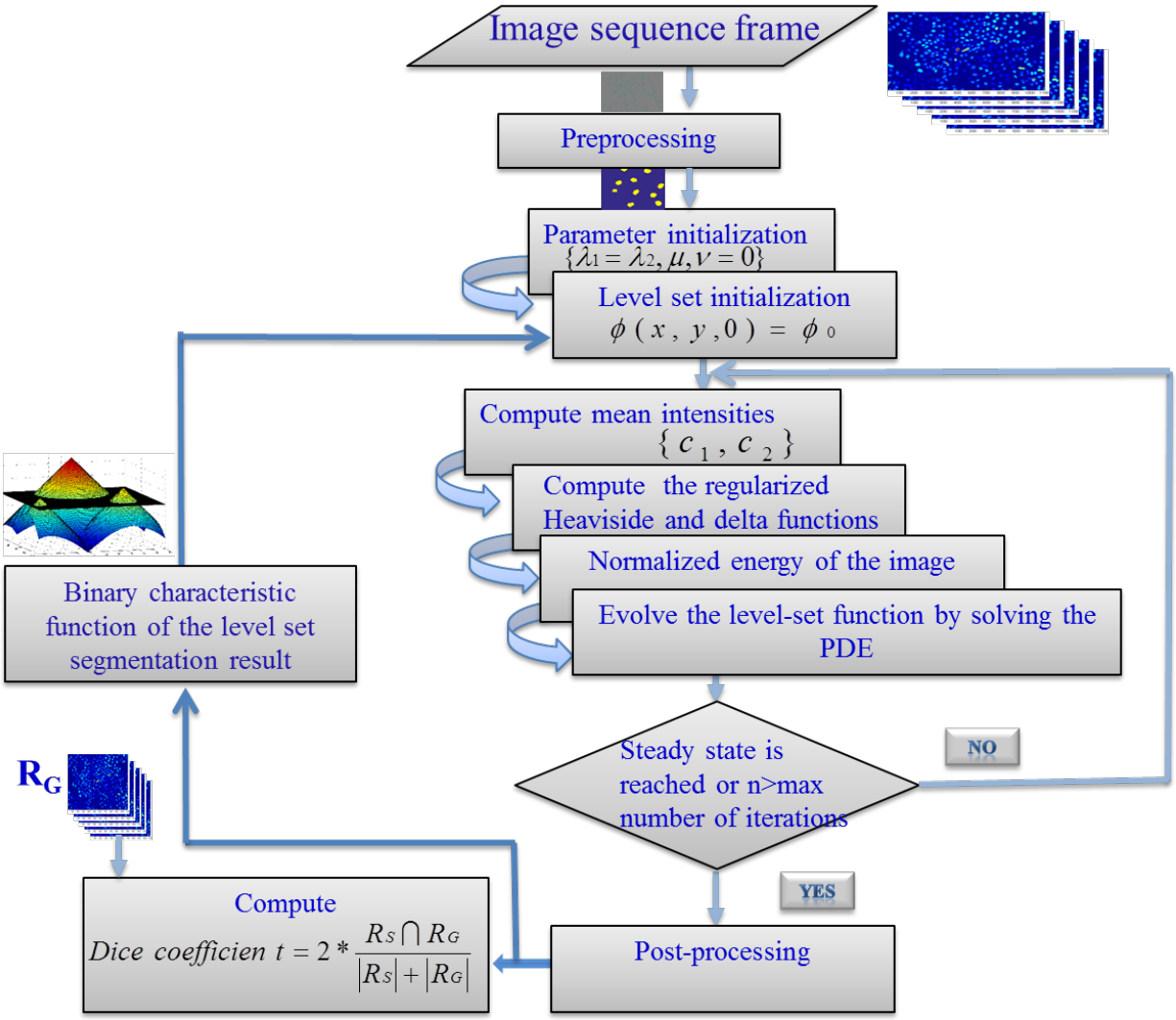

Figure 3.2: Main stages of the Temporally linked level-set segmentation.

for the cell delineation process. We apply a histogram transformation approach to match the intensity distribution of each three consecutive frames defined by (3.20) to an intensity distribution model learned from all frames of the sequence during the training stage.

$$P_{3F}(I) = \lim_{N_{total} \to \infty} \frac{N(I)}{N_{total}}, \quad F_{3F}(k) = \int_0^k P_{3F}(I) dI. \tag{3.20}$$

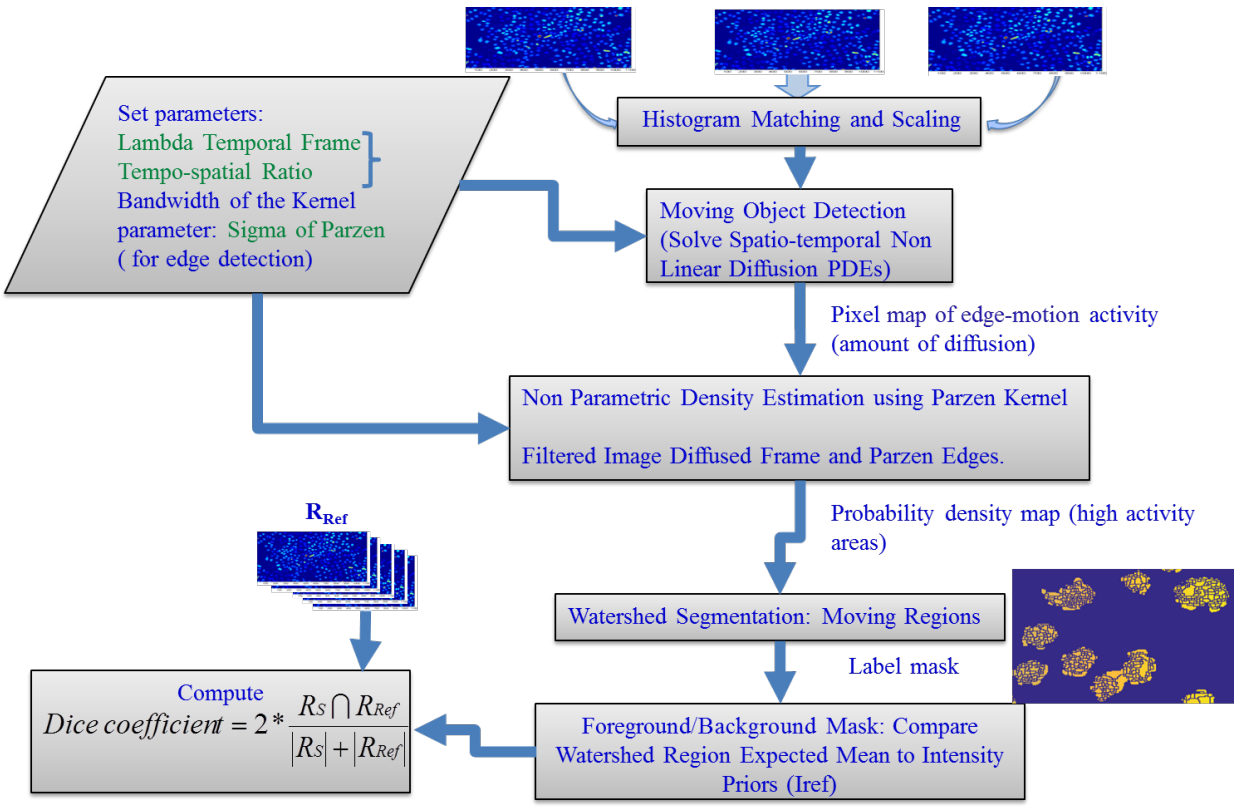

Figure 3.3: Spatio-temporal diffusion-based technique.

The general idea is to transform the frame intensities so that the cell/background threshold I_{ref} determined from the F_{AF}, as expressed in (3.21), matches the global Cumulative Distribution Function reference value $F_{AF}(I_{ref})$ corresponding to the I_{ref} value (3.21) indicating the tail of background intensity distribution of the complete sequence as displayed in Figure 3.4 (top).

$$P_{AF}(I) = \lim_{N_{total} \to \infty} \frac{N(I)}{N_{total}}, \quad F_{AF}(k) = \int_0^k P_{AF}(I) dI. \tag{3.21}$$

We aim to find a transformation so that the output image is a similar image that has a background value with the same order of brightness of the input image. Figure 3.4 (bottom) displays how we can determine the I_{test} value from the PDF of each three consecutive frames

at the training stage using the prior value $F_{AF}(I_{ref})$ as expressed by (3.22).

$$I_{test} = arg \min_i |F_{3F}(I(\omega)) - F_{AF}(I_{ref})|, \tag{3.22}$$

where $\omega \in \Omega_{3F}$, $I : \mathbb{Z}^2 \rightarrow \mathbb{R}^+$. Using these values, the resulting images are scaled and defined over the $[0-255]$ range and with respect to the global minimum and global maximum intensities of all the frames of the dataset sequence after applying equations (3.23), (3.24), and (3.25).

$$T_1(I) = \frac{I_{ref} - G_{Min}}{I_{test} - L_{Min}}(I - G_{Min}) + G_{Min}. \tag{3.23}$$

$$T_2(I) = \frac{255 \cdot (I - G_{Min})}{G_{Max} - G_{Min}}. \tag{3.24}$$

$$I_S(\omega) = T(I(\omega)) = (T_2 \circ T_1)(I(\omega)), \quad \omega \in \Omega_{3F}. \tag{3.25}$$

We experimentally found that the matched frames are less sensitive to the temporal, spatial diffusion parameters and Parzen kernel bandwidth values than the raw frames. In our experiments we used 256 bins for all datasets. The following steps define the two algorithms that learn the CDF reference value for background intensity $F_{AF}(I_{ref})$ at the training stage (Algorithm 5) and transform every source image at the testing stage (Algorithm 6) so as to make its testing background as close as possible to the reference intensity.

Algorithm 5 Histogram transform training stage

Require: dataset $\mathcal{D} = \{D_1, D_2, \ldots, D_N\}$

1: $\mathcal{D}^{AF} \leftarrow$ Concatenate $D_k, \quad k = 1, \ldots, N$
2: $Global_{Max} \leftarrow$ Maximum pixel intensity of $\mathcal{D}^{AF}$
3: $Global_{Min} \leftarrow$ Minimum pixel intensity of $\mathcal{D}^{AF}$
4: Plot $P_{AF}(I) = \lim_{N_{total} \rightarrow \infty} \frac{N(I)}{N_{total}}$
5: Choose (reference value) I_{ref} in P_{AF} at beginning of histogram tail for background distribution
6: $F_{AF}(k) \leftarrow \int_0^k P_{AF}(I)dI$
7: $F_{AF}(I_{ref}) \leftarrow$ Closest percentile of I_{ref}
8: **return** $F_{AF}(I_{ref}), Global_{Max}, Global_{Min}, I_{ref},$

Algorithm 6 Histogram transform testing stage

Require: dataset $\mathcal{D} = \{D_1, D_2, \ldots, D_N\}$, $F_{AF}(I_{ref})$, I_{ref}, $Global_{max}$, $Global_{min}$

$\mathcal{D}^{mir} \leftarrow$ Mirror the frames at borders $\{D_2, D_1, D_2, ..., D_{N-1}, D_N, D_{N-1}\}$
for each three consecutive frames $\{D_{i-1}, D_i, D_{i+1}\} \in \mathcal{D}^{mir}$ **do**
  $\mathcal{I}_i^{3F} \leftarrow$ Concatenate $\{D_{i-1} \cup D_i \cup D_{i+1}\}$ vectors
  $Local_{min} \leftarrow$ Minimum pixel intensity of $\mathcal{I}_i^{3F}$
  Compute $P_i^{3F}(\mathcal{I}_i^{3F}) = \lim_{N_{total} \to \infty} \frac{N(I_i^{3F})}{N_{total}}$ using 255 bins
  $F_i^{3F}(k) \leftarrow \int_0^k P_i^{3F}(\mathcal{I}_i^{3F}(\omega))d\omega$
  $I_i^{test} \leftarrow min|F_i^{3F}(\mathcal{I}_i^{3F}(\omega)) - F_{AF}(I_{ref})|$ where $\omega \in \Omega_{3F}$, $I : \mathbb{Z}^2 \to \mathbb{R}^+$
  for all $I_i^{3F} \in D_{i-1} \parallel D_i \parallel D_{i+1}$
  $T_1(I_i^{3F}) = [(I_{ref} - Global_{Min}) / (I_i^{test} - Local_{Min})]\,(I_i^{3F} - Global_{Min}) + Global_{Min}$
  $T_2(I_i^{3F}) = 255 \cdot (I_i^{3F} - Global_{Min}) / (Global_{Max} - Global_{Min})$
  $T_{I_i^{3F}} = (T_2 \circ T_1)(I_i^{3F}(\omega))$ where $\omega \in \Omega_{3F}$
end for
return $\mathcal{D}_{T_2 \circ T_1}$

Figure 3.5 displays an intensity standardization example applied on three consecutive frames. The top row displays the histogram of the complete dataset and transformations T_1 and T_2 given by (3.23) and (3.24) respectively. The bottom row shows the histogram of 3 frames used to determine I_{test}, the original histogram of currently processed frame and transformed histogram after applying (3.25). We note that after the histogram transformation and scaling, all frames of the same sequence are going to have similar pixel intensity ranges.

3.2.2 Spatio-temporal Diffusion

Perona-Malik Anisotropic Diffusion

Diffusion algorithms perform image restoration by finding numerical solutions of the heat diffusion PDE [125, 8]. In this framework, the linear diffusion model is equivalent to applying Gaussian filtering to the image. The homegeneity of the gaussian diffusion filtering may lead to diffusion of important image features. To avoid the blurring and localization problems of linear diffusion filtering, Perona and Malik [92] proposed to replace the classic isotropic diffusion equation with the nonlinear diffusion model by adding a diffusivity coefficient. This

inhomogeneous coefficient depends on the space activity in the image based on the norm of the local gradient of the image. Perona-Malik equation is based on the following PDE:

$$\frac{\partial I}{\partial s} = div\left[g\left(|\nabla I(x,y,s)|\right)\cdot\nabla I(x,y,s)\right], \tag{3.26}$$

where I is the image intensity, s the scale variable for 2D case, and $g(\cdot)$ a function that determines the amount of diffusion, also known as diffusivity function. The problem formulation with a Neumann boundary condition is

$$\begin{cases} \frac{\partial I}{\partial s} = \nabla\left[g\left(|\nabla I(x,y,s)|\right)\cdot\nabla I(x,y,s)\right] \\ \frac{\partial I}{\partial s} = 0 \in \partial\Omega \\ I(x,y,0) = I_0(x,y) \in \Omega, \end{cases} \tag{3.27}$$

where Ω is the image domain which is a bounded subset of $\mathbb{R}^n$ with boundary of class C^1. We assume that the derivatives of I_0 vanish at the boundaries of the image domain. The diffusivity function is chosen to be monotonically decreasing from 1 to 0 while x changes from 0 to ∞ satisfying $\lim_{x\to\infty} g(x) \to 0$ so that diffusion is attenuated across edges. This function is usually controls the amount or rate of diffusion according to the edge strength. Common options for $g(\cdot)$ are the sigmoid and exponential functions also reported by Perona and Malik in [92]:

$$g(x) = \frac{1}{\left(1+\frac{x^2}{k^2}\right)} \tag{3.28}$$

$$g(x) = e^{\left(-\frac{x^2}{k^2}\right)}, \tag{3.29}$$

where k denotes the conductance parameter that is a positive constant that controls the sensitivity to edges and is usually determined experimentally. This formulation was referred to as anisotropic diffusion by Perona and Malik even though the locally adapted filter is isotropic, but it has also been referred to as inhomogeneous and nonlinear diffusion [124,

126] or Perona-Malik diffusion [92] by other authors. The inhomogeneous diffusion method does not diffuse the image in a uniform way. The Perona-Malik diffusion equation is presented and is shown to be equivalent to a a procedure that estimates a piecewise-constant image from a noisy input image [101]. Nonlinear diffusion filter is used to enhance Gerig et al. used such filters to enhance MR images [54, 44], to perform edge preserving smoothing of MR images [119, 53]. Other authors have shown that diffusion filters can be used to enhance and detect object edges within images [82], this method has been extensively used for image restoration as it reduces smoothing at edges in order to preserve their contrast and location.

Spatio-temporal Nonlinear Diffusion

Partial Differential Equation Model

Here we propose to simulate nonlinear heat flow through the processed frames in both spatial and temporal dimensions. This operation smooths-out the background regions and simultaneously preserves the spatio-temporal discontinuities corresponding to cells. More specifically, performs intraregion smoothing while inhibiting interregion smoothing. This process is defined as follows: Given 3 consecutive frames of the sequence at times $\{t-1, t, t+1\}$, we define a system of three coupled PDEs for each frame. *At time points* $\tau = \{t-1, t, t+1\}$

$$\begin{aligned}\frac{\partial I(i,j,\tau,s)}{\partial s} =& g(|\nabla I(i,j,\tau,s)|) \cdot \Delta I(i,j,\tau,s) \\ &+ \nabla g(|\nabla I(i,j,\tau,s)|) \cdot \nabla I(i,j,\tau,s).\end{aligned} \tag{3.30}$$

Initial condition

$$I(i,j,\tau,0) = I_0(i,j,\tau). \tag{3.31}$$

Boundary condition

$$\frac{\partial I}{\partial \vec{n}} = 0 \qquad \text{on } \partial\Omega \times \partial T \times (0,S). \tag{3.32}$$

Numerical solution

Moving regions are initially detected in each three consecutive frames by numerically solving the spatio-temporal partial-differential diffusion equation [11] where the diffusivity function is applied to the gradient magnitude of the image I. In this work we used the function (3.29) that is more suitable for region oriented applications [131]. This nonlinear diffusion is bound to the gradient magnitude [117]. It applies more diffusion in uniform regions and slows down at edges, therefore preserves high contrast edges over low contrast ones. We used the Finite Difference method to solve the system of (3.30) on a 2D square grid lattice. Since we assume that the derivatives of I_0 vanish at the boundary of Ω, We applied padding by replicating the pixel intensities at the image borders. This will give a zero gradient at the boundaries of Ω and will enable the detection and localization of motion within each 3 consecutive frames.

At t

$$\begin{aligned} I^{s+1}_{i,j,t} = I^{s}_{i,j,t} + \lambda_s[g(|\nabla I^{s}_{i+1,j,t}|) \cdot N_t + g(|\nabla I^{s}_{i-1,j,t}|) \cdot S_t \\ + g(|\nabla I^{s}_{i,j+1,t}|) \cdot E_t + g(|\nabla I^{s}_{i,j-1,t}|) \cdot W_t] \\ + \lambda_t[g(|\nabla I^{s}_{i,j,t-1}|) \cdot PF + g(|\nabla I^{s}_{i,j,t+1}|) \cdot NF] \end{aligned} \tag{3.33}$$

At $t-1$

$$\begin{aligned} I^{s+1}_{i,j,t-1} = I^{s}_{i,j,t-1} + \lambda_s[g(|\nabla I^{s}_{i+1,j,t-1}|) \cdot N_{t-1} \\ + g(|\nabla I^{s}_{i-1,j,t-1}|) \cdot S_{t-1} \\ + g(|\nabla I^{s}_{i,j+1,t-1}|) \cdot E_{t-1} \\ + g(|\nabla I^{s}_{i,j-1,t-1}|) \cdot W_{t-1}] \\ - 2\lambda_{tPF} \cdot g(|\nabla I^{s}_{i,j,t-1}|) \cdot PF \end{aligned} \tag{3.34}$$

At $t+1$

$$
\begin{aligned}
I^{s+1}_{i,j,t+1} = I^{s}_{i,j,t+1} + \lambda_s [& g(|\nabla I^{s}_{i+1,j,t+1}|) \cdot N_{t+1} \\
& + g(|\nabla I^{s}_{i-1,j,t+1}|) \cdot S_{t+1} \\
& + g(|\nabla I^{s}_{i,j+1,t+1}|) \cdot E_{t+1} \\
& + g(|\nabla I^{s}_{i,j-1,t+1}|) \cdot W_{t+1}] \\
& - 2\lambda_{tNF} \cdot g(|\nabla I^{s}_{i,j,t+1}|) \cdot NF
\end{aligned} \tag{3.35}
$$

where

$$N_t = I^{s}_{i-1,j,t} - I^{s}_{i,j,t}, \quad S_t = I^{s}_{i+1,j,t} - I^{s}_{i,j,t} \tag{3.36}$$

$$W_t = I^{s}_{i,j-1,t} - I^{s}_{i,j,t}, \quad E_t = I^{s}_{i,j+1,t} - I^{s}_{i,j,t} \tag{3.37}$$

$$PF = I^{s}_{i,j,t-1} - I^{s}_{i,j,t}, \quad NF = I^{s}_{i,j,t+1} - I^{s}_{i,j,t}. \tag{3.38}$$

In (3.33), (3.34), and (3.35) λ_s, λ_t, λ_{tPF}, λ_{tNF} denote the numerical "time" steps for spatial, temporal, next frame temporal, and previous frame temporal terms respectively. In our implementation we set $\lambda_t = TS_{Ratio} \cdot \lambda_s$ and $\lambda_{tPF} = \lambda_{tNF}$, where TS_{Ratio} is a fixed parameter for the ratio of temporal to spatial diffusion. The diffusivity function is applied to the gradient magnitude of the image I.

3.2.3 Detection of Spatio-temporal Discontinuities by Parzen Density Estimation

The idea is to estimate the likelihood of mean intensity in the neighborhood of each pixel in the diffused frame. Assuming a model of unimodal probability density function (PDF) for region interiors and bimodal PDF for edges, we use the likelihood of mean intensity as an index of edge occurrence. Low values of this index correspond to a bimodal PDF indicating an edge. We estimate this likelihood by the nonparametric technique of Parzen kernels [91,

58, 35]. The Parzen density estimation belongs to the nonparametric density methods [23] i.e. methods to estimate the probability density function of a random variable that do not impose any initial assumptions about the shape of the probability density functions. Its operation is based on placing at each observation sample a probability mass and producing a potential according to a Gaussian kernel. The contributions of all the sample points are averaged to estimate the density value at every point of the image [58].

$$f_h(x) = 1/(n \cdot h^p) \sum_{i=1}^{n} K((x - x_i)/h), \tag{3.39}$$

where $(x1, x2, , xn)$ is an independent and identically distributed sample drawn from some distribution with an unknown density P, $K(\cdot)$ is the kernel and $h > 0$ is a smoothing parameter called the bandwidth. We can see in (3.39) that the kernel-bandwidth h can strongly affect the PDF estimate, especially when the number of observations n is finite. Very small h values will produce a ragged density estimate, while very large values will smooth the structure of the PDF. An optimal h value is usually experimentally determined to find a compromise between the variability and accuracy and converge towards the true PDF. Figure 3.6 shows three density estimates: the green solid line corresponds to a small bandwidth, the black line corresponds to a large bandwidth, while the blue line represents a bandwidth selection that produces a more accurate estimate of the underlying bimodal distribution.

To show the effect of the bandwidth kernel width is vital for good results, we plot motion masks of Hela 02 with different Parzen kernel widths. In regions of high density we need to choose a narrow kernel width to allow us to model the variations in population density accurately. Conversely, in the low density, a very wide kernel is preferable, since the population there is very low. On a sample frame of a dense dataset, as in Figure 3.7 we clearly see that few cells are not detected when we choose a wide parzen bandwidth.

3.2.4 Cell Delineation and Identification

The edge map can be interpreted as a topographic surface consisting of valleys corresponding to spatio-temporally homogeneous areas and peaks denoting spatio-temporal discontinuities [93]. The next step is to apply watershed segmentation. Watershed analysis has emerged from mathematical morphology and was implemented by a series of morphology operators in its early versions [121] . Since then, several implementations have appeared, proposing iterative, sequential, arrowing, flow line oriented and flooding techniques [111]. Regional minima of the topographic relief are selected and flooded to form the moving regions. We obtain a watershed region in the resulting segmentation for each minimum. We first find the watershed ridges of the stochastic map of spatio-temporal discontinuities. The watershed transform divides a multivalued image into separate regions by identifying the regional minima and applying flooding operations to each minimum to fill the watershed basins. Each basin corresponds to a region. We first invert the stochastic map produced by Parzen density estimation to form regions separated by spatio-temporal discontinuities. To separate the cells we calculate intensities and areas of watershed regions and classify them into cells or background using area and intensity prior information and likelihoods $p(area|c_i)$, $p(I|c_i)$ in Gaussian form, where $c_i = \{background, cell\}$. Adjacent watershed regions with coherent motion should be merged together to form a moving object. We compute mean intensity over the watershed regions and classify into foreground or background using as threshold value the standardized reference value $T(I_{ref})$ calculated by (3.25).

3.3 Joint Spatio-temporal Diffusion and Temporally Linked Level-set Approach (ST-Diff-TCV)

We propose a joint method combining the Spatial and Temporal differential information with the high delineation accuracy that characterizes level set-based segmentation [36, 38, 42, 28]. More specifically, we use S-T Diffusion to delineate the cells first, then initialize TCV

with the S-T Diffusion result to refine the cell segmentation. We apply the S-T Diffusion technique on each modulo k frame to address cell events that may not be handled by TCV such as cell mitosis, cell division, new cells entering the field of view, and other cases. This strategy may also reduce the computational cost by applying the S-T Diffusion technique to a limited number of frames. We apply these methods on several datasets of fluorescence microscopy images with varying levels of difficulty with respect to cell density, resolution, contrast, and signal-to-noise ratio. The flowchart in Figure 3.8 outlines the main stages of our proposed technique. Furthermore, in Figs. 3.9 and 3.10 we display intermediate results from each stage on a test frame and its temporal neighbors for the C2DL−MSC02 and Fluo-N2DH-SIM04 sequences.

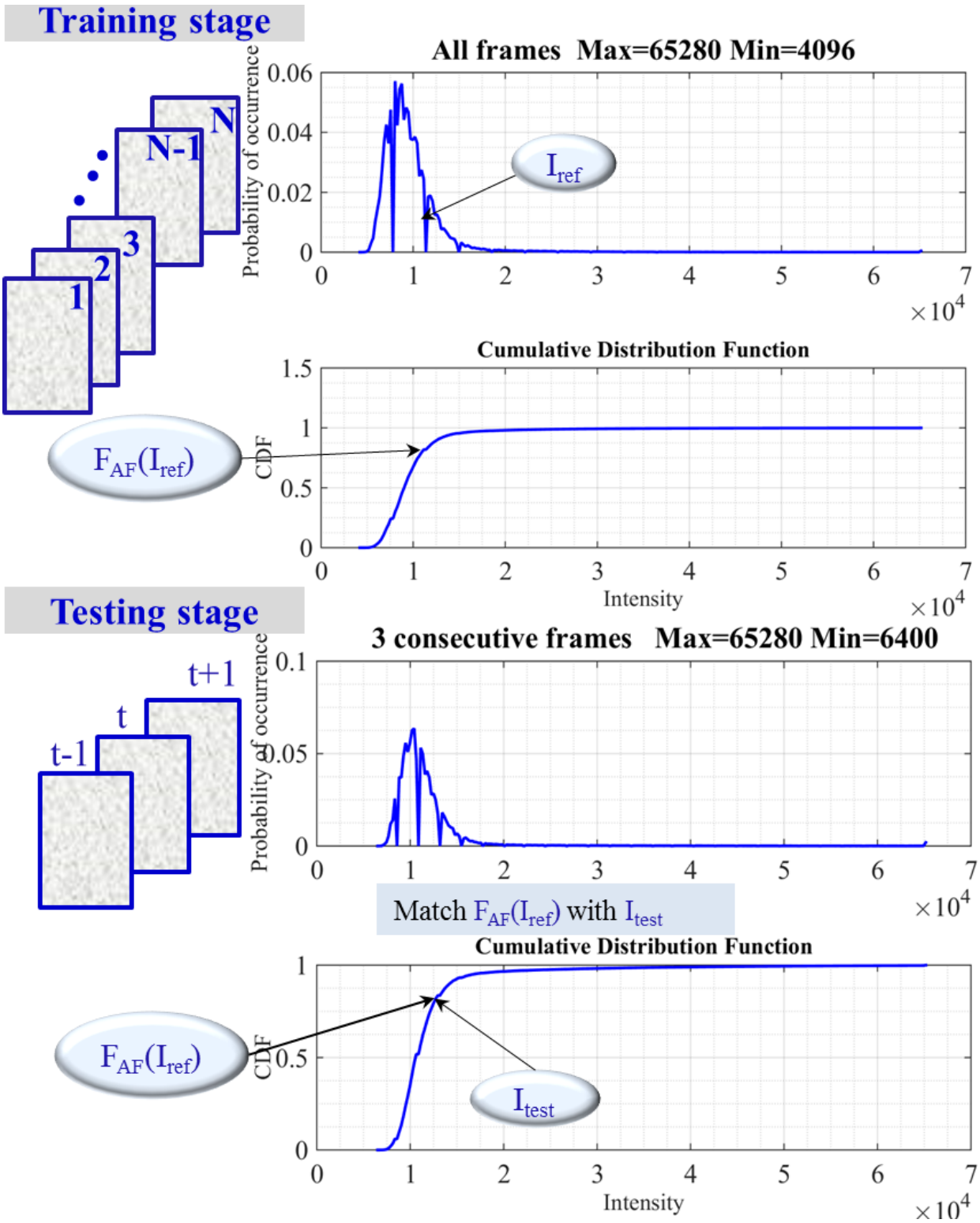

Figure 3.4: (Training stage) Probability density function of 48 frames of C2DL−MSC02 dataset and cumulative distribution function. (Testing stage) Normalized PDF and CDF of three consecutive frames of C2DL−MSC02 dataset.

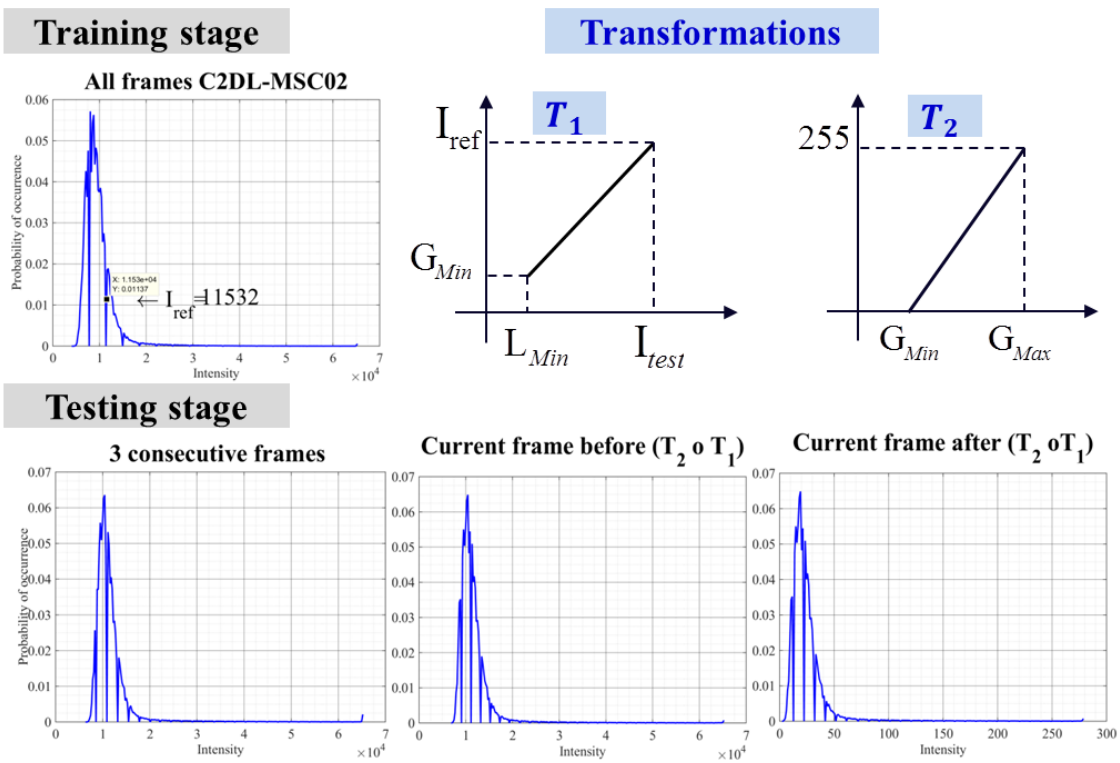

Figure 3.5: Histogram of all concatenated images of the C2DL-MSC02 dataset, and linear transformations and scaling of each pixel of the image (top row, left to right). The histogram of 3 consecutive frames that will be matched to the training dataset, and the histograms of the current frame before and after transformation $T(I(\omega)) = (T_2 \circ T_1)(I(\omega)), \quad \omega \in \Omega_{3F}$ (bottom row, left to right).

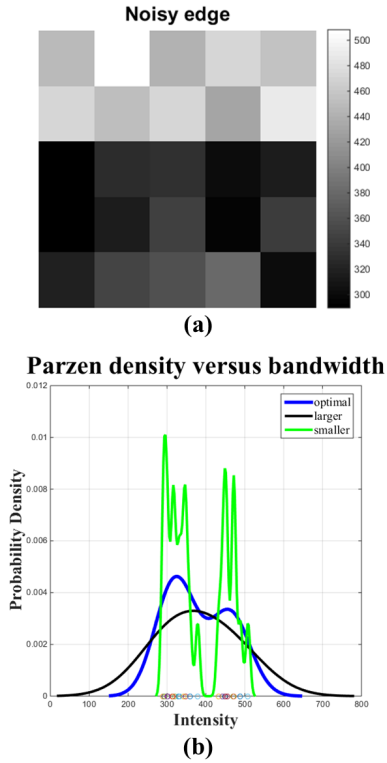

Figure 3.6: An example of (a) noisy edge detection using (b) nonparametric density estimation. Comparison of the Parzen density estimate for different bandwidth values of h on the same image intensity samples plotted on the horizontal axis. The optimal h value estimates the bimodality of the local intensity distribution. Use of smaller h is susceptible to statistical variability, while larger h will reduce the estimation accuracy.

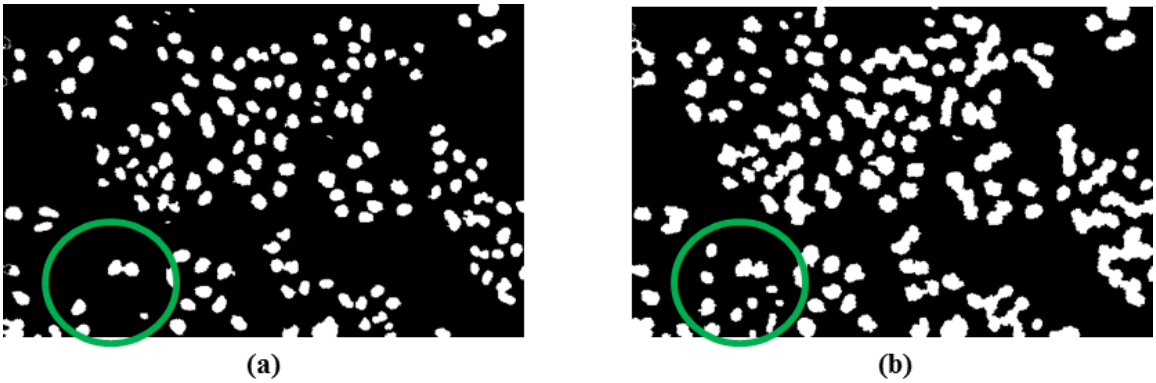

Figure 3.7: Comparison of detected cell masks using different Parzen bandwidth values on the same sample frame of a dense dataset. (a) Parzen bandwidth $h = 20$ showing some missing cells, (b) Parzen bandwidth $h = 2$ leads to better results as it can detect more cells than in (a).

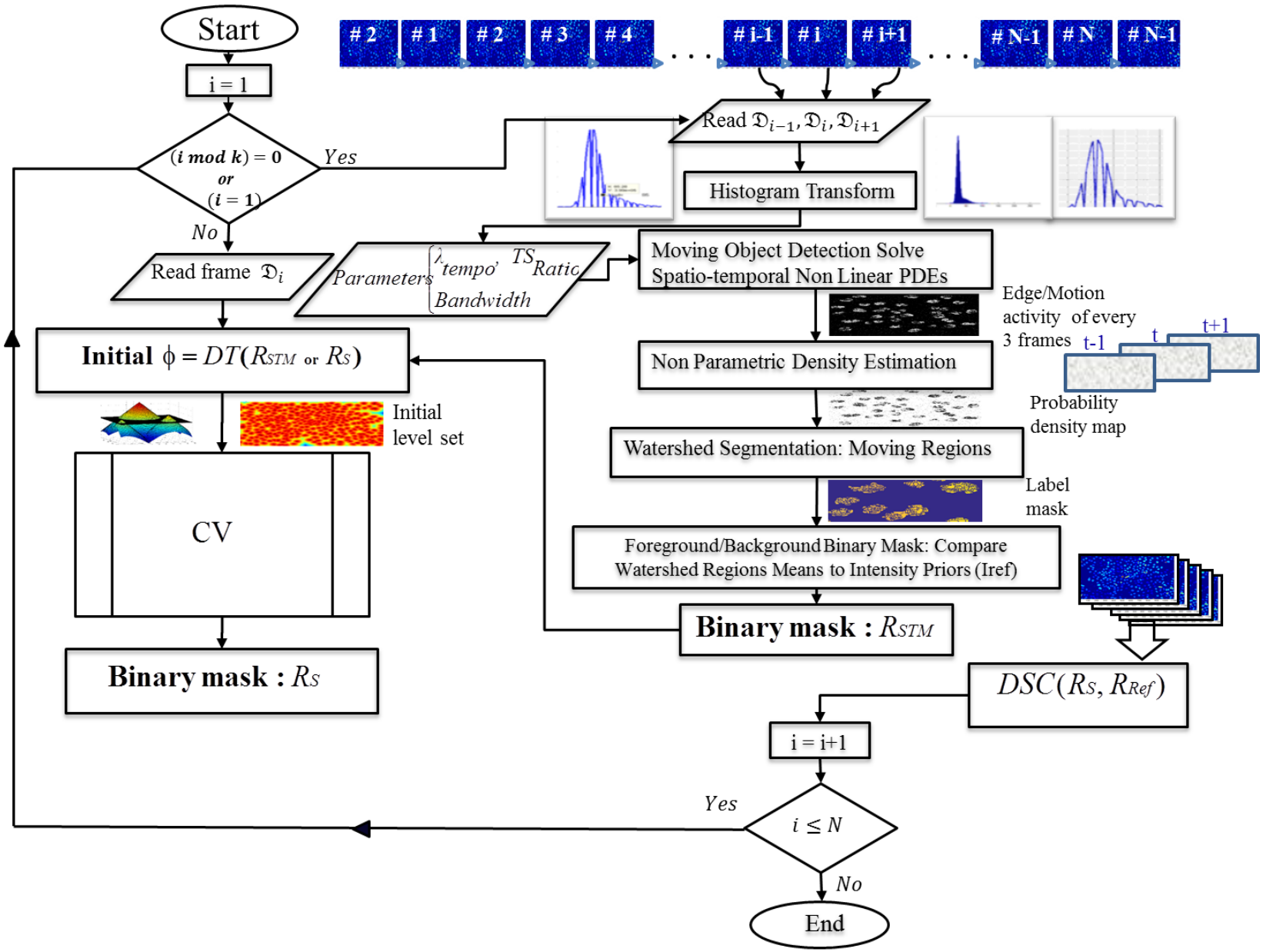

Figure 3.8: Outline of the proposed joint spatio-temporal nonlinear diffusion algorithm and temporally linked level sets methods (ST-Diff-TCV).

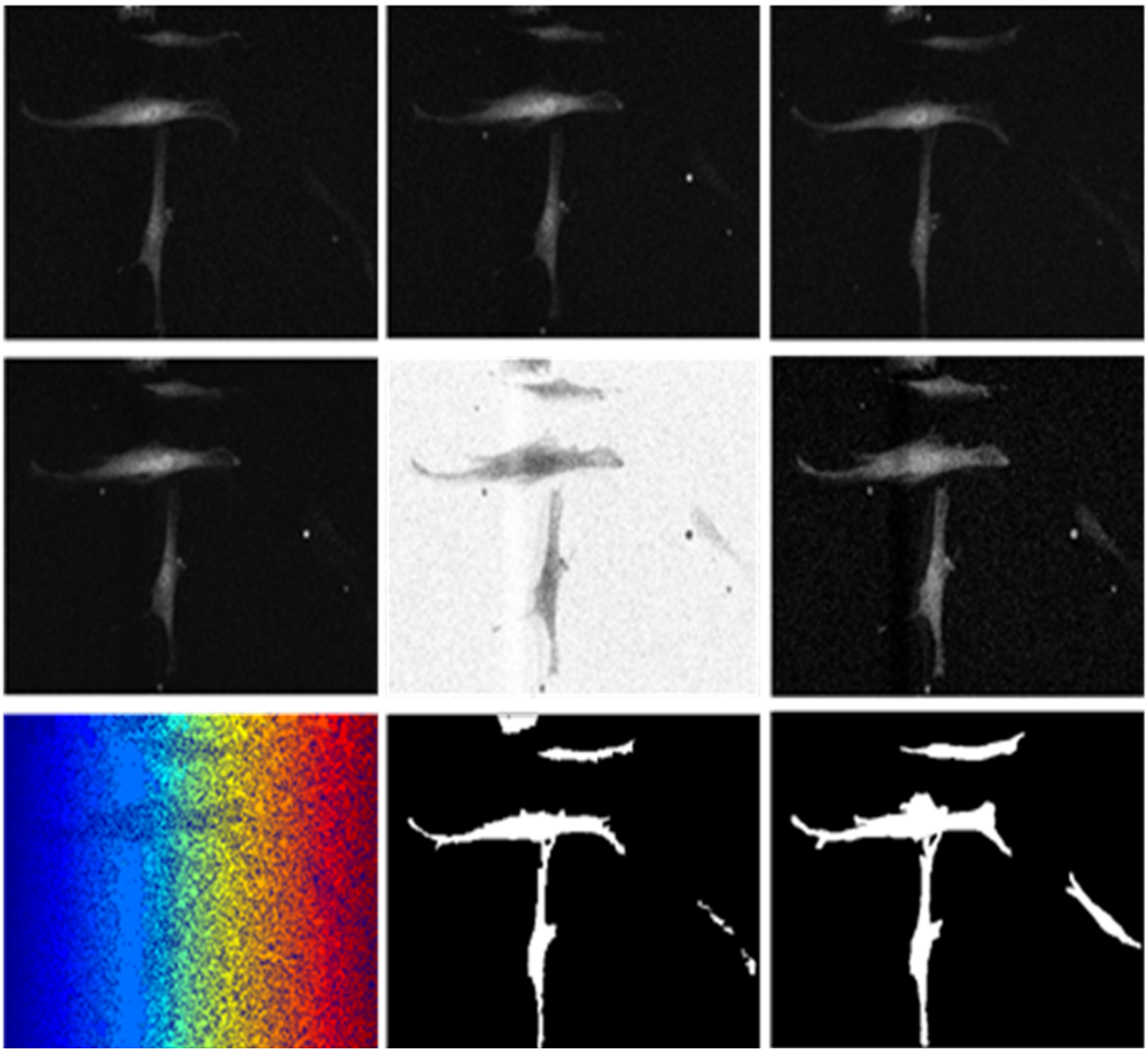

Figure 3.9: Intermediate results produced by ST-Diff-TCV on sample frames of C2DL-MSC02 data sequence. First row: center, previous and next frames in the temporal space (left to right) Second row: S-T diffused frame, kernel density estimation of edge-moving regions then the inverted probability density map. Third row: watershed result, cell identification after foreground/background separation, and the reference segmentation mask (left to right).

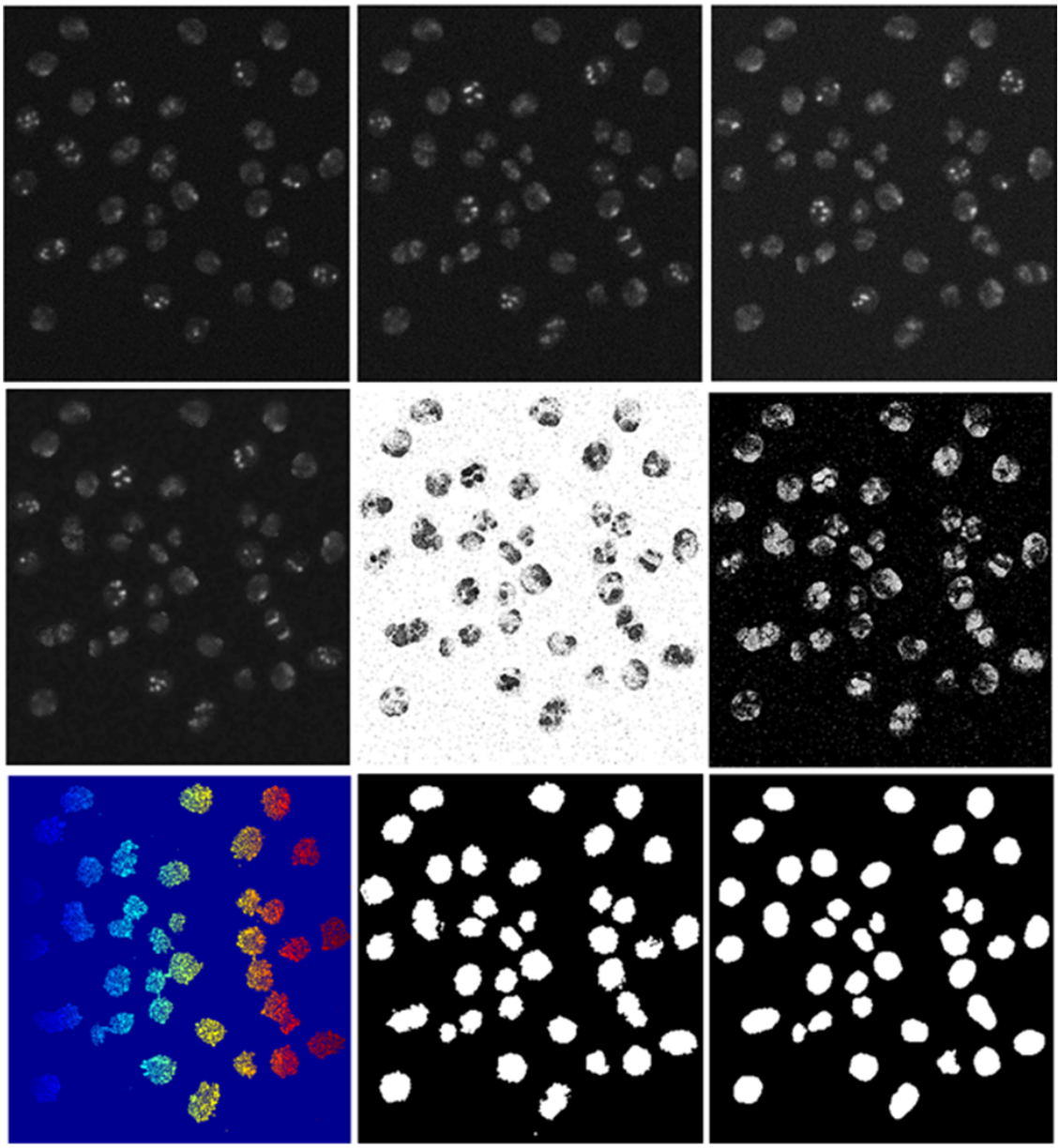

Figure 3.10: Intermediate results produced by ST-Diff-TCV on sample frames of Fluo-N2DH-SIM04 data sequence. First row: center, previous and next frames in the temporal space (left to right) Second row: S-T diffused frame, kernel density estimation of edge-moving regions then the inverted probability density map. Third row: watershed result, cell identification after foreground/background separation, and the reference segmentation mask (left to right).

Chapter IV: CELL SEGMENTATION EXPERIMENTS

4.1 Data Description

The datasets consist of 2D fluorescent microscope time-lapse image sequences. We used 12 time-lapse video sequences; 6 real microscopy time-lapse sequences and 6 computer simulated videos with various cell densities and noise levels. We obtained the training and challenge data sets from the cell tracking challenge website [25]. Simulated videos: The 6 simulated videos displayed fluorescently labeled nuclei of the HL60 (human promyelocytic leukemia) cell line migrating on a flat 2D surface (N2DH-SIM01, N2DH-SIM02, N2DH-SIM03, N2DH-SIM04, N2DH-SIM05, N2DH-SIM06). They differ in the level of noise, cell density of the initial population, the number of cells leaving and entering the field of view and the number of simulated mitotic events, yielding up to 70 cells in the field of view [25]. Real videos: We used 3 datasets each containing 2 time-lapse sequences. Two video sequences of Rat Mesenchymal stem cells (Fluo-C2DL-MSC01 and Fluo-C2DL-MSC02), also known as mesenchymal stem cells, are adult stem cells that can be found in the bone marrow or isolated from cord blood, peripheral blood, fallopian tube, fetal liver or lung. Cultured mesenchymal stem cells are an excellent tool for the study of adipocyte, osteocyte, and chondrocyte differentiation. The videos were acquired in the Cell Therapy Laboratory of Center for Applied Medical Research (CIMA) Pamplona, Spain. (Pixel size of 0.3977 x 0.3977 microns and Time step of 20 minutes for Fluo-C2DL-MSC1 and 30 minutes for Fluo-C2DL-MSC02. Two real video sequences named N2DH-GOWT101 and N2DH-GOWT102 of mouse embryonic stem cells in $2D$ obtained by the Institute of Biophysics Academy of Sciences of the Czech Republic. Brno. Czech Republic acquired using, Pixel size of 0.240 x 0.240 microns and time step of 5 minutes between each frame. Two video sequences named N2DL-HeLa01 and N2DL-HeLa02 expressing HeLa cells in $2D$ with pixel size of 0.645 x 0.645 microns and Time step of 30 minutes between each frame. A HeLa cell, is the oldest and most commonly used human cell

line derived from cervical cancer cells. The cell line was found to be remarkably durable and prolific which makes these datasets considered to have high level of difficulty [25] because of the high cell density and mitoses events yielding up to 300 cells in the field of view and low resolution and intensity. A sample frame of each dataset is displayed in Figure 4.1.

4.2 Intensity Distributions of Time-lapse Sequences

As we have described before, the datasets are characterized by intensity variability that complicates the segmentation stages. This effect may be more pronounced in differential approaches. We propose to reduce the variability within a time-lapse sequence and among different time-lapse sequences using a statistical learning technique to perform intensity histogram transformation.

In Figures 4.2 and 4.3 we display the computed global intensity histograms for our simulated and real image sequences respectively. We also display the PDF and CDF of these sequences. We note that the original distributions have clear differences in first and second order statistics. We propose to use reference points that are learned on the CDF of the global sequence to transform the intensity histograms of the individual frames. The goal is to address translation and scaling variations between distributions and accomodate the application of methods based on finite spatio-temporal differences. This is the case for the spatio-temporal diffusion differential techniques and level-set approaches.

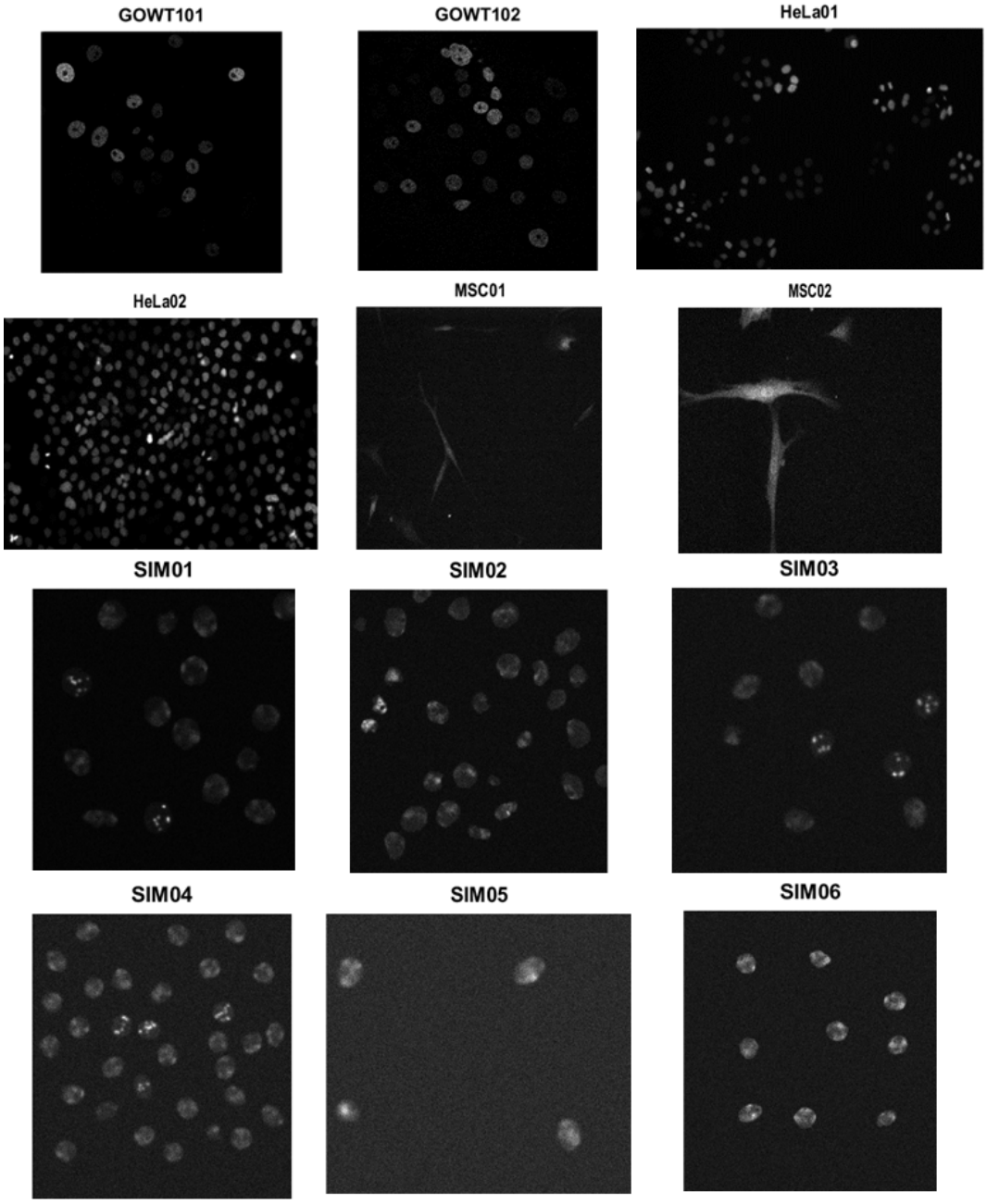

Figure 4.1: The 6 real and 6 simulated time-lapse sequences used for validation.

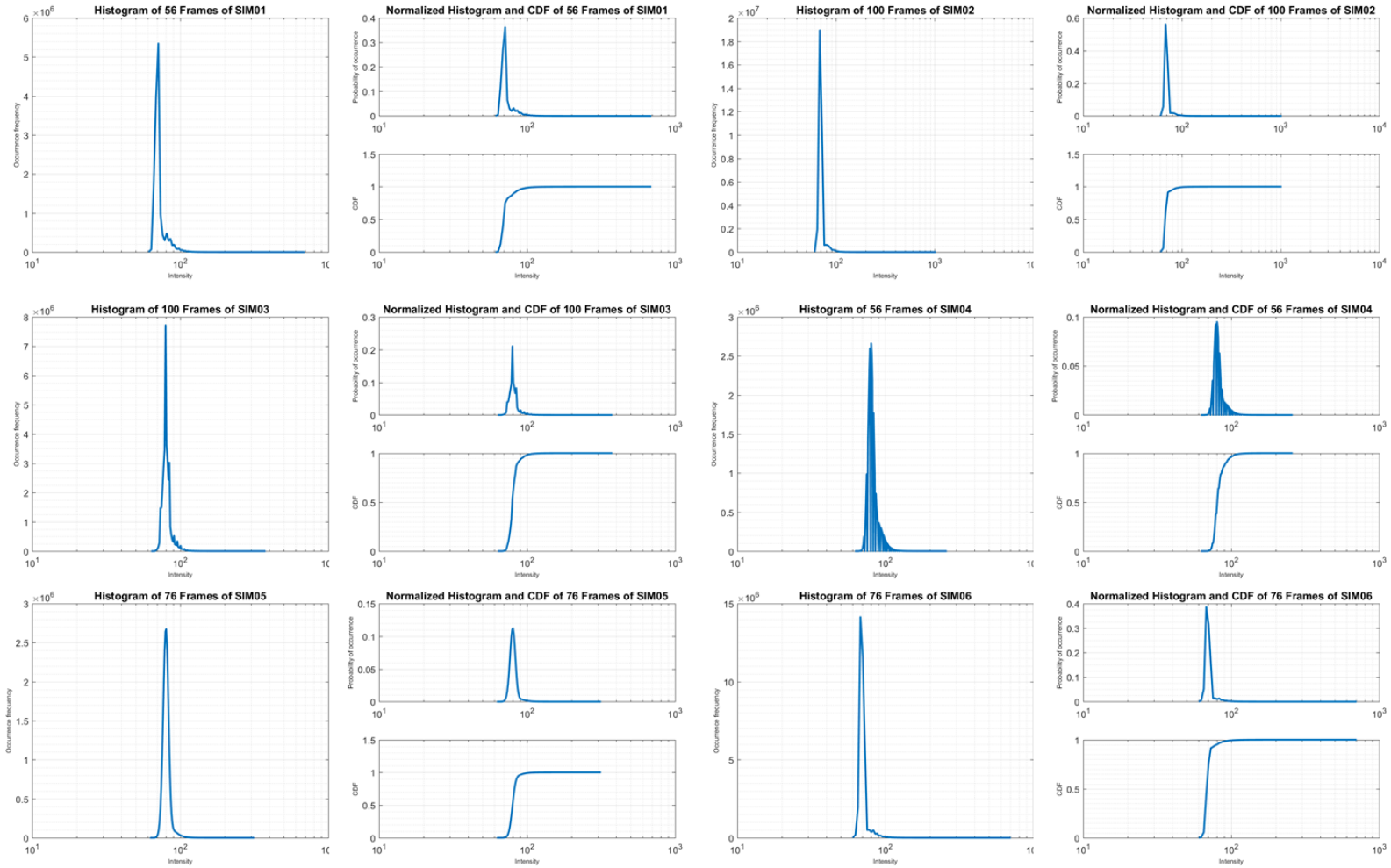

Figure 4.2: PDF and CDF of all the concatenated frames of each sequence of the simulated datasets.

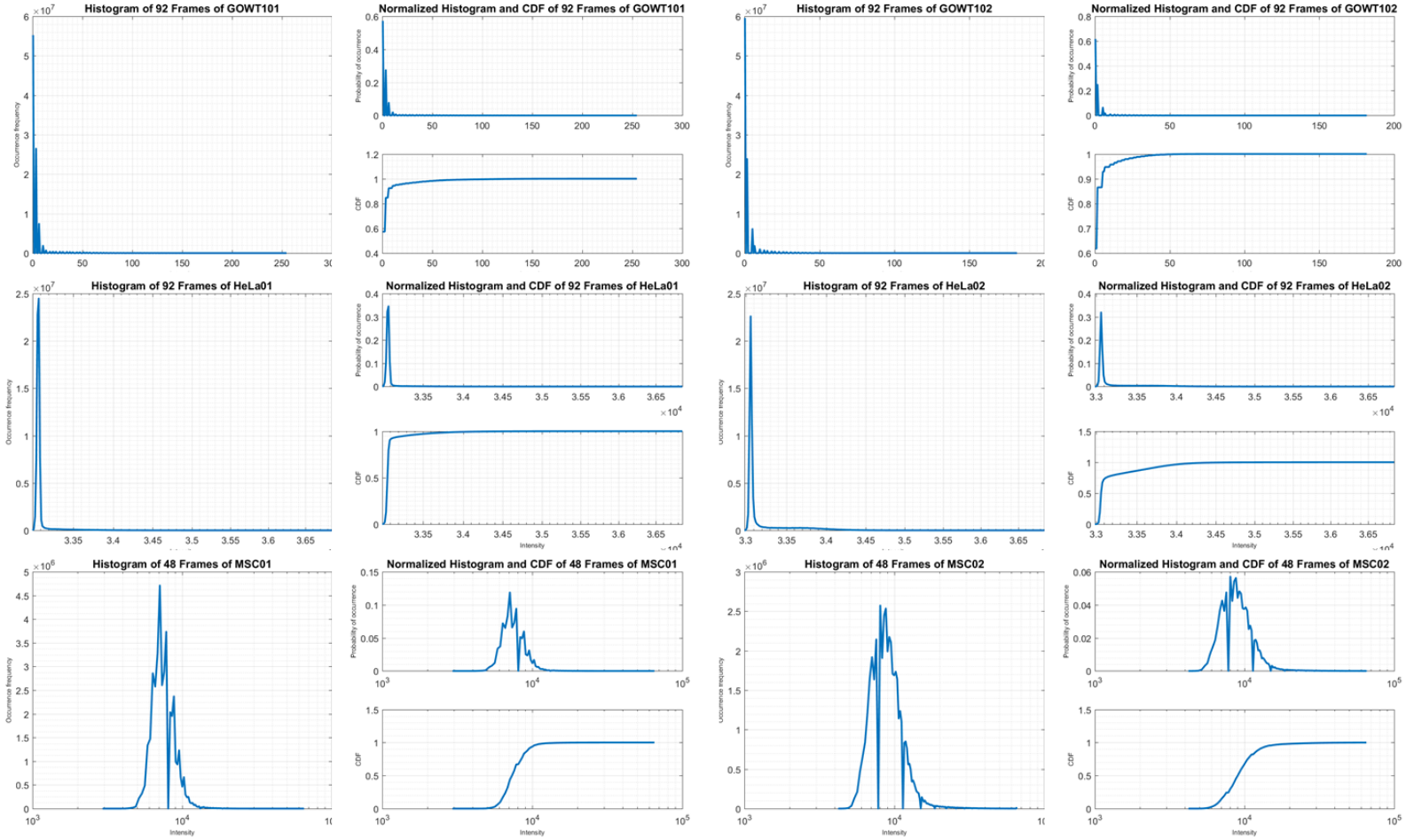

Figure 4.3: PDF and CDF of all the concatenated frames of each sequence of the real datasets.

4.3 Generation of Reference Data for Segmentation [25]

One expert from CIMA-ES (Center for Applied Medical Research, España) annotated all the real datasets used in the training phase. The real videos were manually annotated by three experts from three sites, CBIA-CZ (Center for Biomedical Image Analysis part of the national research infrastructure Czech-BioImaging) and ERASMUS-NL(Erasmus University Rotterdam, Netherlands).

The task for annotators was to mark grid points belonging to cells as accurately as possible. Therefore, each cell was segmented as a set of grid points with the same unique label. The length of the videos and the high number of cells per frame in some of the datasets prevented from having a complete manual annotation of all the cells. Therefore, all the frames of each video were first randomly permutated to select the cells that were used as ground truth. The segmentation masks were drawn in the entire image frame. The annotators were asked to identify and annotate cells that in their opinion were prone to causing segmentation problems, such as cells undergoing abnormal mitoses, dimly stained cells, oddly shaped cells and colliding pairs of cells. They segmented at least 20 instances of each problematic event.

4.4 Image Quality Assessment of Datasets

In our first experiment, we measured the image quality (IQ) of our datasets and then evaluated the segmentation accuracy. We utilized the available reference data for this purpose. The reference data consist of manually annotated videos for segmentation and tracking along with a short description and links to the raw datasets obtained from [25]. We first used the reference data to estimate the average Signal-to-Noise Ratio (SNR) and Contrast-to-Noise Ratio (CNR) of each dataset. The SNR and CNR measures are defined as follows:

$$SNR = 20 \log_{10} \frac{\bar{u}_C}{\bar{u}_B}, \tag{4.1}$$

$$CNR = \frac{|\bar{u}_C - \bar{u}_B|}{\sigma_B}, \tag{4.2}$$

where $\bar{u}_C$ is the average image intensity over the cell regions, $\bar{u}_B$ is the average intensity over the background and σ_B is the standard deviation of the background pixels. In Table 4.1 we list the average SNR (in dB) and average CNR that are means over all frames in each sequence using (4.1) and (4.2) and corresponding standard deviations of each dataset over cell regions. Summarized information on our test data image quality metrics and the level of difficulty is listed in Table 4.1, including the image matrix size, voxel size, time step in minutes, the number of frames in each sequence. A comparison between the level of difficulty and the image quality metrics in Table 4.1 shows that the simulated sequences have higher SNR and CNR, therefore being more amenable to segmentation than the real sequences.

Table 4.1: Dataset properties and quality using Signal-to-Noise Ratio (SNR) and Contrast-to-Noise Ratio (CNR)

Dataset name	Frame size	Voxel size (μm)	Average SNR	Average CNR	Time step (min)	Level of difficulty
N2DH-SIM01	494x534	0.125x0.125	21.53 ± 0.69	7.96 ± 0.95	-	***Medium:***different noise levels, cell density of the initial population and number of simulated mitotic events.
N2DH-SIM02	569x593	0.125x0.125	22.21 ± 0.65	8.35 ± 0.96	-	
N2DH-SIM03	606x605	0.125x0.125	18.59 ± 0.47	4.21 ± 0.47	-	
N2DH-SIM04	673x743	0.125x0.125	18.97 ± 0.47	4.09 ± 0.49	-	
N2DH-SIM05	597x525	0.125x0.125	19.49 ± 0.54	4.22 ± 0.60	-	
N2DH-SIM06	655x735	0.125x0.125	21.92 ± 0.54	7.90 ± 0.78	-	
C2DL-MSC01	992x832	0.397x0.397	14.67 ± 0.67	2.11 ± 0.36	20	***High:***low SNR, cell stretching appear as discontinuous extensions of the cells.
C2DL-MSC02	1200x782	0.397x0.397	15.09 ± 2.31	4.47 ± 1.49	30	
N2DL-HeLa01	1100x700	0.644x0.644	26.60 ± 3.41	19.23 ± 7.67	30	***High:***high cell density, low resolution, frequent mitoses events (normal and abnormal).
N2DL-HeLa02	1100x700	0.644x0.644	16.02 ± 1.67	5.40 ± 1.08	30	
N2DH-GOWT101	1024x1024	0.240x0.240	22.47 ± 0.49	12.62 ± 0.77	5	***Medium:***heterogeneous staining, prominent nuclei, mitoses and cells entering leaving the field of view.
N2DH-GOWT102	1024x1024	0.240x0.240	18.91 ± 0.92	8.32 ± 0.91	5	

4.5 Segmentation Evaluation Measure

We compute DICE coefficients to estimate the segmentation performance between each method and the reference manual segmentations. The main purpose is to evaluate how well the segmented cells match the cell regions of the reference mask. We quantify the accuracy of the segmentation performance by computing the DICE similarity coefficient denoted by DSC. This is defined as:

$$DSC = 2 \times \frac{|R_S \cap R_{Ref}|}{|R_S| + |R_{Ref}|} \in [0, 1], \tag{4.3}$$

where R_{Ref} is the set of all pixels that belong to cell regions in the reference image, R_S is the set of all binary regions delineated by the tested segmentation technique. The DICE coefficient measures the relative similarity between two binary images over their cardinalities. It is frequently used for image segmentation validation. The value of 1 indicates perfect matching. Figure 4.4 displays an example of cell regions used to compute the Dice coefficient.

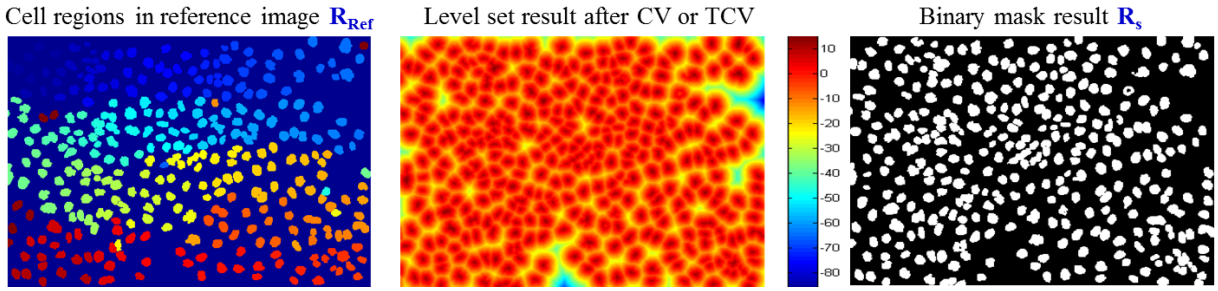

Figure 4.4: Cell regions used to compute the Dice coefficient (DSC). R_s is the set of all binary regions delineated by our segmentation technique. R_{Ref} set of all pixels that belong to cell regions in the reference image.

4.6 Validation and Comparison of CV and TCV

In the first experiment we segmented the test sequences using CV method and TCV approach.We segmented each dataset using each method and evaluated the segmentation per-

formance against reference masks. We computed means and the standard deviations of DICE scores obtained by CV and TCV methods over all frames for each sequence as displayed in Figure 4.5. Overall the accuracy in DICE scores derived from the linking method appears to be similar in value with that obtained from CV method. However, there is a clear difference in the values of the standard deviation. That is, the standard deviations obtained from the temporal-linking method (0.006-0.1) are significantly smaller than those derived from the CV method (0.02-0.4), indicating better convergence and stability.

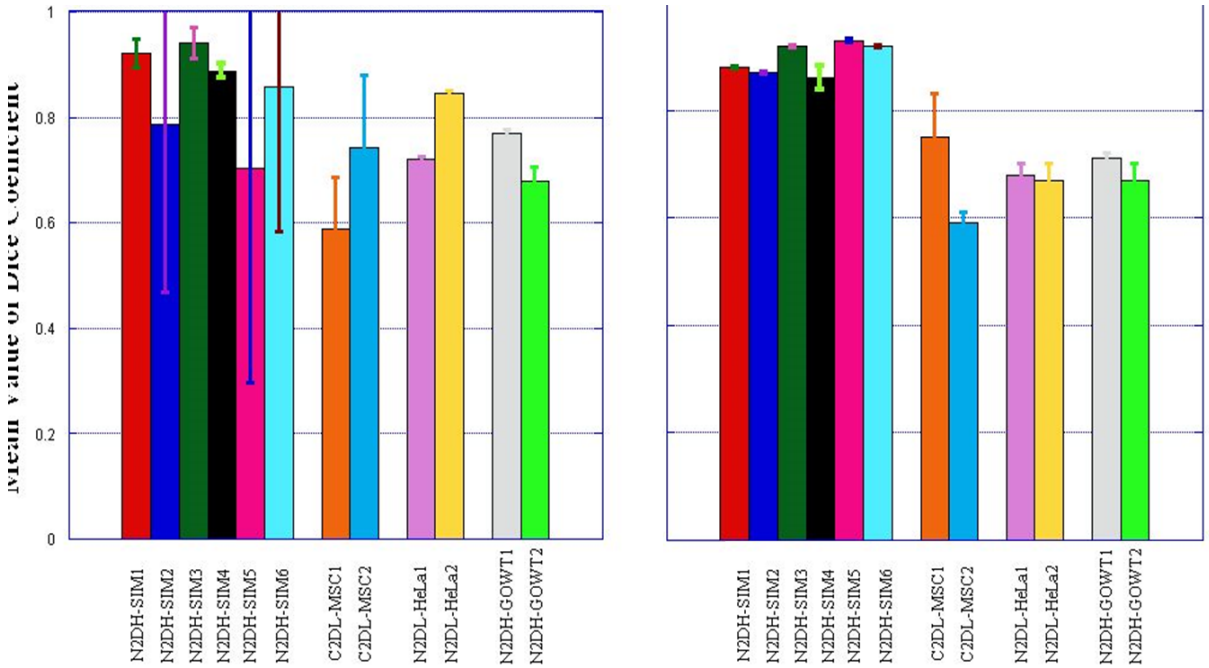

Figure 4.5: Segmentation accuracy produced by the original CV algorithm (left) and the temporally linked level-sets (right).

Better insight into the improvement from the temporal-linking method can be obtained by looking at frame-by-frame segmentation and convergence. Consider the Fluo-N2DH-SIM5 dataset, for example. In Figure 4.6 we show the frame by frame DSC score results of energy minimization derived using the CV and temporal-linking methods. Because of the non-convexity of the energy functional (allowing therefore many local minima), the CV method reached on some frames a local minimum of energy where, however, the moving

contour got trapped. In contrast, the temporal-linking method led to a global minimum of the energy, yielding the actual cell regions. The mean number of iterations necessary to perform segmentation of all the frames provides better insight into the convergence of both methods. Here Figure 4.6 shows changes of the DICE coefficient for each frame. In particular, notice the abrupt drop of the coefficient and the index to values very close to zero on certain frames when using the CV method, whereas DICE scores produced by the temporal-linking method appear robust indicating improved robustness.

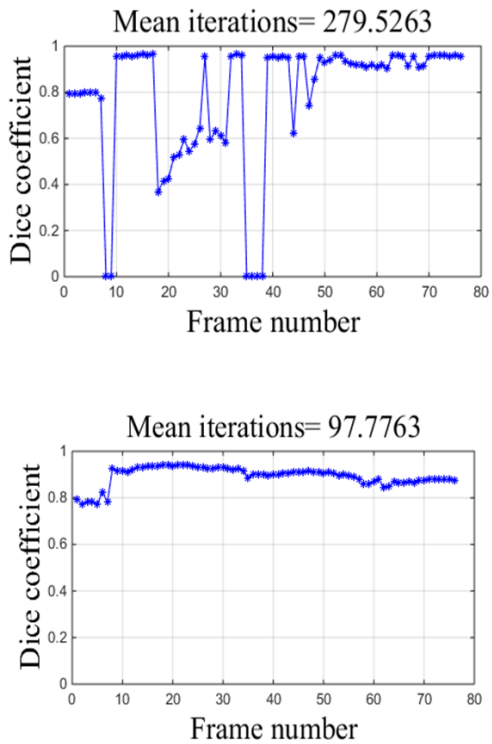

Figure 4.6: Comparison of the DICE coefficient of each frame (total frame=77) of the Fluo-N2DH-SIM5 data using the traditional CV segmentation (top) and the temporal-linking method (TCV) (bottom). We note the greater DICE scores and faster convergence of the proposed method.

Another consideration in our comparisons was the number of iterations until convergence. Figure 4.7 the number of iterations required to achieve segmentation of one sample image of N2DL-Hela2 dataset by (a) the standard CV segmentation (b) the temporal linking method. We observe a significant reduction in the number of iterations (from 5000 to 173),

because the initial level-set is very close to the actual regions to segment. However, the DICE score produced by the temporally linked level-set is lower than the one produced by the CV method. As indicated in Table 4.2, this dataset has a high level of difficulty due to the high density and especially the frequent mitoses, low resolution and low fluorescence intensity. In this case, we encountered the temporally linked level-set converges significantly faster than CV. The local minimum is reached in a few iterations compared to the proposed technique that reaches a more accurate solution. Building upon the previous observation, we tested our hypothesis of faster convergence on our complete set of sequences. We report the average number of iterations used to achieve segmentation of the cells for each dataset over all the frames in Table 4.2. This table demonstrates the major reduction of the computational time for minimizing the energy with the use of the temporal linking method that is equal to a factor of 10.2. This reduction is achieved by exploiting the previously computed level-set and using it for initializing the values for the minimization of the current image with possible guessing of the initial values as implemented in the CV method.

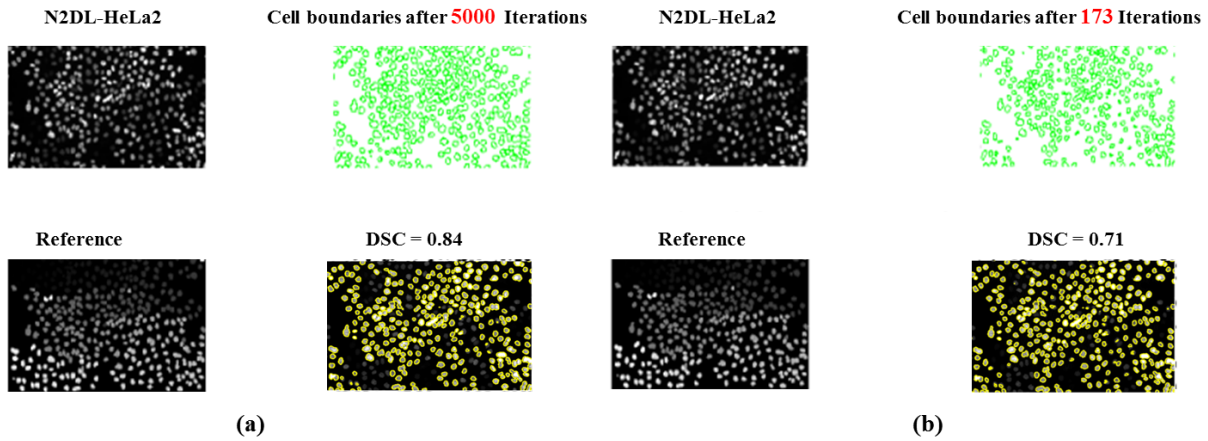

Figure 4.7: Comparison between the number of iterations to required to obtain segmentation result of one sample frame of C2DL-Hela2 dataset using (a) CV and (b) TCV methods.

The previous observation can be explained in terms of the energy minimization. Depending on several factors, the energy can sometimes converge to a local energy minimum

without reaching the desired global energy minimum. The contour may sometimes stop its evolution before reaching the desired boundaries. In particular cases the splitting of the cells is not delineated correctly; this case is very often en-countered in cell segmentation. In some cases, especially in MSC data, stretched cells can leave a trace which can be detected by single or few pixel objects which may be misdelineated as a cell. Since our energy function is non-convex, allowing therefore many local minima, conventional CV initialization may lead to premature convergence to a local minimum and segmentation errors.

Table 4.2: The mean number of iterations required to achieve segmentation of each sequence by both methods: CV and TCV

Dataset name	Frame size	Nb frames	Nb iterations CV	Nb iterations TCV
N2DH-SIM01	494x534	56	261	**106**
N2DH-SIM02	569x593	100	1088	**88**
N2DH-SIM03	606x605	100	412	**96**
N2DH-SIM04	673x743	56	456	**43**
N2DH-SIM05	597x525	76	279	**97**
N2DH-SIM06	655x735	76	228	**72**
C2DL-MSC01	992x832	48	240	**104**
C2DL-MSC02	1200x782	48	343	**224**
N2DL-HeLa01	1100x700	92	1039	**67**
N2DL-HeLa02	1100x700	92	4470	**82**
N2DH-GOWT101	1024x1024	92	322	**64**
N2DH-GOWT102	1024x1024	92	2469	**141**
Mean			998	**98**

4.7 Validation and Comparison of CV, TCV, ST-Diff, and ST-Diff-TCV Methods

We applied the standard CV, TCV, ST-Diff, and ST-Diff-TCV methods on 12 time-lapse fluorescent microscopy datasets listed in Table 4.1. Fluorescent microscopy imaging is often

times subjected to a mixture of different types of noise. The main goal of a preprocessing step is to reduce the corruption caused by noise and to improve the image quality [85]. To facilitate data analysis, a combination of filters and histogram enhancement is applied to the datasets to obtain better delineation accuracy.

We computed the DICE coefficient between the automated and reference segmentations for each method and for each dataset. Further, we computed the means and the standard deviations of the DICE similarity coefficients over all frames for each dataset sequence. Figure 4.8 and Table 4.3 report the DSC estimates and their variations for each sequence. In addition, the last row in Table 4.3 lists the overall DSC values for all datasets. In Figure 4.8 and Table 4.3 we observe that ST-Diff-TCV yields higher DSC values for 11 out of the 12 test sequences. ST-Diff-TCV yields an average Dice coefficient of 0.89 over all datasets, while both CV and TCV yield 0.78, and ST-Diff yields 0.85 (Table 4.3). Furthermore, the standard deviation values in Table 4.3 show more robustness and stability. That is, the standard deviations obtained from ST-Diff and ST-Diff-TCV (0.01-0.03) are significantly smaller than those derived from the CV method (0.01-0.4) and even TCV (0.02-0.08) indicating better convergence and stability.

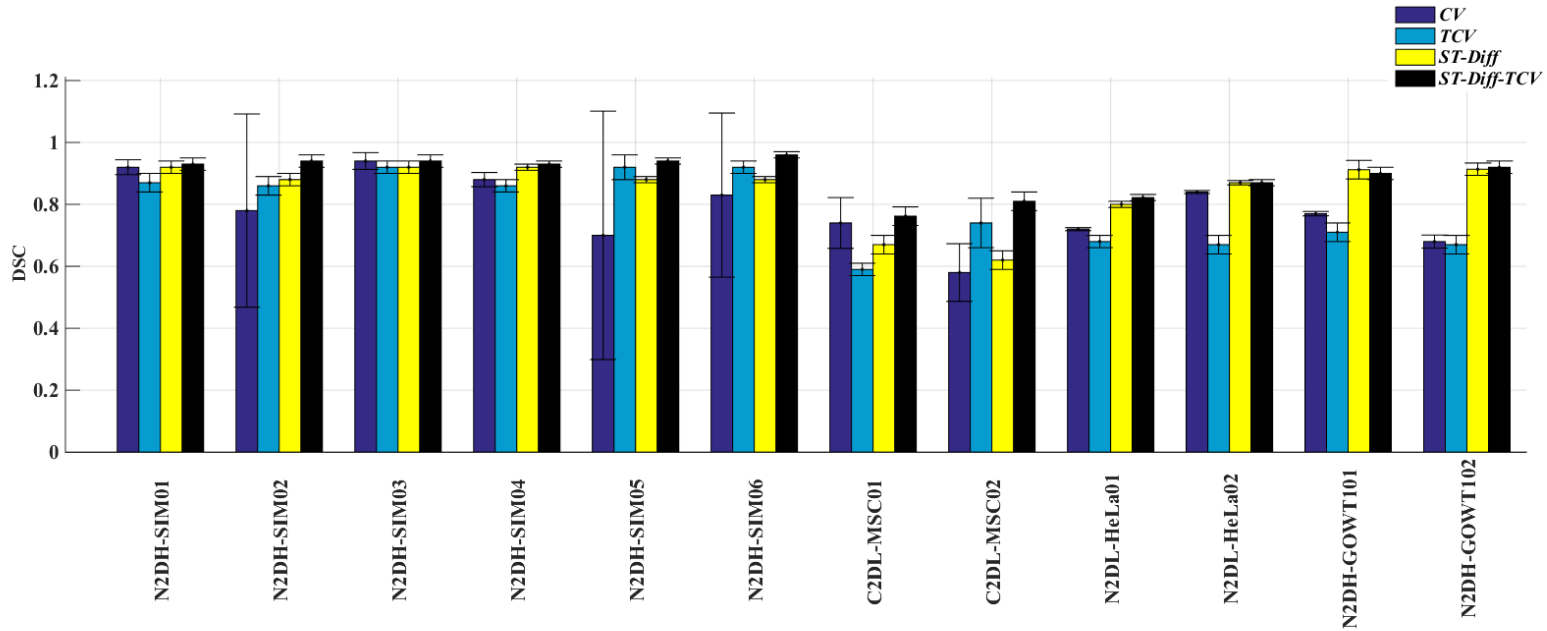

Figure 4.8: Dice similarity coefficients (DSC) produced by standard Chan−Vese model (CV), temporally linked Chan−Vese technique (TCV), spatio−temporal diffusion (ST−Diff), and the joint ST−Diff−TCV methods over all 12 datasets.

Table 4.3: The mean DICE coefficient obtained from segmentation of each sequence by CV, TCV, ST-Diff, and the joint ST-Diff-TCV method

Dataset name	Size	Frames	CV	TCV	ST-Diff	ST-Diff-TCV
N2DH-SIM01	494x534	56	0.92 ± 0.02	0.87 ± 0.03	0.92 ± 0.02	**0.94 ± 0.02**
N2DH-SIM02	569x593	100	0.78 ± 0.31	0.86 ± 0.03	0.88 ± 0.02	**0.94 ± 0.02**
N2DH-SIM03	606x605	100	**0.94 ± 0.03**	0.92 ± 0.02	0.92 ± 0.02	**0.94 ± 0.02**
N2DH-SIM04	673x743	56	0.88 ± 0.02	0.86 ± 0.02	0.91 ± 0.01	**0.93 ± 0.01**
N2DH-SIM05	597x525	76	0.70 ± 0.40	0.92 ± 0.04	0.88 ± 0.01	**0.94 ± 0.01**
N2DH-SIM06	655x735	76	0.83 ± 0.27	0.92 ± 0.02	0.88 ± 0.01	**0.96 ± 0.01**
C2DL-MSC01	992x832	48	0.74 ± 0.08	0.59 ± 0.02	0.67 ± 0.03	**0.76 ± 0.03**
C2DL-MSC02	1200x782	48	0.58 ± 0.09	0.74 ± 0.08	0.62 ± 0.03	**0.81 ± 0.03**
N2DL-HeLa01	1100x700	92	0.72 ± 0.01	0.68 ± 0.02	0.80 ± 0.01	**0.82 ± 0.01**
N2DL-HeLa02	1100x700	92	0.84 ± 0.01	0.67 ± 0.03	**0.87 ± 0.01**	**0.87 ± 0.01**
N2DH-GOWT101	1024x1024	92	0.77 ± 0.01	0.71 ± 0.03	**0.91 ± 0.03**	0.90 ± 0.02
N2DH-GOWT102	1024x1024	92	0.68 ± 0.02	0.67 ± 0.03	0.91 ± 0.02	**0.92 ± 0.02**
Mean *DSC*			0.78	0.78	0.85	**0.89**

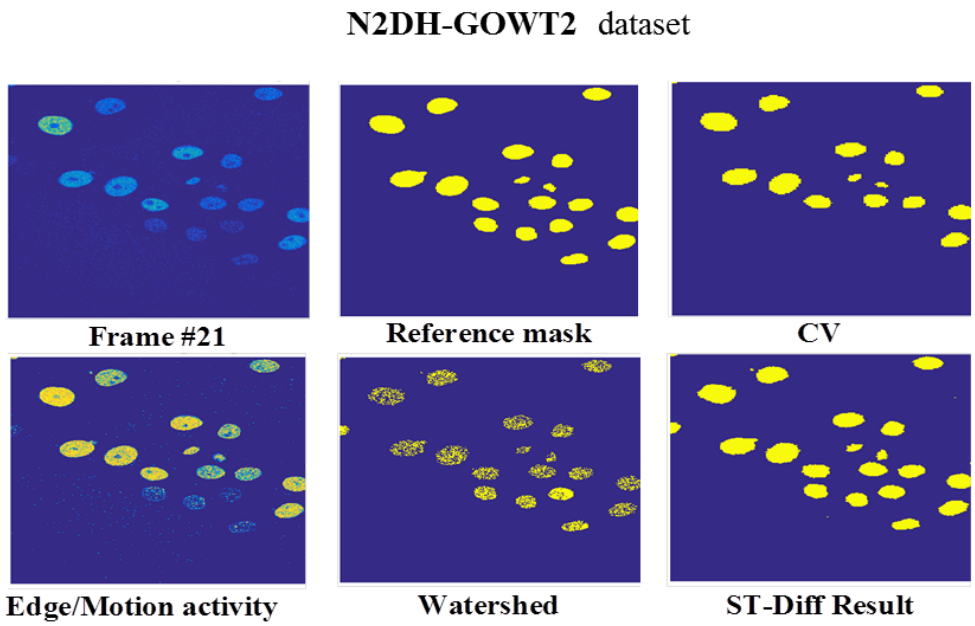

Figure 4.9: CV versus ST-Diff Segmentation on Mouse Stem Cells N2DH-GOWT102 dataset.

In some of our datasets, the fluorescent images present less bright nuclei or cells darker than the background where there is absorption rather than fluorescence. Certain darker cell regions have mean intensity lower than the mean intensity of the background like in MSC1, N2DH-GOWT1-01 and N2DH-GOWT1-02 data sequences. We were able to detect those cells by the motion estimation which significantly improves the segmentation accuracy from 0.77 to 0.91 and 0.68 to 0.913. This is simply performed by choosing a threshold lower than mean intensity of the reference background where we had to choose a factor and 1/3 for N2DH-GOWT1-01 and N2DH-GOWT1-02 respectively. Hence, the region competition process fails to delineate those cells. However, these cells are detected by the spatio-temporal motion detection method because they are rather detected by their high activity process and the Threshold factor for background as shown in Figure 4.9, which is proven to be more efficient in this case.

To illustrate the performance comparison among the three tested methods in more

detail, we show in Figure 4.10, the results derived from CV, TCV, ST-Diff, and ST-Diff-TCV methods on N2DH-SIM02 and N2DH-SIM04 datasets. In the N2DH-SIM02 sequence (Figure 4.10(a)), we observe that because of the non-convexity of the energy functional (allowing therefore many local minima), the CV method reached several local minima of energy. In contrast, the TCV method led to a global minimum of the energy. ST-Diff-TCV method yields accurate delineation of the cells with fewer fluctuations in the Dice coefficient than the other methods. We note that ST-Diff-TCV yields an average Dice coefficient of 0.94, while CV yields 0.78, TCV yields 0.86, and ST-Diff yields 0.88. In the N2DH-SIM04 dataset as displayed in Figure 4.10(b) we observe that ST-Diff-TCV produces the highest accuracy at a DSC value of 0.93, followed by ST-Diff, CV and TCV with Dice coefficients of 0.91, 0.88 and 0.86 respectively.

Furthermore, Figure 4.11 displays cell delineations represented by yellow contour maps for one frame of the sequence N2DL-Hela2 including the manual reference, and automated segmentation produced by all tested methods. This sequence has an increased level of difficulty because of the high cell density and low contrast between some cells and the background. Because CV and TCV methods use piecewise constant approximations for object and background as can be seen in (3.15), the low contrast cells are likely to be falsely identified as background therefore reducing DSC (CV: 0.84, TCV: 0.67). On the other hand, both ST-Diff and ST-Diff-TCV identify the spatio-temporal discontinuities and detect the cells that are missed by CT and TCV as outlined by white rectangles in Figure 4.11. In the magnified local regions of the test image we note that ST-Diff-TCV yields more accurate cell separation for adjacent cells than ST-Diff.

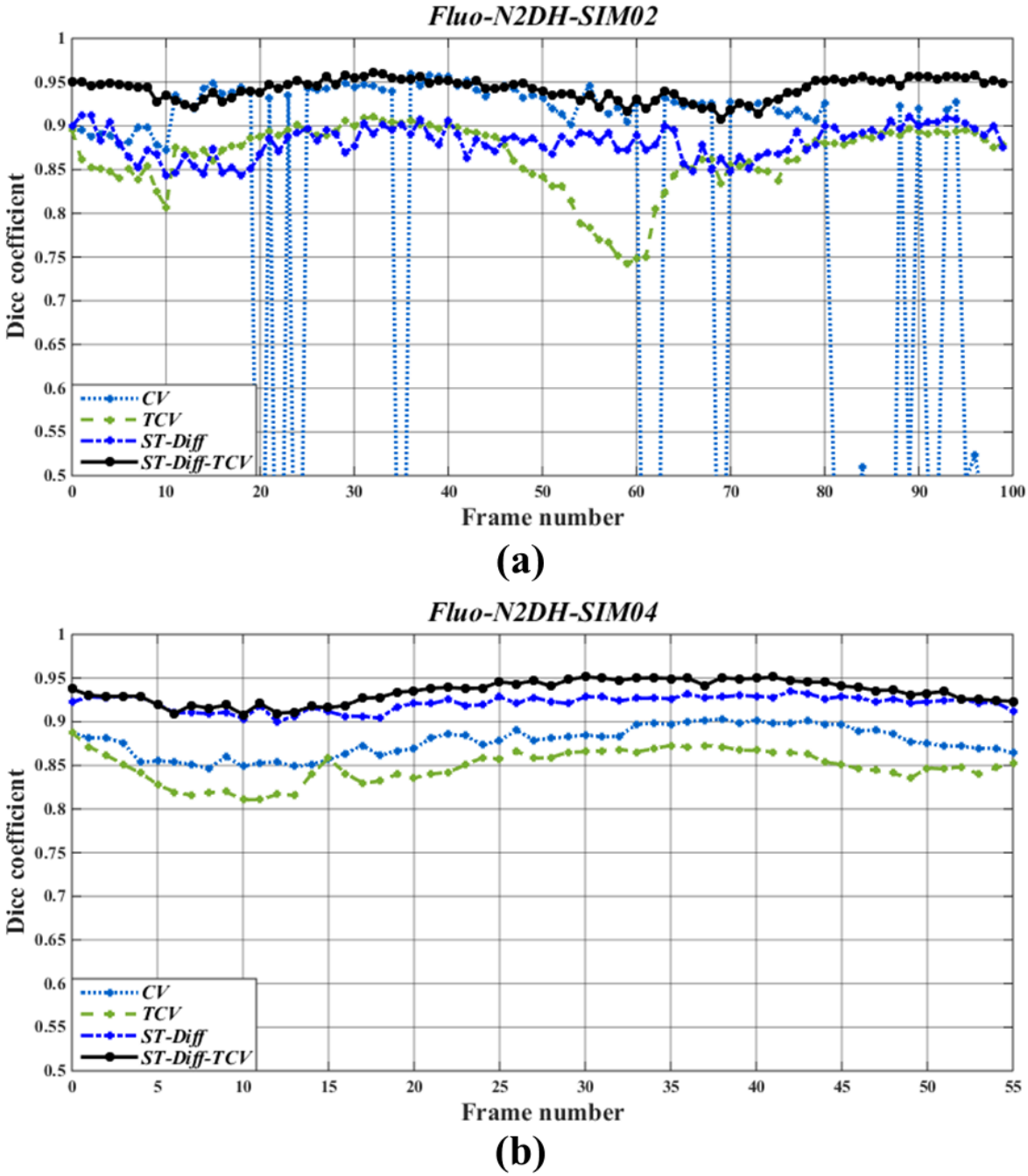

Figure 4.10: Dice similarity coefficients (DSC) produced by standard Chan-Vese segmentation (CV), temporally linked Chan-Vese technique (TCV), spatio-temporal diffusion (ST-Diff), and the joint ST-Diff-TCV methods for each frame of (a) N2DH-SIM02 and (b) N2DH-SIM04 datasets.

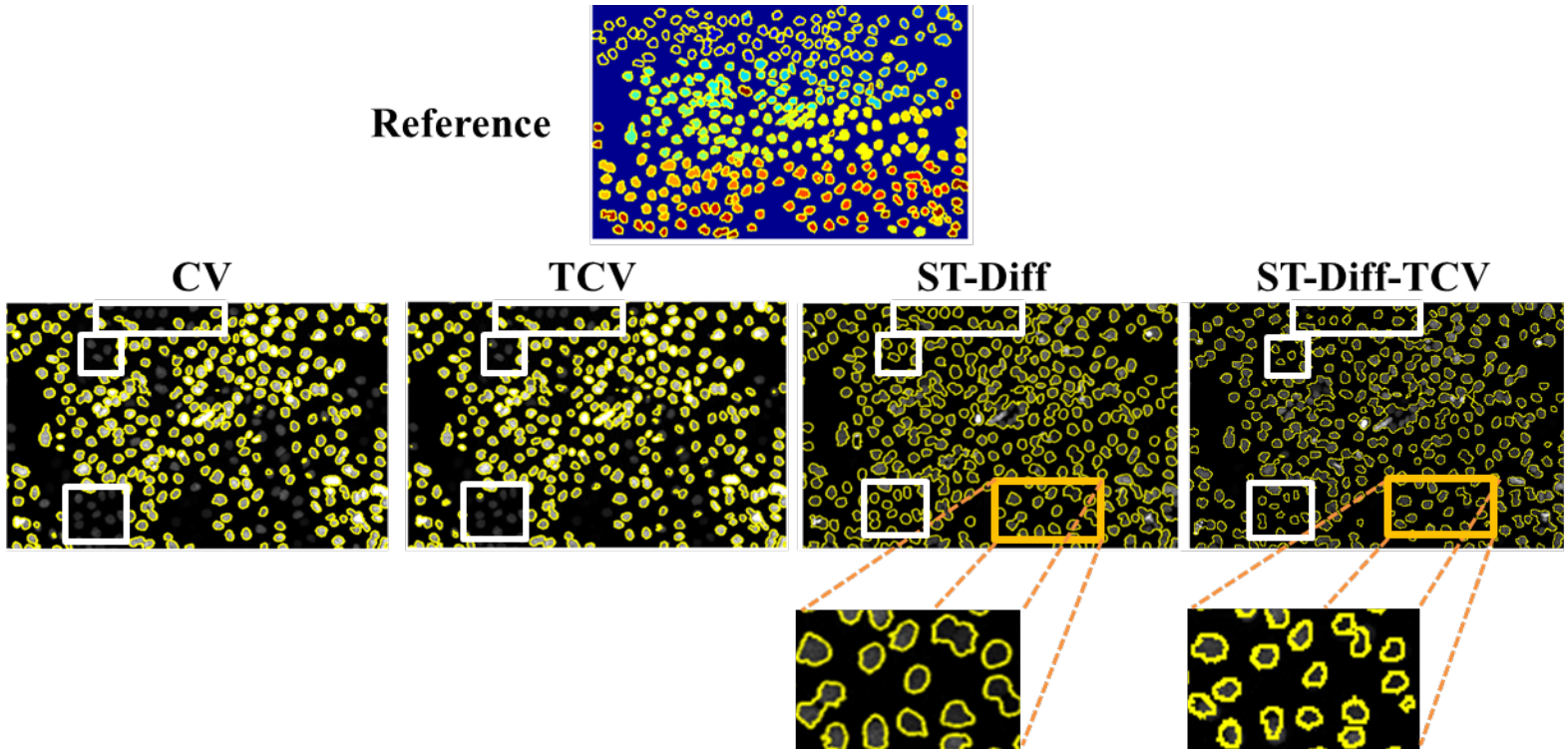

Figure 4.11: Cell boundaries produced by the 4 tested methods on N2DL-HeLa02 sequence frame. The spatio-temporal analysis enables the identification of more moving cells than the level-set models. Furthermore, ST-Diff-TCV produces more accurate cell separation than ST-Diff (magnified regions).

In some of our datasets, the fluorescent images contain low intensity nuclei where there is absorption rather than fluorescence in local parts of the same image resulting in heterogeneous cell intensity levels. These darker regions have low intensity that can be mis-detected as background. As a result the region competition process would fail to delineate them. However, these cells are identified by the spatio-temporal motion analysis method because of their high temporal activity, which is proven to be more efficient in these cases. For example, we observed that CV was not able to detect some cells with very low intensity in both N2DL-Hela and N2DH-GOWT sequences. Conversely, those cells were very well delineated using the temporal differences between frames, i.e., by ST-Diff-TCV, thus significantly improving the segmentation accuracy from 0.72 to 0.82 for N2DL-Hela01, and from 0.68 to 0.92 for N2DH-GOWT102 leading to DSC improvements up to 24% (Table 4.3).

On the other hand, the proposed technique involves parameters which are experimentally determined for each sequence. These are TS_{Ratio}, λ_t for motion diffusion, μ region length regularization weight for TCV segentation, the Parzen kernel parameters $Parzen_{Size}$, h, and the threshold factor $Thresh_{Factor}$ for cell/background separation. ST-Diff-TCV performance exhibits moderate sensitivity to the parameter values. In this work we performed exhaustive grid search in the parameter space to identify the optimal settings. Table 4.4 lists the parameter values that we determined experimentally. Alternate parameter optimization techniques may be required to achieve more accurate segmentation in sequences with significantly different quality levels and cell types. In summary, our experiments suggest that the joint ST-Diff-TCV method improves the segmentation accuracy compared to CV, TCV, and ST-Diff, especially when applied to simulated and real microscopy images with cells characterized by wide intensity variations and undergoing mitotic events, changes in density, and low SNR (Table 4.3 and Figure 4.8).

Table 4.4: Different parameters used for the joint ST-Diff-TCV method

Dataset name	μ	λ_t	TS_{Ratio}	$Parzen_{Size}$	h	κ	$Thresh_{Factor}$
N2DH-SIM01	0.1	0.1	1000	3	2	4	1
N2DH-SIM02	0.1	0.1	1000	3	1	4	1
N2DH-SIM03	0.1	0.1	20	3	5	4	1
N2DH-SIM04	0.1	0.1	200	3	10	4	1
N2DH-SIM05	0.001	0.1	900	3	9	4	1
N2DH-SIM06	0.001	0.1	1200	3	2	4	1
C2DL-MSC01	0.01	0.1	610	3	8	4	1
C2DL-MSC02	0.001	0.1	1	3	6	4	0.5
N2DL-HeLa01	0.1	0.1	20	3	6	4	1
N2DL-HeLa02	0.001	0.1	1	3	5	4	1
N2DH-GOWT101	0.001	0.1	10	3	5	4	0.5
N2DH-GOWT102	0.01	0.1	11	3	5	4	0.75

Chapter V: CELL TRACKING

The automation of tracking is a complex problem, and the cell correspondence complexity increases exponentially with the increase of cell population. One reason for this is that the biological cells may follow a Brownian movement, which makes the motion estimation very hard. This chapter describes a method for automated tracking of biological cells in time-lapse microscopy by motion prediction and minimization of a global probabilistic function for each set of cell tracks. We identify cell events by backtracking the cell track stack and forming new tracks to determine a partition of the complete track set.

This chapter is organized in six sections. The first section introduces an overview and the main components of the tracking method. In the second section, we address the cell separation problem in case of images with high density and cell cluster detection. In the third section, we present the cell feature computation. In the fourth section, we highlight the motion estimation methods, give an overview of optical flow methods, and describe a joint local-global optical flow technique that we applied to our data. In the next section we introduce our likelihood-based bi-frame cell matching technique to link cells between frames. In the last section, we describe the proposed algorithms to create cell tracks and the acyclic graph.

5.1 Method Overview

The goal of cell tracking is to identify all cells throughout the time-lapse sequence in order to follow their motion and detect the main events such migration, mitosis, apoptosis, entering and leaving the field of view. Our method belongs to the category of tracking by detection . Therefore it uses cell indicator functions that were determined in each frame to perform cell tracking and quantification. In Figure 5.1, we display the main stages of the proposed system. These are

1. *Pre-tracking*

2. *Feature Vector Computation*

3. *Motion Model Estimation*

4. *Cell Matching*

5. *Cell Track Construction and Handling of Cell Events*

6. *Cell Quantification.*

A tracking algorithm ideally should have the capability to address the main cell events that occur in a sequence. These events are

- *Cell Mitosis: division of a cell into two daughters*
- *Cell Disappearance: cell leaving field of view or collision*
- *Cell Apoptosis/Necrosis: death of a cell*
- *New Entering Cells: cell entering the field of view*
- *Cell Reappearance: cell re-entering the field of view*

Figure 5.2 depicts a model of the cell events of appearance, disappearance, mitosis, and collision. Furthermore, Figure 5.3 displays a pair frames with all detectable events. Cell event detection usually follows cell tracking and requires analysis and linking or division of cell tracks.

The association problem is usually the most complex and most challenging stage of the tracking system. By increasing the number of cells, the complexity of the linking problem increases exponentially. Changes in cell shape such as cell stretching may also cause false appearances due to cell detection discontinuities. In Figure 5.4, we show in orange color

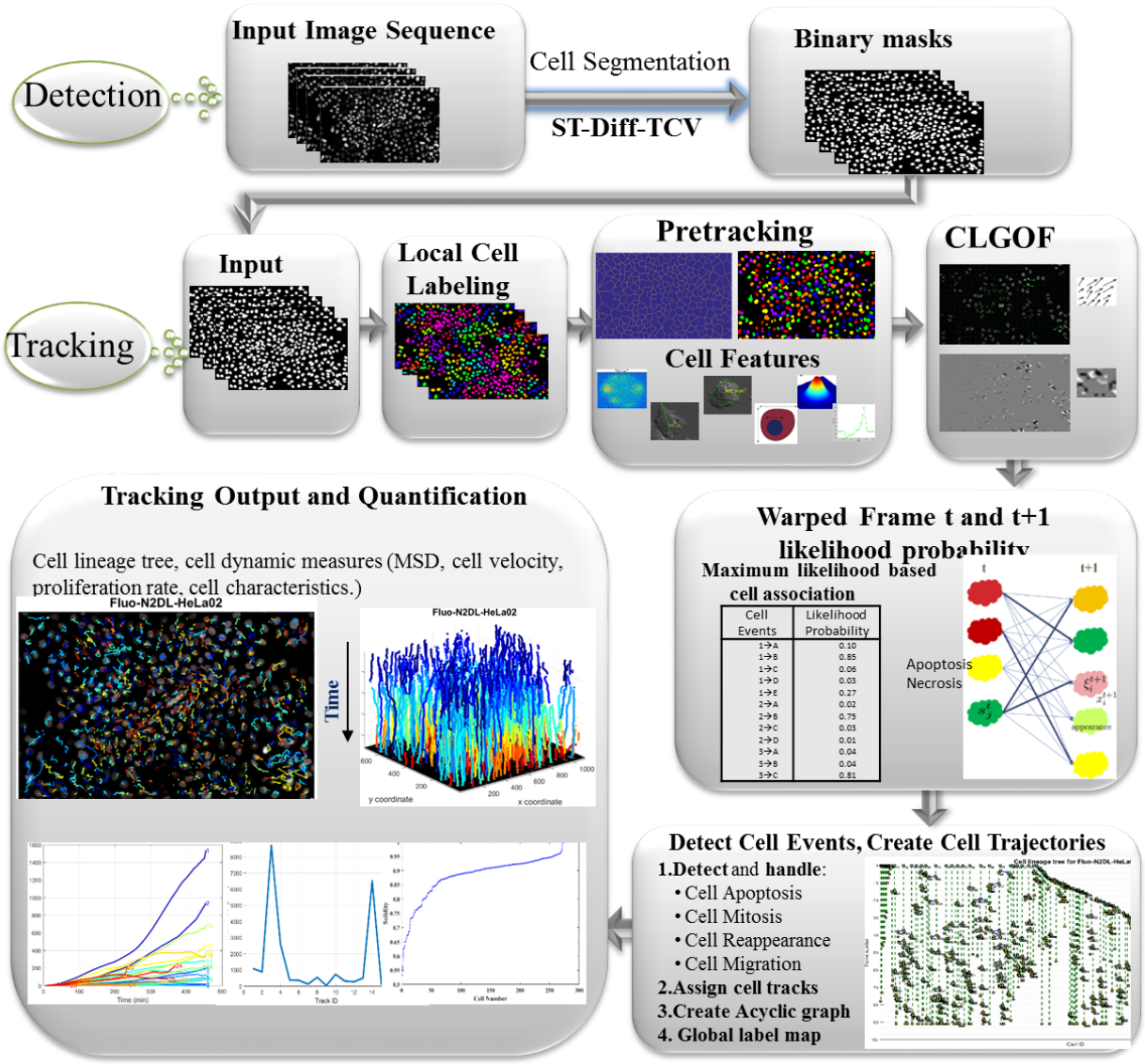

Figure 5.1: Pipeline of the proposed tracking algorithm.

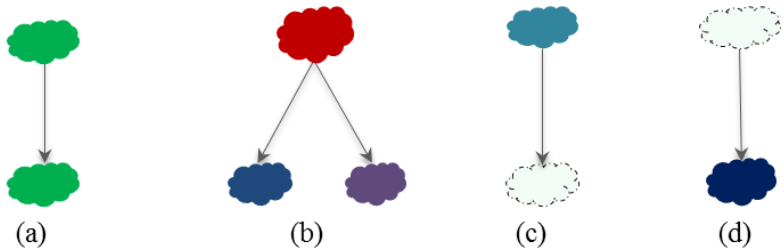

Figure 5.2: Association cases considered in our tracking system (a) migration, (b) mitosis, (c) disappearance, or apoptosis, or leaving field of view, and (d) appearance, or cells entering the field of view.

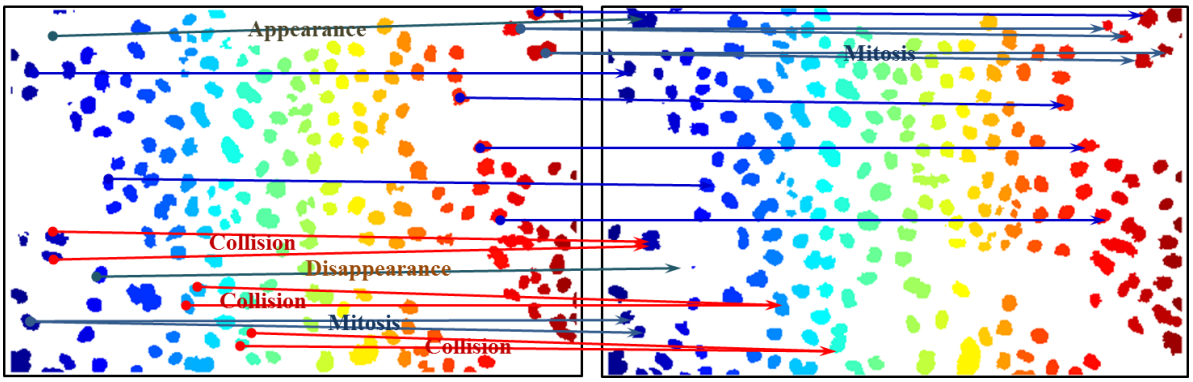

Figure 5.3: Different events present on sample frame of Hela2 dataset

two false positives for cell reappearance caused by over-segmentation of a single cell. These artifacts may reduce tracking accuracy.

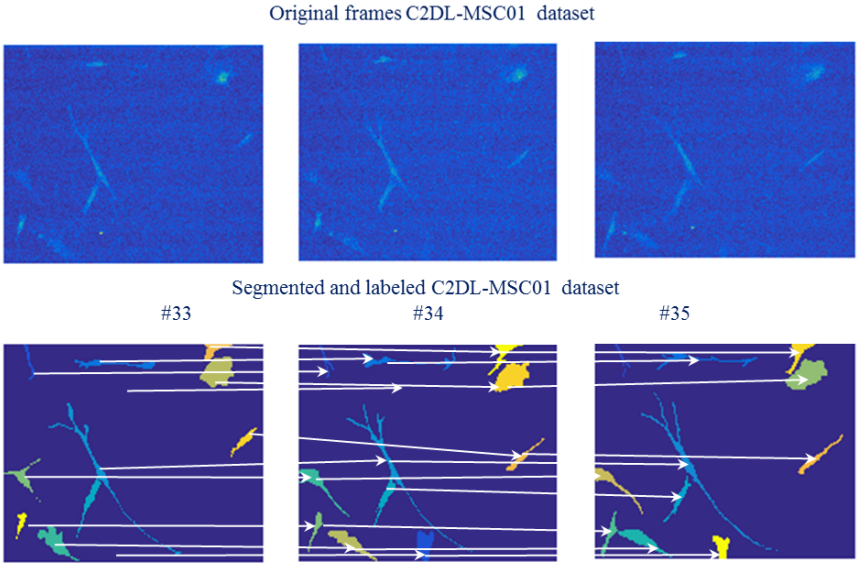

Figure 5.4: Association problem with shape changes on three consecutive frames of C2DL-MSC01 dataset. The red arrow show a cell entering the field of view while the orange arrows show false disappearance (processed as an Apoptosis event)

Furthermore, we display a flowchart of the proposed tracking system in Figure 5.5. We first apply cell fusion separation and over-segmentation reduction in the pre-tracking stage. Then we estimate the cell motion use of a variational multi-scale optical flow technique. We then apply the motion field to calculate a new frame and we apply max likelihood decision

on a probabilistic function of overlap to find cell correspondences. We then construct cell linked lists to represent cell tracks and we backtrace the lists to detect overlapping tracks and divide overlapping. Overall, the tracking and cell detection problem can be viewed as a partitioning problem by cost minimization.

The tracking system produces the following data and information: globally linked cell indicator maps, the cell lineage tree, and the tracking output measurements about the birth and death information, the mitosis events and cell velocities.

5.2 Pre-tracking

5.2.1 Small Region Removal

To distinguish between cell and non-cell regions in the segmented image we consider a threshold value defined with respect to minimum cell area for an object to be considered as a cell or part of the background. This removes all the non-cell detected objects before tracking to reduce false positives.

5.2.2 Cell Influence Zones

A cell influence zone is a topology of points that are connected to only one cell region by a specific relation [93]. Often times this relation originates from a measure of distance between a region and a point, such as the distance function [62].

Having defined an influence zone at this stage we perform skeletonization by influence zones denoted by $SKIZ$. This yields sets of points that belong to no influence zone therefore they determine the boundaries by cell influence zones. The zones within the boundaries can be used to define cell adjacencies and can be used later to estimate Parzen density estimates for finding cell correspondences between successive frames. More specifically the zone determines an area in space called gate, which is used to limit the area for prediction in our data association stage. If a candidate cell of a neighboring time frame lies within the gate of the current frame then we can consider it as a candidate for a matching association.

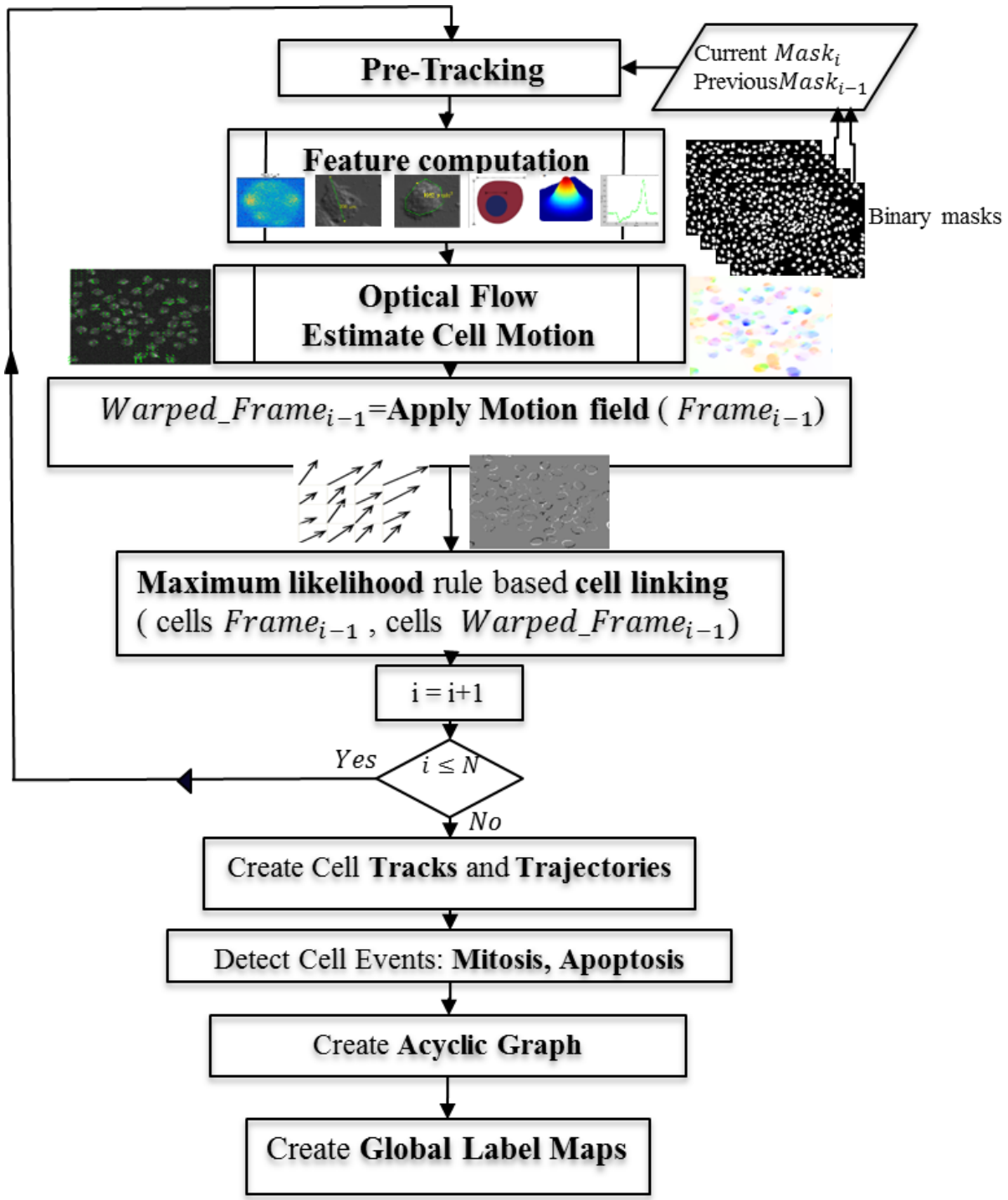

Figure 5.5: Flowchart of our tracking system.

To perform SKIZ, we first calculate the distance transform of the image. Distance Transform assigns each pixel with the distance to the nearest image feature point [78] like edges or object boundaries. The skeleton then lies along the curvature discontinuities or creases in the distance transform, which correspond to the local maxima on the distance transform [102]. The $SKIZ$ set can be computed using the watershed transform.

5.2.3 Separation of Cell Clusters

In case of dense datasets, the cells can be so close that they can be falsely detected as clusters of cells and segmented as a single foreground object as shown in Figure 5.6. Thus, it is important to split clusters of multiple cells that were segmented as a single cell using some geometrical shape priors, shape statistics, distance transform watershed operation and H-transform [95].

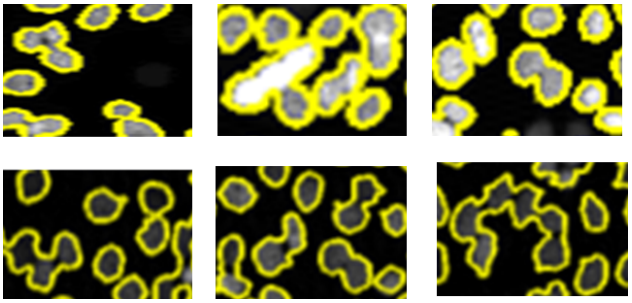

Figure 5.6: Examples of clusters of cells detected as the same foreground object by our segmentation.

To distinguish between colliding cells we apply watershed segmentation to the Euclidean distance map computed on the cell segmentation map. This operation creates a boundary between the different cells in the cluster. The watershed transform has been proposed by many authors for nuclei segmentation [122, 34]. However, the number of peaks in the distance map may result in over segmentation by splitting the clusters of cells into more regions than necessary. Figure 5.8, middle column, illustrates the over-segmentation effect produced by the detection of extraneous minima. The next step is to reduce the number of over-segmented

cell fragments by a morphological reconstruction technique call the H-minima transform.

H-minima Transform

H-minima Transform [111, 95] is a morphological operation obtained by erosion of the image I increased by a height h defined by

$$H(I, h) = R^{\epsilon}(I + h) \tag{5.1}$$

where R^{ϵ} is defined as the reconstruction by erosion morphological operator and h is a depth parameter. H-minima transform removes spurious local minima and avoids oversegmentation by supressing all the regional minima whose depth is smaller than h. H-minima/maxima transform has been largely used in nuclei detection in biomedical images [96, 115, 59].

To detect the presence of cell clusters that were undersegmented into a single cell, we compute the solidity characteristic. We give the following definitions for the solidity measure and the convex point set that is used in solidity computation.

Definition 5.2.1 (Convex point set)**.** A set of points is defined to be convex if it contains the line segments connecting each pair of its points. The convex hull of a given set X is defined as the smallest convex region that contains X. It is also referred to as a convex envelope surrounding the shape.

Definition 5.2.2 (Solidity)**.** Clusters of cells have contours with points of high concavity. Solidity is the measurement of the overall concavity of a cell. It is defined as the area of the shape region A_{shape}, divided by the convex hull area A_{conv}. Returns a scalar specifying the proportion of the pixels in the convex hull that are also in the region. Prior information about a unique cell or cluster of cells has to be used as a threshold for our estimation. The solidity of a convex shape is always 1. We show in Fig 5.6 some examples of clustered cells.

Computed as

$$S = \frac{A_{shape}}{A_{conv}}. \tag{5.2}$$

Therefore, the main steps of the cell separation approach approach are:

1. *Cell number estimation based on the solidity feature of the cells*

2. *Distance transformation on original segmentation binary mask to obtain distance map*

3. *H-transformation to accurately locate the centroid of each cell in the cell cluster*

4. *Watershed segmentation to delineate the different cells in each cluster*

Regional minima are connected components (using 8-connected neighborhoods) of pixels with a constant intensity value, and whose external boundary pixels all have a higher value and h is a threshold value used for the H-minima transform.

As an example, we show in Figure 5.7 the distance transform, boundaries and watershed of the distance transform of frame 74 of Hela02 dataset.

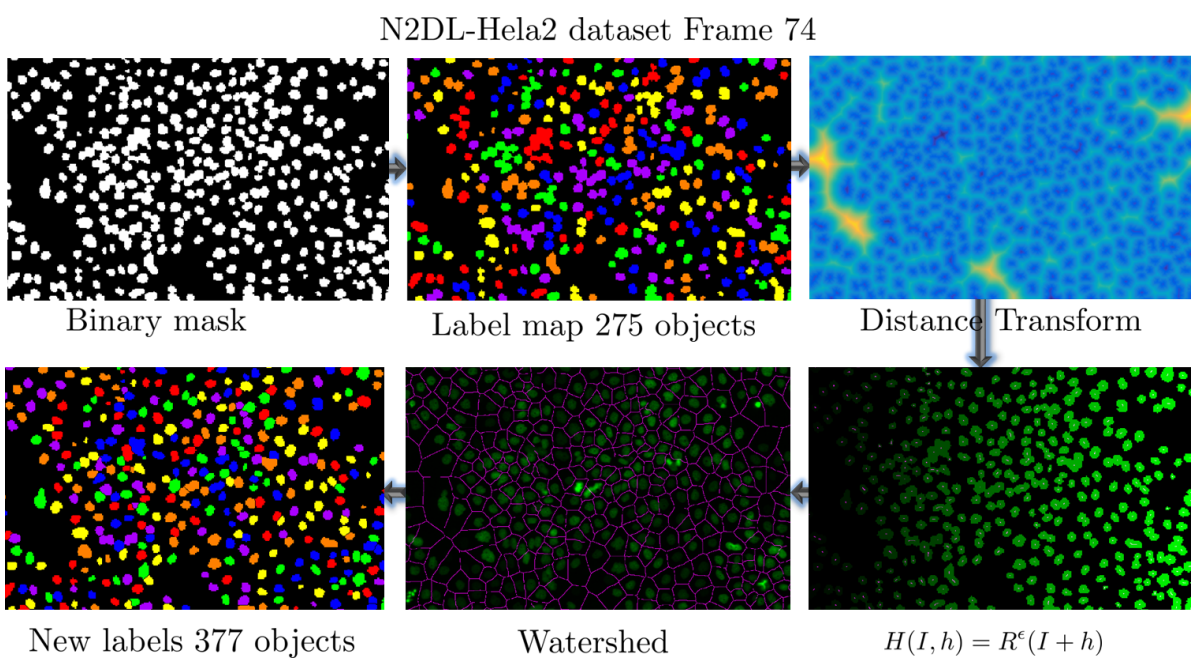

Figure 5.7: Example of cell cluster separation on frame 74 of N2Dl-Hela02 dataset.

In Figure 5.8 we show the watershed ridges for cell separation that separate the same object into different cells after an H-minima transform of the distance transform of the original binary mask, where we used a threshold to impose a number of minima. This

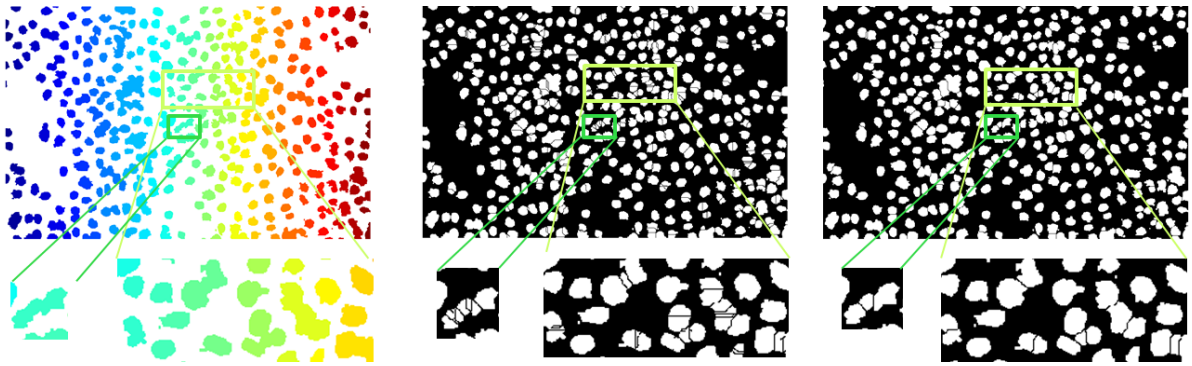

Figure 5.8: Labeled image frame of Hela02 dataset, cell separation showing oversegmentation and our final cell separation result after H-minima Transform and watershed segmentation.

threshold value is experimentally determined based on the number of cells detected in each cluster and by comparing this number to the number of estimated cell number using the solidity feature of the cells of the dataset. Solidity is area fraction of the region as compared to its convex hull. So solidity is what fraction of the actual area your region is. We display an example of the contours of adjacent cells before and after cell separation in Figure 5.9.

5.3 Feature Computation

Compute cell properties to be used for finding cell correspondences. After the pre-tracking stage, we compute intensity, size, and shape characteristics for each cell. Let for each cell A, $c_A \in \mathbb{R}^2$ be the centroid of the cell, $s_A \in \mathbb{R}$ be the number of voxels occupied by the cell. We compose a pattern vector that corresponds to each cell that may also be called observation.

A usual approach to finding cell correspondences would be to compute distances between the pattern vectors and use a nearest neighbor algorithm to find the closest pairs of vectors. But our experiments showed that a cell could have several close matches, only one of which

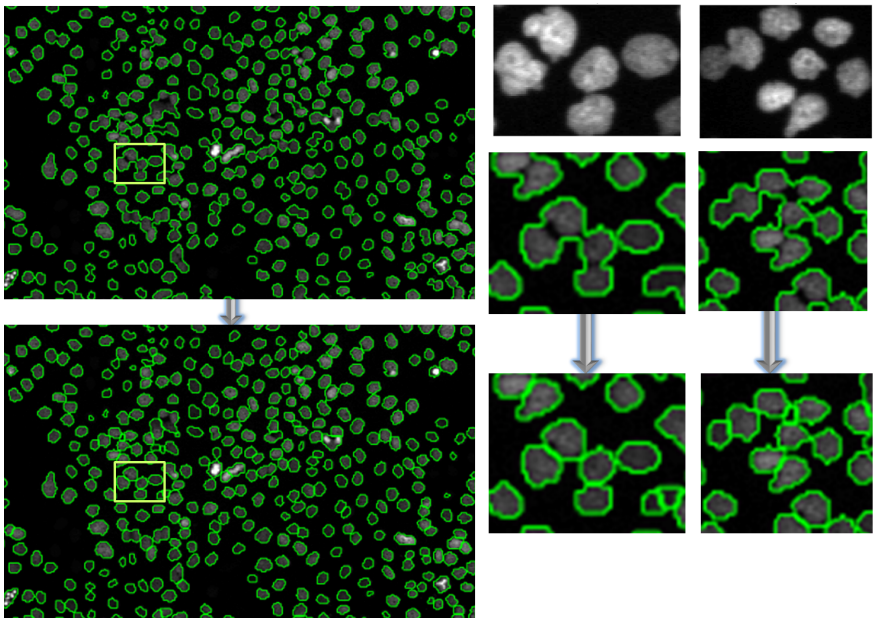

Figure 5.9: Contours delineating the cell boundaries of cell clusters on frame 74 of N2Dl-Hela02 dataset.

is correct. Based on this observation we suggest using optical flow to estimate the motion pattern of each cell to be used for matching. This strategy resulted in a very good association independent probability estimate of the cell matching and association problem.

5.4 Estimating Cell Motion

5.4.1 Optical Flow Computation

The optical flow estimates the velocity of each pixel between two consecutive frames at times t and $t + \Delta t$ based on spatio-temporal image intensity variations. This method is used in computer vision to characterize and quantify the motion of objects. Many algorithms have been proposed and used to solve or optimize the optical flow methods [71, 57, 6, 17, 19, 18, 114, 123, 70].

Methods for optical flow estimation are based on the computation of partial derivatives of the image intensities signal. The two most popular methods are Lucas and Kanade [71] and Horn and Schunk [57]. Lucas and Kanade proposed a local method that uses a

spatial constancy assumption. The method by Horn and Schunk is a global method that supplements the optical flow constraint with a regularizing smoothness term.

Differential optical flow methods assume that the intensity value I at each pixel $\vec{\omega} = (x, y)$ at time t is not affected by its displacement $\vec{\delta} = (dx, dy)$ at $t + 1$.

$$I\left(\vec{\omega} + \vec{\delta}, t + 1\right) = I\left(\vec{\omega}, t\right). \tag{5.3}$$

If we approximate $I\left(\vec{\omega} + \vec{\delta}, t + 1\right)$ by first order Taylor expansion we have that:

$$I\left(\vec{\omega} + \vec{\delta}, t + 1\right) = I\left(\vec{\omega}, t\right) + \vec{\nabla} I \cdot \vec{d} + \mathcal{O}(\partial^2) \tag{5.4}$$

$$I\left(x + dx, y + dy, t + 1\right) = I\left(x, y, t\right) + \frac{\partial I}{\partial x} dx + \frac{\partial I}{\partial y} dy + \frac{\partial I}{\partial t} dt \tag{5.5}$$

Because of intensity constancy assumption in 5.3, it follows that:

$$\frac{\partial I}{\partial x} dx + \frac{\partial I}{\partial y} dy + \frac{\partial I}{\partial t} dt = 0 \Rightarrow \tag{5.6}$$

$$-I_t = I_x \frac{dx}{dt} + I_y \frac{dy}{dt} \tag{5.7}$$

$$-I_t = \vec{\nabla} I \cdot \frac{d\vec{\delta}}{dt} \tag{5.8}$$

$$-I_t = \vec{\nabla} I \cdot \vec{\alpha}, \tag{5.9}$$

where $\vec{\alpha} = \frac{d\vec{\delta}}{dt} = (u, v)$.

However we cannot find a unique solution (u, v) using this equation only; therefore we have to deal with the aperture problem. This limits us to calculating only the optical flow that is normal to the edge direction.

In the computation of optical flow we usually make implicit or explicit assumptions that set constraint conditions to our problem. We assume gradual changes of image motion of an object. That is, the image motion slowly changes in time (Figure 5.10). In practice,

this means the temporal increments are fast enough compared to the motion of objects in a frame. In this case, the temporal difference approximates the derivative of the intensity with respect to time. An additional constraint is that of spatial smoothness that requires neighboring pixels to have approximately the same motion. Finally, we may assume that the gradient of the image intensities is not changed by the displacement. This is known as the gradient constancy assumption.

$$\nabla I\left(x, y, t\right) = \nabla I\left(x + dx, y + dy, t + 1\right) \tag{5.10}$$

Local estimation technique

To overcome the aperture problem, Lucas and Kanade assumed that the optical flow is constant within a neighborhood ρ. They proposed to use a least square fitting method to minimize the following function and estimate the optical flow components [71, 19]:

$$E_{LK}(u, v) = K_\rho \star \left[\left(I_x u + I_y v + I_t\right)^2\right]. \tag{5.11}$$

By setting partial derivatives extremum conditions $\frac{\partial E_{LK}}{\partial u} = 0, \frac{\partial E_{LK}}{\partial v} = 0$, we get the following linear system of equations

$$E_{LK} = \begin{bmatrix} K_\rho \star \left(I_x^2\right) & K_\rho \star \left(I_x I_y\right) \\ K_\rho \star \left(I_x I_y\right) & K_\rho \star \left(I_y^2\right) \end{bmatrix} \begin{bmatrix} u \\ v \end{bmatrix} = \begin{bmatrix} -K_\rho \star \left(I_x I_t\right) \\ -K_\rho \star \left(I_y I_t\right) \end{bmatrix} \tag{5.12}$$

Because we cannot find solutions at all points, the resulting field is non-dense. Therefore an interpolation step is used to alleviate this shortcoming.

Global estimation technique

Another group of approaches estimates dense flow by minimizing a global functional with regularization constraints. Horn and Schunk proposed to find the field $\vec{\alpha}$ as the minimizer

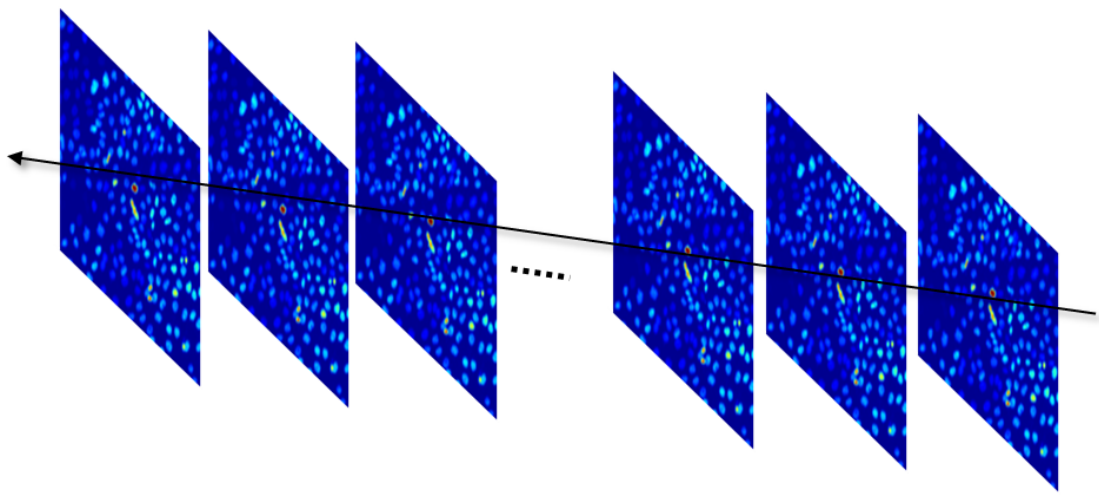

Figure 5.10: Assumption behind Lucas and Kanade optical flow: Motion is slow relative to the frame rate.

of the following functional:

$$E_{HS} = \int_{\Omega} \left[(I_x u + I_y v + I_t)^2 + \lambda \left(|\nabla u|^2 + |\nabla v|^2 \right) \right] dxdy, \tag{5.13}$$

where λ is a Langrangian multiplier for imposing smoothness constraints to the optical flow field. To solve the above convex functional we need to solve the Euler-Lagrange equations with reflecting boundary conditions:

$$0 = \Delta u - (1/\lambda) \left(I_x^2 u + I_x I_y v + I_x I_t \right) \tag{5.14}$$

$$0 = \Delta v - (1/\lambda) \left(I_x I_y u + I_y^2 v + I_y I_t \right), \tag{5.15}$$

where Δ is the Laplace operator:

$$\Delta = \partial_{xx} + \partial_{yy}. \tag{5.16}$$

This solution of these diffusion-reaction equations is unique. Moreover, at locations where $|\nabla I| \approx 0$, the local flow cannot be computed but the regularization term provides an estimate based on neighboring pixels. Therefore this technique yields a flow estimate for the complete image domain and no interpolation is needed. However global differential methods may be more sensitive to noise than the local techniques. Flow fields are less regularized at noisy image regions because noisy regions are characterized by high gradients that overcome the smoothness regularization term.

5.4.2 Combined Local/Global Optical Flow Method (CLGOF)

In Lucas-Kanade [71] and Horn-Schunck [57] optical flow techniques, the vector field extracted may not be dense, may have many discontinuities [71, 17] or may not be robust [57, 17]. Here we adopt a solution that combines the local and global optical flow estimation principles [17, 19].

Energy Functional

The functional includes data and smoothness terms. The data term measures the deviations from the intensity constancy assumption and the gradient constancy assumption and is given by:

$$E_{Data}(u,v) = \int_{\Omega} \left(\left| I(\vec{\omega} + \vec{\delta}) - I(\vec{\omega}) \right|^2 + \gamma \left| \nabla I(\vec{\omega} + \vec{\delta}) - \nabla I(\vec{\omega}) \right|^2 \right) d\vec{\omega} \tag{5.17}$$

A function $\Psi(s^2)$ may be applied to the integrand to moderate the effect of outliers:

$$E_{Data}(u,v) = \int_{\Omega} \Psi \left(\left| I(\vec{\omega} + \vec{\delta}) - I(\vec{\omega}) \right|^2 + \gamma \left| \nabla I(\vec{\omega} + \vec{\delta}) - \nabla I(\vec{\omega}) \right|^2 \right) d\vec{\omega}. \tag{5.18}$$

The smoothness term is:

$$E_{Smooth}(u,v) = \int_{\Omega} \Psi\left(|\nabla_{ST} u|^2 + \nabla_{ST} v|^2\right) d\vec{\omega}, \tag{5.19}$$

where $\nabla_{ST} = (\partial_x, \partial_y, \partial_t)^T$.

The energy functional is given by:

$$E_{CLG} = E_{Data} + \lambda E_{Smooth}. \tag{5.20}$$

Minimization

Based on the calculus of variations, the minimizer of 5.20 is a solution of the Euler-Lagrange equations:

$$\begin{aligned}
&\Psi'(I_x^2 + \gamma(I_{xz}^2 + I_{yz}^2)) \cdot (I_x I_z + \gamma(I_{xx} I_{xz} + I_{xy} I_{yz})) \\
&\quad - \alpha \nabla \cdot (\Psi'\left(|\nabla_{ST} u|^2 + \nabla_{ST} v|^2\right) \nabla_{ST} v) = 0 \\
&\Psi'(I_z^2 + \gamma(I_{xz}^2 + I_{yz}^2)) \cdot (I_y I_z + \gamma(I_{yy} I_{yz} + I_{xy} I_{xz})) \\
&\quad - \alpha \nabla \cdot (\Psi'\left(|\nabla_{ST} u|^2 + \nabla_{ST} v|^2\right) \nabla_{ST} v) = 0.
\end{aligned} \tag{5.21}$$

In the system of 5.21 we use reflecting boundary conditions.

Coarse to Fine Strategy

In order to approximate the solution for the displacement field we numerically solve the system in 5.21 at two scales; a coarse grid and the original grid. A multi-scale approach yields a more accurate global solution than a single-scale approach. This technique includes fixed point iterations in conjunction with a downsampling strategy. The final solution found at the coarse scale is used to initialize the finer scale.

This technique yields an approximation of the displacement field $\hat{\delta}$:

$$\hat{\delta} = arg \min_{\vec{\delta}} E_{CLG}. \tag{5.22}$$

An example of the optical flow estimate using this method is displayed in Figure 5.11.

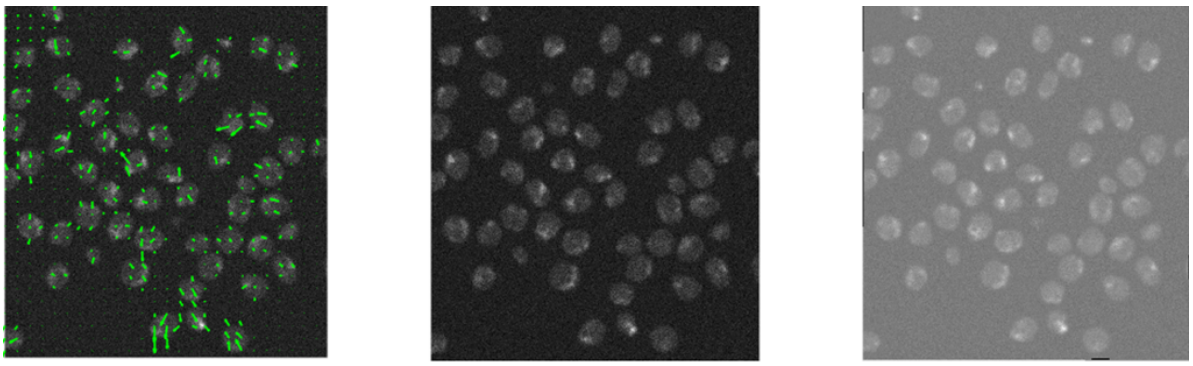

Figure 5.11: Optical flow estimate (left) between frames 42 and 41(middle) and the warped frame 41 (right) of SIM04 dataset.

5.4.3 Applying Motion Field to Previous Cell Indicator Frame

The estimated displacement field $\hat{\delta}$ is used to calculate a warped frame $\hat{I}$ by:

$$\hat{I}(\vec{\omega} + \hat{\delta}, t+1) = I(\vec{\omega}, t). \tag{5.23}$$

We define a cell indicator function $L : \Omega \rightarrow \mathbb{Z}$ that maps pixel values onto unique cell identifiers produced by the cell segmentation stage. We apply warping to the cell indicator frame to find $\hat{L}$ before linking the current and previous frame:

$$\hat{L}(\vec{\omega} + \hat{\delta}, t+1) = L(\vec{\omega}, t). \tag{5.24}$$

The cell matching and linking stage is applied between the pairs of frames $\{I(\vec{\omega}, t+1), \hat{I}(\vec{\omega}, t+1)\}$ and $\{L(\vec{\omega}, t+1), \hat{L}(\vec{\omega}, t+1)\}$ using probabilistic decision functions. An example of the

optical flow calculation and application for warping during cell division is displayed in Figure 5.12.

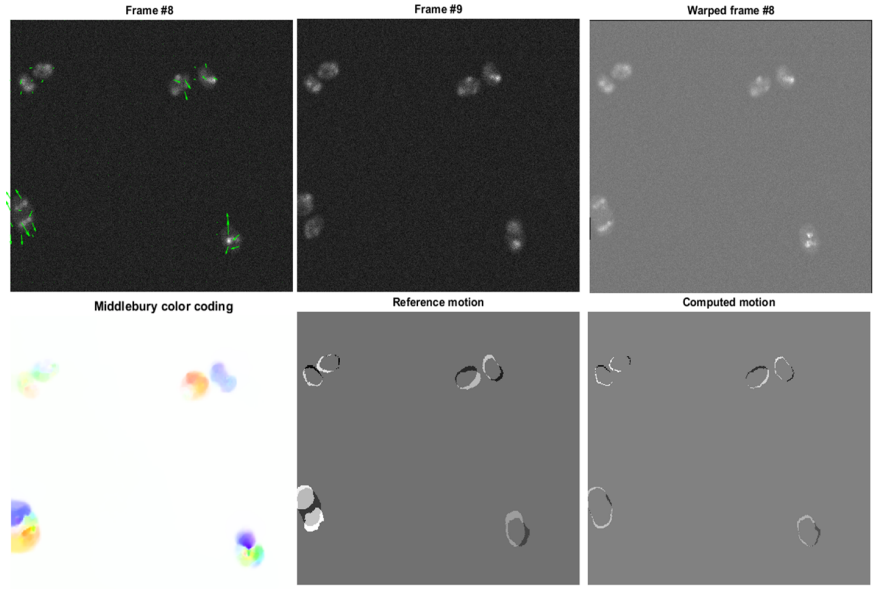

Figure 5.12: First row: optical flow estimate (left) between frames 9 (middle) and the frame 8 (right) of SIM05 dataset. Second row: middlebury color coding of computed optical flow (left), difference between cell indicator functions between reference cell masks of frames 8 and 9 middle), difference between cell masks of frame 9 and warped frame 8 using computed optical flow (right).

5.5 Likelihood-based Bi-frame Cell Matching - Linking Cells Between Current and Previous Frames

The problem of finding the association with the highest probability is performed by computing the max-likelihood matching for each cell of the current frame among all the cells of the previous warped frame.

We formulate bi-frame cell matching as a classification problem.

Let $\Xi_t = \{\xi_1^t, \xi_2^t, \ldots, \xi_n^t\}$ be the states of a system with n cells at time t, $X_t = \{x_1^t, x_2^t, \ldots, x_n^t\}$ be the set of observations for all cells at time t, and $S_t = \{s_1^t, s_2^t, \ldots, s_n^t\}$ be the set of samples for all cells at time t.

We also assume a Markov process that transition probability depends only on the state of the mother cell or the same cell in previous frame $P(S_{t+1}|S_t)$.

We compute the likelihood that the cell i in frame $t+1$ is connected with cell j in frame t. Assuming that each cell i in frame t corresponds to a state of nature s_i^t, we calculate:

$$\pi_{ij}^{t+1} = p(x_i^{t+1}|\xi_i^{t+1} = s_j^t). \tag{5.25}$$

Here we define a likelihood function π_{ij}^t based on the observations derived from the computed cell features. We currently use spatial proximity between cells of warped previous indicator function $\hat{L}(\omega + \hat{\delta}, t+1)$ and cells of the current indicator function $L(\omega, t)$ to form the observation vectors. Hence

$$p(x_i^{t+1}|\xi_i^{t+1} = s_j^t) \propto \exp\left\{-(1/2)(x_i^{t+1} - x_j^t)^T \Sigma^{-1}(x_i^{t+1} - x_j^t)\right\}. \tag{5.26}$$

We make a decision using a maximum-a-posteriori (MAP) rule that becomes a maximum likelihood (ML) rule assuming equal priors. We also use a reject option to model cell re-appearance when the maximum likelihood is still very low. Figure 5.13 displays the cell matching procedure.

$$\hat{j} = arg \max_j \pi_{ij}^{t+1}. \tag{5.27}$$

After making a decision we assign the predicted cell class $\hat{j}$ to the cell indicator map $L(\vec{\omega}, t+1)$.

5.6 Creating Cell Tracks and Acyclic Graph

Definition 5.6.1 (Individual cell track)**.** Each track $\phi_i \in \Phi^M$ is the set of identified cell states in the sequence.

$$\phi_i = \{\xi_i^t \,|\, t = t_{start}, \ldots, t_{end}\}, \tag{5.28}$$

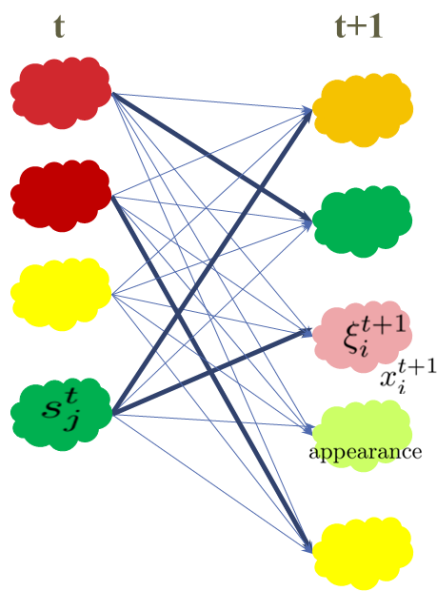

Figure 5.13: Example of possible cell associations and maximum likelihood matches in bold. The reject option yields the newly appearing cell that has no match with previous frame.

where t_{start} and t_{end} denote the first and last frame of the track in the sequence with $0 \leq t_{start} \leq t_{end} \leq N-1$.

Definition 5.6.2 (Cell track set)**.** Let N be the number of frames in a time-lapse sequence, M the total number of cell tracks. and $L_G = \{\xi_i^t\}$ the set of cell labels among all frames. Let Φ^M, be the set of all cell tracks in a sequence with $|\Phi^M| = M$.

Cell tracking optimization problem

Our goal is to identify all cell tracks Φ^M in the sequence. This can be formulated as follows: Let $\mathcal{C}\{\Phi^M\}$ be the cost computed over a specific track set Φ^M.

Find cell track set

$$\hat{\Phi}^M = \arg\min_{\Phi^M} \mathcal{C}\{\Phi^M\}, \tag{5.29}$$

with the conditions

$$\Phi^M = \bigcup_{i=1\ldots M} \phi_i \tag{5.30}$$

$$\phi_j \cap \phi_k = \emptyset, \forall j \neq k. \tag{5.31}$$

After finding a solution $\hat{\Phi}^M$, we assign a track label $l \in L_G$ to each cell. The track duration is defined from the discrete time point of cell appearance till its disappearance, division, or reaching the end of sequence. If a cell reappears, then we create a new track. In the case of cell division we end the track of the mother cell and create two new daughter tracks.

5.6.1 Creating Cell Tracks

We create linked lists of the cell states that represent the tracks. The elements of this list are quadruples $Q = \left[t, \xi_m^t, t_p, \xi_n^{t_p}\right]$, that contain the frame id, cell label (indicator) id, previous frame id and previous label id respectively. We create these lists by traversing the set of cell states in reverse chronological order. This procedure is outlined in Algorithm 7.

Algorithm 7 Identify cell tracks

Require:

```
for each linked list starting from last to first do
    for each cell in linked list do
        identify cell track stacks by finding parent cell labels that maximize likelihood of
        cell matching recursively using Cell_Linked_Lists
        Use stack to check if a tested cell has been added to a previous track
    end for
end for
return
```

The previous procedure produces cell linked lists that represent the tracks ϕ_i and adress cell appearance and disappearance. However, at the end of this stage some tracks may be partially overlapping that is in the case of cell division, where different cells have a common ancestor. We address these cases by finding the overlapping parts of two tracks ϕ_j and ϕ_k creating three new tracks, one for the ancestor $\phi_p = \phi_j \cap \phi_k$ and the 2 daughters $\phi_q = \phi_j - (\phi_j \cap \phi_k)$ and $\phi_r = \phi_k - (\phi_j \cap \phi_k)$. This procedure is outlined in Algorithm 8.

Algorithm 8 Identify cell events

Require:

```
for each track do
  while there exists a parent do
    check if [frame#, label#] is in a previous track and find matches
    if new match is found then
      division is detected, start a new track
      if cell is found in another track but not the already labeled then
        create a new track for division
      else if cell is only in previous tracks then
        close track and set parent label to 0
      end if
    else
      add cell to existing track
    end if
  end while
end for
return
```

5.6.2 Minimal Cost Cell Labeling

The individual maximum likelihood tracks ϕ_i constistute minimum error solutions according to Bayesian theory [45]. Therefore, the proposed algorithm can be considered as a forest of minimal cost chains with temporal constraints that minimizes the cost $\mathcal{C}$ in the universe of cell tracks Φ defined as:

$$\mathcal{C} = \sum_{\phi_i \in \Phi} C(\phi_i), \tag{5.32}$$

where $C(\phi_i)$ is the total cost of the cell track ϕ_i.

$$C(\phi_i) = \sum_{j \in \phi_i} c(\pi_{ij})], \tag{5.33}$$

where $c : \mathbb{R} \rightarrow \mathbb{R}$ is a decreasing function of sigmoid or exponential form. Our approach outlined in Algorithm 7 constitutes a greedy solution to this combinatorial optimization problem. The cell event analysis described in Algorithm 8 ensures that the solution set is non-overlapping and exhausts the universe of cell tracks for each sequence.

5.6.3 Representing Cell Tracks using an Acyclic Oriented Graph

Cell tracking results can be represented using an acyclic oriented graph. The nodes of such a graph correspond to the detected cells, whereas its edges coincide with temporal relations between them. The acyclic graph $G = (V, E)$ consists of a vertex set V and an edge set E such that $E \subset V \times V$. The condition for an ordered vertex pair to belong to the edge set E is:

$$\left(\xi_i^{t_1}, \xi_j^{t_2}\right) \in E \Leftrightarrow (i = j \wedge t_2 = t_1 + 1) \vee (i \neq j \wedge t_1 < t_2 \wedge P(\xi_i) = j)\,. \tag{5.34}$$

The function $P : \Xi \to \Xi$, where Ξ is the universe of cell states ξ_i, returns the ancestor ξ_a of an entity ξ_i that is $\xi_a = P(\xi_i)$. The first case of an edge in (5.34) represents cell migration, while the second case represents cell division. The graph is guaranteed to be acyclic because the edges are oriented and they follow the ascending temporal ordering of the cell state indicators within and between tracks.

We create acyclic graph table by traversing Processed_Cell_Trajectories to find last frame, first frame, and parent track id. Finally we create an adjacency list of the graph nodes and sort and relabel the nodes to create a tree representation. The last step is outlined in Algorithm 9.

Algorithm 9 Create adjacency list and write to file

Require:

```
for each row [track_id, first_frame, last_frame, parent_track_id] do
    Sort rows by first_frame
    Relabel track ids in increasing order starting from 1
    Write table to file
    Plot acyclic graph using tree visualization with node color coding
end for
return
```

We assign graph node labels $L_G(V)$ to cells in each indicator image and create global indicator function $F_L : \Omega \to L_G$ represented by a 2D+t label structure.

Chapter VI: CELL TRACKING EXPERIMENTS

In our work, cells are first detected in all the frames of the sequence independently from the tracking method. The tracking is done sequentially throughout the whole time-lapse sequence, and each cell of each frame is paired to none, one or two objects of the next frame. In this chapter we describe the cell tracking experiments including the validation against reference data for tracking and we discuss the results. In addition, we display and discuss the cell lineage trees, the detected cell trajectories, and cell quantification results. We track the cells by associating the segmented cell regions and making connections to accurately handle physiological cell events that take place during the course of the imaging experiment.

6.1 Construction of Reference Data for Tracking

The final ground truths (TRA-GT-F) were constructed by combining three pairs of manual annotations (TRA-GT) created by three experts from (CBIA-CZ, CIMA-ES, ERASMUS-NL) using a majority-voting scheme [25, 77]. The routines assume that each pair of manual annotations was corrected for automatically detected inconsistencies of two types: (1) a segmentation mask overlapping with multiple tracking markers or (2) a segmentation mask without a complete tracking marker.

The ground truth data for tracking include images with markers and a directed acyclic graph for each image sequence. The markers correspond to the tracked cells. The label of the marker denotes the track id or cell id. The directed acyclic graph represents the cell lineage tree. The nodes of the tree correspond to the identified cells, while the links represent either the track when a cell migrates, or the parent-daughter relationship in the case of cell division. The acyclic graph is stored in table form, where each row includes the cell track id, the start frame number, the end frame number, and the parent node id.

6.2 Tracking Evaluation Approach

The tracking accuracy measure symbolized by TRA aims to evaluate the capability of an automated algorithm to detect and track cells versus reference tracking data that were described above [77]. TRA calculates the difference between the acyclic oriented graph produced by the tested method and the TRA-GT-F reference graph. The idea behind the TRA measure is to calculate the least number of graph operations needed in order to transform the test graph produced by the tested method to TRA-GT-F. The allowed operations are node splitting/deletion/addition, edge deletion/addition, and editing of edge semantics.

The TRA measure is derived from the weighted sum of the above graph operations that is denoted by TRA_P. The manual weights are proportional to the effort of a human who performs these operations. This weighted sum is defined by:

$$TRA_P = w_{NS}NS + w_{FN}FN + w_{FP}FP + w_{ED}ED + w_{EA}EA + w_{EC}EC, \tag{6.1}$$

where w_{NS} , w_{FN} , w_{FP}, w_{ED}, w_{EA}, w_{EC}, are the weights for node splitting, node adding, node deletion, edge deletion, edge addition, and edge semantics editing.

The TRA measure is then given by

$$TRA = 1 - \frac{\min\left(TRA_P, TRA_E\right)}{TRA_E}, \tag{6.2}$$

where the TRA_E is the cost of constructing the reference graph from the beginning and is given by

$$TRA_E = w_{FN}|M| + w_{EA}|E|. \tag{6.3}$$

In this equation, $|M|$ denotes the cardinality of the node set, and $|E|$ denotes the cardinality of the link set of TRA-GT-F. The division operation in (6.2) normalizes the graph cost, and the subtraction from 1 defines an evaluation function that increases with better tracking,

such that $TRA \in [0, 1]$.

6.3 Automated Cell Tracking Results

The objective of cell tracking is to identify and follow the segmented cells in a time-lapse sequence. We performed cell tracking experiments and validated them against reference tracking results using the TRA measure. We then computed and visualized the cell lineage trees produced by the automated tracking algorithm. We finally computed morphology, diffusivity, velocity, and motility measures. In the following paragraphs we report results of our experiments.

We illustrate in Figures 6.2 - 6.5, the cell lineage trees automatically generated by our tracking approach using the reference cell identifier maps (segmentation maps). Furthermore, Figures 6.6 - 6.9 display the cell lineage trees produced by our fully automated cell segmentation and tracking methodology. These trees correspond to the directed acyclic graph and represent and visualize the tracked cells and the cell events detected by our tracking methodology. Our automatically constructed trees $T_{test}(M_{test}, E_{test})$ consist of nodes M_{test} that represent the cells that are identified across the sequence, and links E_{test} that represent the cell event evolution, namely cell migration, cell appearance and disappearance, and cell mitosis. More specifically, the dashed links denote cell migration and the continuous links denote a parent-daughter relationship.

The TRA tracking accuracy measure that was mentioned earlier in (6.2), computes the similarity between lineage trees identified by our methodology versus reference lineage trees that were constructed manually by human operators. Table 6.1 lists the tracking accuracy measure using as input the manual cell segmentation masks. In Table 6.1, we observe that the tracking method produces very high accuracy rates with an average of 0.992. These results show that our tracking approach is able to detect cell events very efficiently given a reference segmentation.

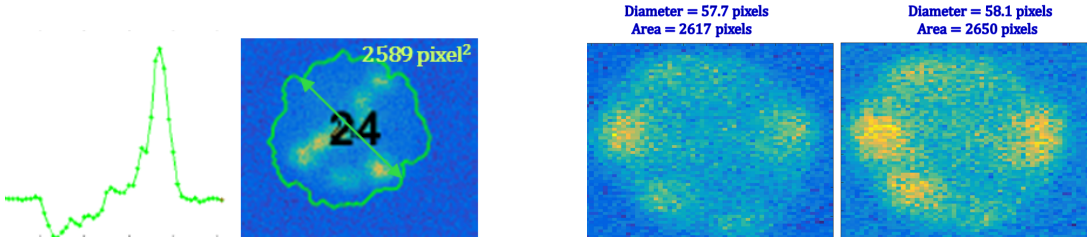

(a) Example of features of a cell labeled 24 of N2DH-SIM01 dataset.

(b) Features of cells of N2DH-SIM01 dataset.

Figure 6.1: Examples of feature computation.

Microscopy live cell image sequences may present large time and space distances that might reduce the tracking accuracy. Computing the displacement field between each two pairs of frames using the Combined Local Global Optical Flow and Coarse to Fine Strategy before our bi-frame matching will enable us to successfully overcome the problem of large time and space discrepancies for a robust and efficient cell tracking algorithm.

In addition, Table 6.2 contains the tracking validation after using ST-Diff-TCV segmentation results as input to our tracking approach, thus testing a fully automated segmentation, tracking, and quantification system. The tracking accuracy values reported in Table 6.2 are very promising. We note that the segmentation stage allows for efficient tracking detection. Overall, our method produces very promising tracking rates with an average tracking rate of 0.891. In specific cases, over- or under- segmentation of a cell may significantly reduce the tracking accuracy. The lower TRA value for the C2DL-MSC02 sequence is caused by the very low CNR and SNR characteristics of this sequence and very elongated cell morphology with high intensity variability inside the cell body. These effects result in over-segmentation, which creates false positives in cell detection and tracking. Hence, this result indicates that tracking is very dependent on segmentation. Besides this, in theory, under-segmentation produces false negatives in cell detection that are propagated to tracking.

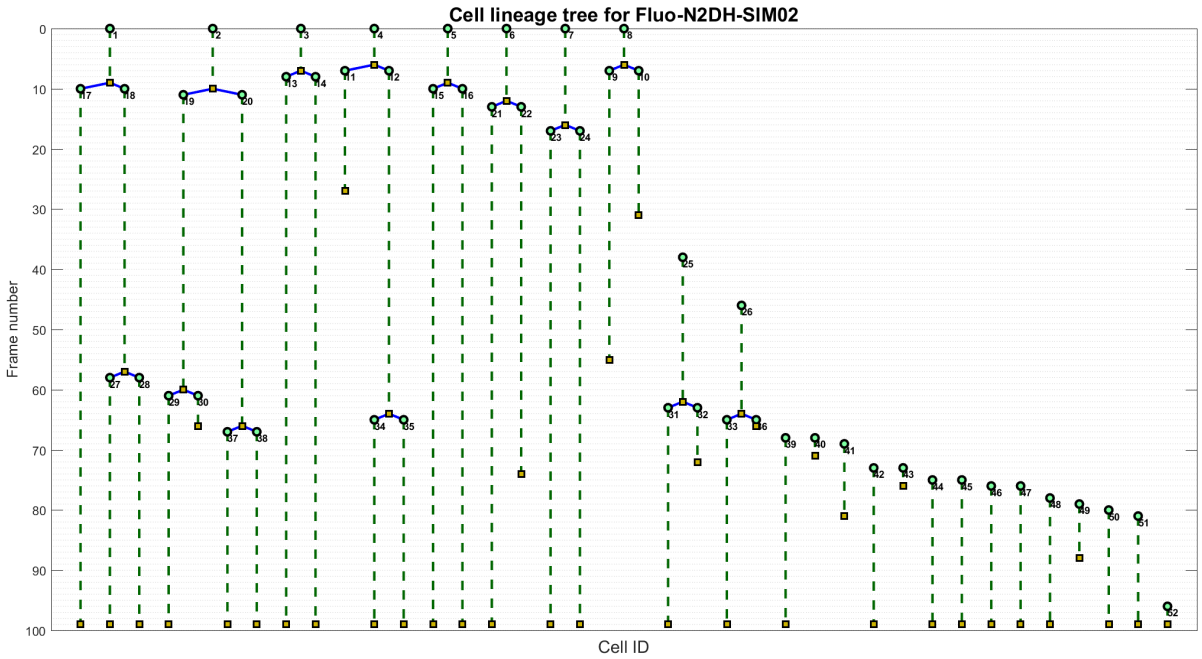

Figure 6.2: Cell lineage tree generated by our method on N2DH-SIM02 dataset. Tree nodes represent the cell track ids of each cell.

Visualization of Cell Trajectories

As an application of cell tracking, we generated cell trajectories in the 2D+t domain displayed in Figures 6.10a - 6.22a and in the 2D projected domain displayed in Figures 6.10b - 6.22b. The system produces automatically the cell trajectory graphs using the global cell indicator functions. In these figures the trajectories are color-coded and each color represents the biological events during the lifetime of a single cell. The track IDs are also displayed next to the end of each cell trajectory for reference. We note that in the simulated sequences we were able to visualize and monitor the events of cell migration, division, and new cell appearance with varying levels of density. Furthermore, the real datasets display the previously mentioned cell event types, and in addition we observe very high cell density with normal and abnormal cell divisions (Hela), and migration of elongated cells at low contrast (MSC). Therefore, the cell trajectories can effectively provide a visual analysis tool of a biological experiment. More specifically, they reveal mother and daughter relations, and

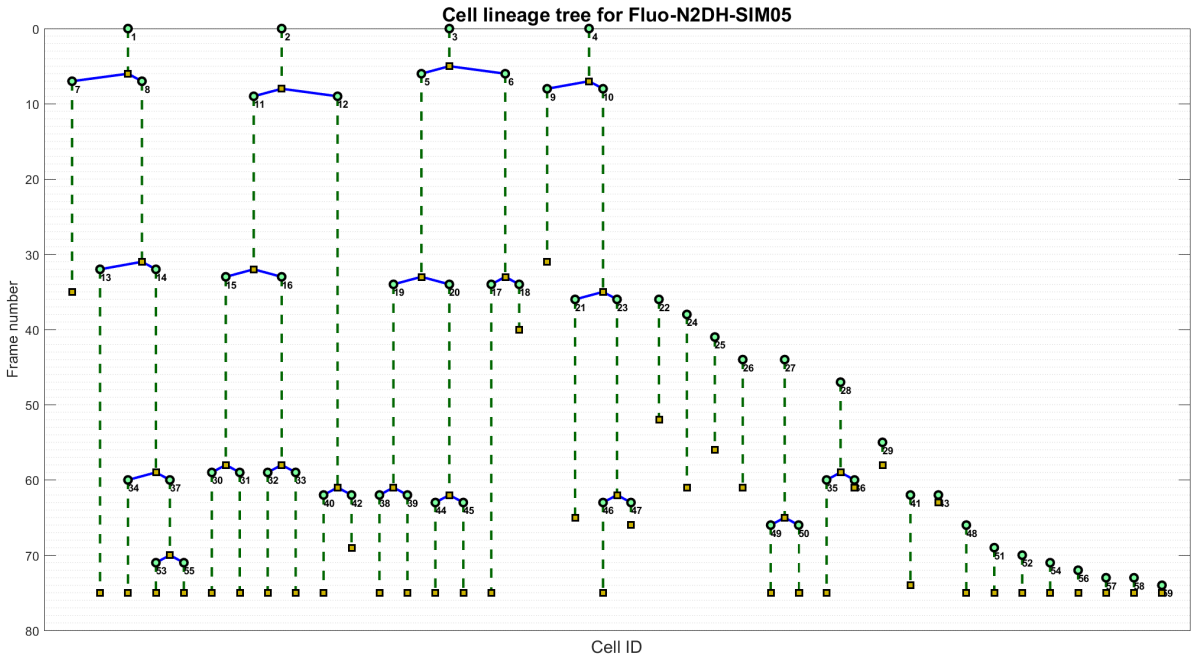

Figure 6.3: Cell lineage tree generated by our method on Fluo-N2DH-SIM05 dataset.

metrics such as symmetry and division times can be extracted from cell lineage. Types of motion can also be visually inferred from the 2D projections of trajectories. Straightforward applications include the development of predictive models for stem cell population growth and design, and optimization of subcultural strategies.

Cell Quantification

Another application is cell quantification and quantitative analysis. Quantification is the computation of biologically meaningful cell measures that can be divided into morphological, motility, diffusivity, and velocity measures. Morphological measures include the area, perimeter, major and minor principal axes, circularity, eccentricity, convexity. More sophisticated shape features can be computed using Fourier descriptors, Independent Component Analysis (ICA), and Principal Component Analysis (PCA). Motility measures are computed from the trajectories of the tracked cells using piecewise linear approximation. Typical motility measures include the total distance traveled by each cell, the net distance

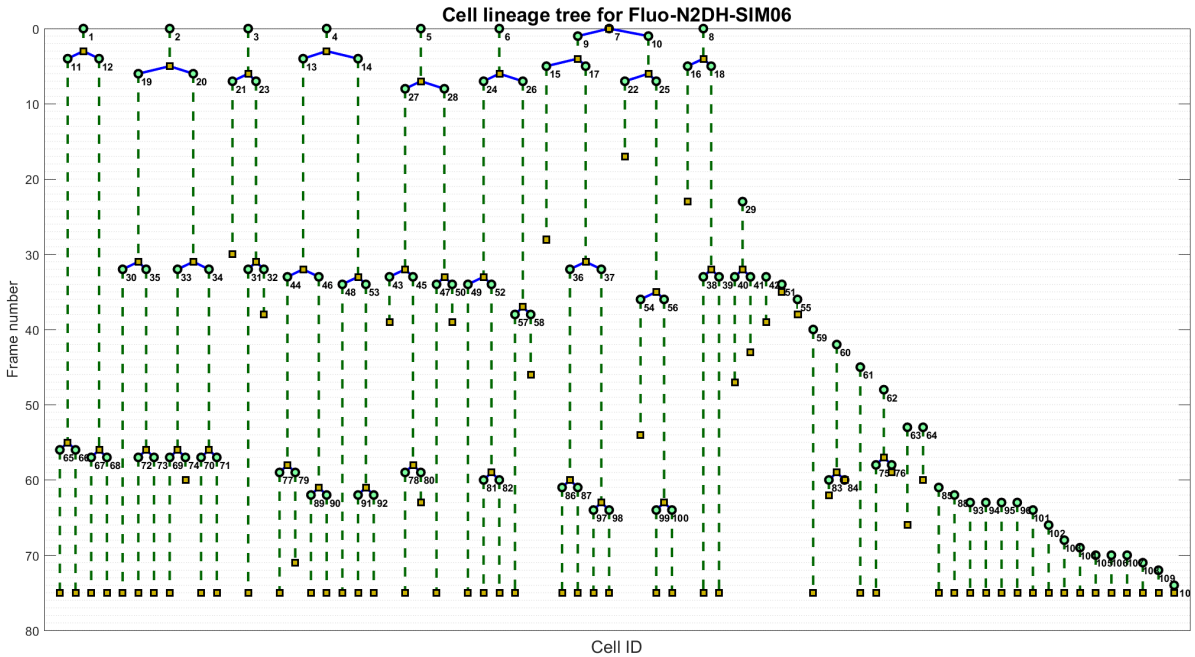

Figure 6.4: Cell lineage tree generated by our method on Fluo-N2DH-SIM06 dataset.

that is the distance between the start and the end points in a trajectory, the total trajectory time, or cell life time. An advanced measure of diffusivity is the Mean Squared Displacement (MSD) that is computed by the second-order moment of displacement as a function of time point difference and is defined as follows

$$MSD(n) = \frac{1}{N-n} \sum_{i=1}^{N-n} d^2 \left(\omega_i, \omega_{i+n}\right), \tag{6.4}$$

where $\omega_i = (x_i, y_i)$ is the centroid of a cell at time point i, N is the total trajectory lifetime, and n is the interval for computation of MSD. A frequent selection for the distance function $d(\cdot,\cdot)$ is the Euclidean distance $d\left(\omega_i, \omega_{i+n}\right) = \|\omega_i - \omega_{i+n}\|_2$. MSD is used for characterizing the mode of cell motion. We can accomplish this by observing the MSD-time curve. Some identifiable modes of cell motion are Brownian, anomalous diffusion, region-confined motion, directed motion, or immobility.

In our method we compute 26 morphological, motility, and diffusivity measures. More

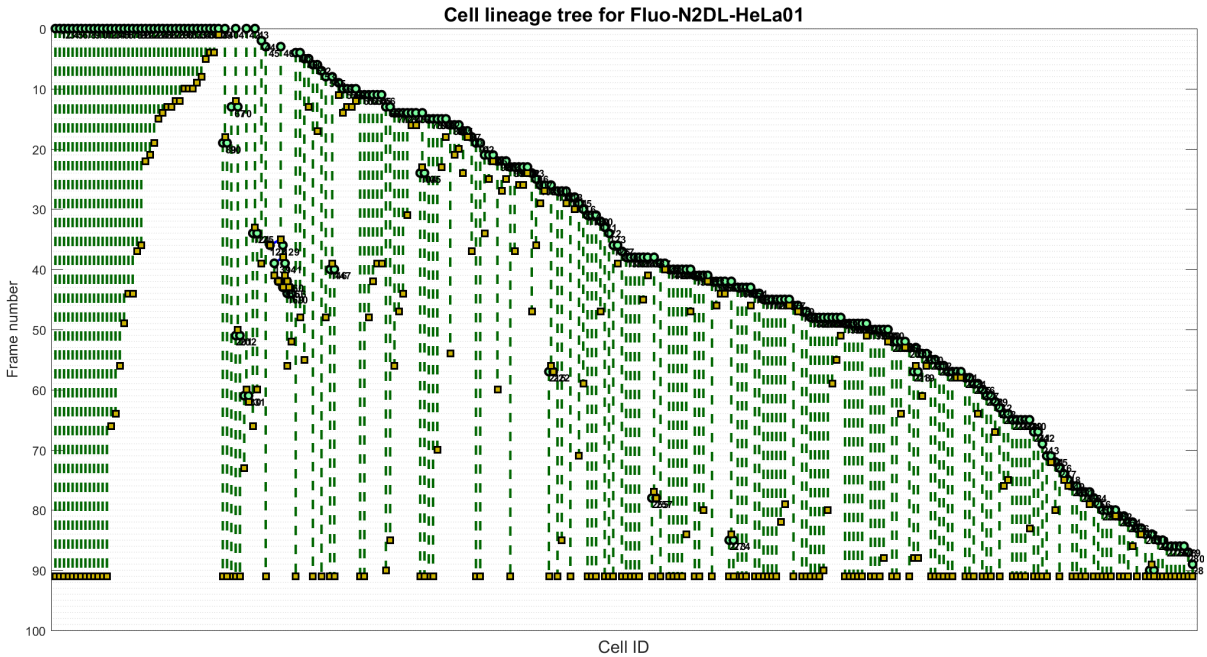

Figure 6.5: Cell lineage tree generated by our method on the dense dataset Fluo-Hela01. The number of tracks in ground truth is 265 and our tracking system detects 283 tracks resulting in TRA=0.992.

specifically in Table 6.3 we display computed motility and diffusivity measures for all cells of the sequence Fluo-C2DL-MSC01 displayed in Figures 6.18a and 6.18b. In Table 6.3 we can observe the variability of traveled distances and MSD measures. Furthermore Figures 6.19a and 6.19b illustrate the MSD function versus time and the mean MSD value for each cell for Fluo-C2DL-MSC01, Fluo-C2DL-MSC02, and N2DH-GOWT101. In these plots we can identify different motion modes including linear and exponential types. A linear MSD type indicates Brownian motion. A MSD curve approximated by a power law function may indicate superdiffusion, normal diffusion or, subdiffusion depending on the approximated power coefficient value. Our system automatically produces the quantification measures and related plots for all cells and trajectories for an input time-lapse sequence.

Table 6.1: TRA values obtained from our automated tracking on reference segmentation masks.

Dataset name	TRA_{GT}
N2DH-SIM01	0.999
N2DH-SIM02	0.998
N2DH-SIM03	0.997
N2DH-SIM04	0.999
N2DH-SIM05	0.988
N2DH-SIM06	0.997
C2DL-MSC01	0.999
C2DL-MSC02	0.973
N2DL-HeLa01	0.992
N2DL-HeLa02	0.97
N2DH-GOWT101	0.998
N2DH-GOWT102	0.996
Mean TRA_{GT}	**0.992**

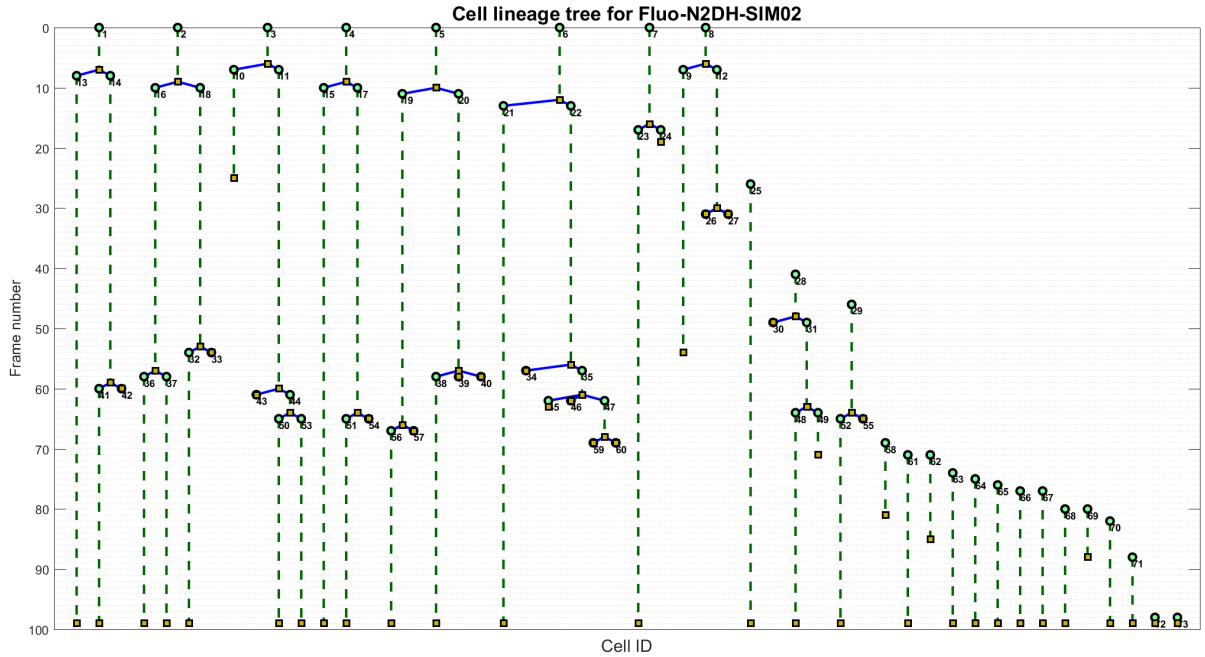

Figure 6.6: Cell lineage tree generated by our fully automated method on N2DH-SIM02 dataset.

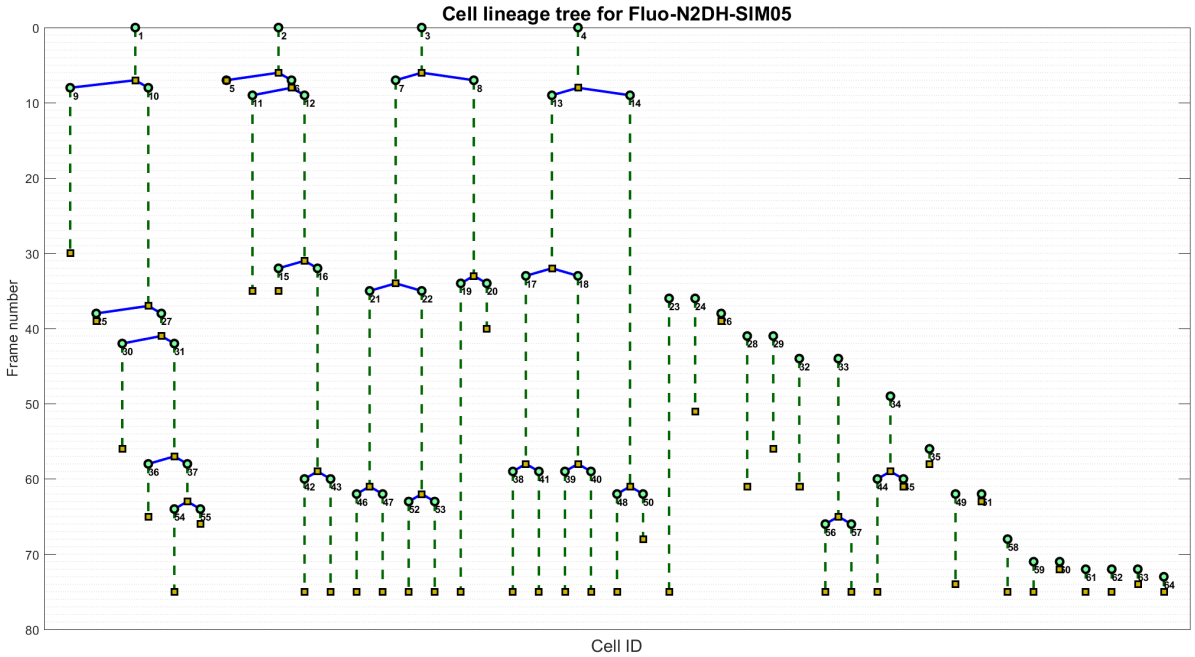

Figure 6.7: Cell lineage tree generated by our fully automated method on Fluo-N2DH-SIM05 dataset.

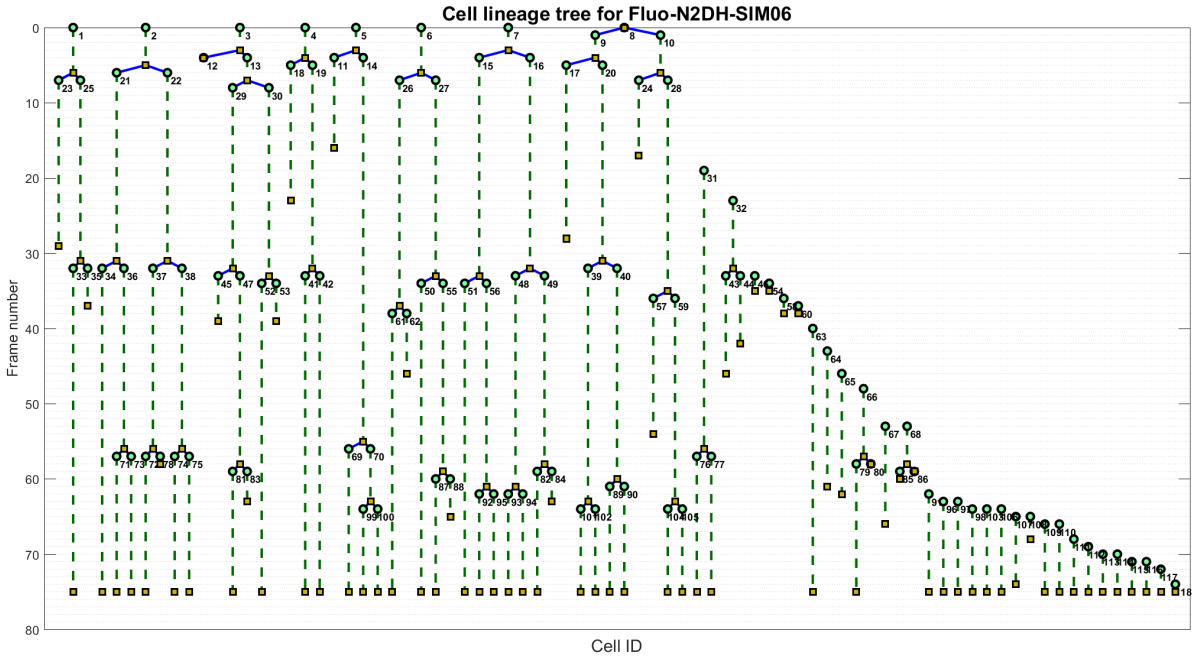

Figure 6.8: Cell lineage tree generated by our fully automated method on Fluo-N2DH-SIM06 dataset.

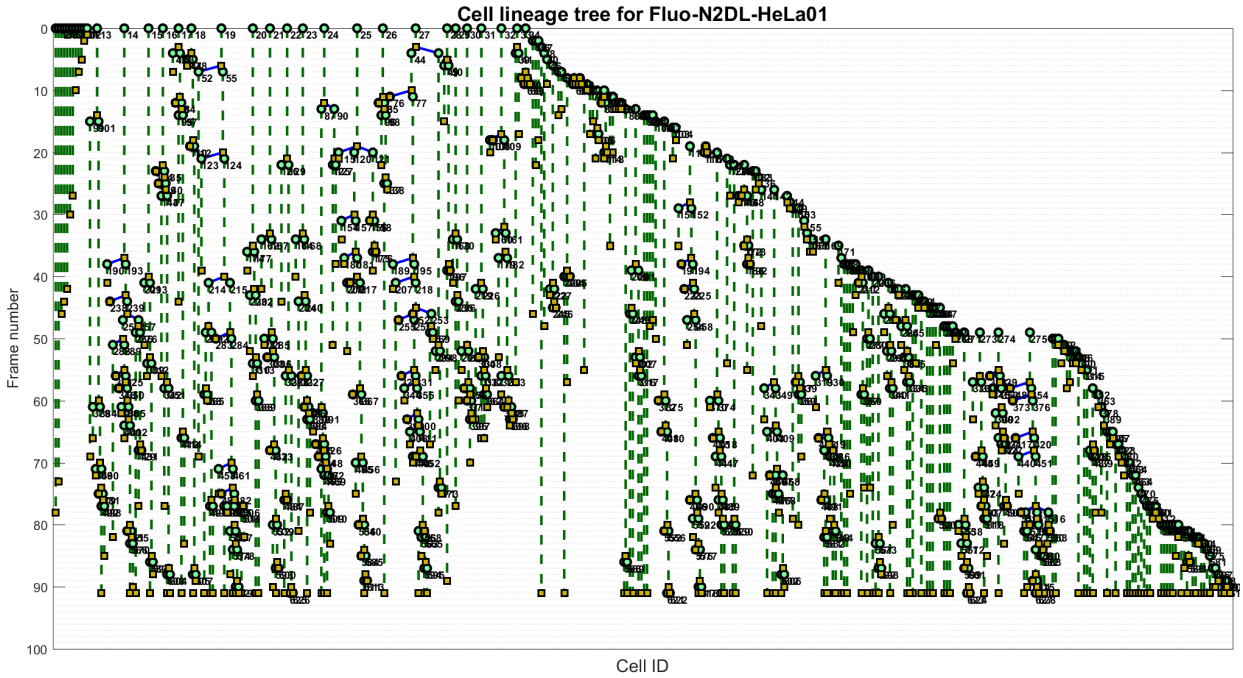

Figure 6.9: Cell lineage tree generated by our fully automated method on the dense dataset Fluo-Hela01 dataset. This case yields TRA=0.85.

Table 6.2: TRA values obtained from our automated tracking of each sequence on our segmentation results.

Dataset name	Size	Number of Frames	TRA
N2DH-SIM01	494x534	56	0.963
N2DH-SIM02	569x593	100	0.949
N2DH-SIM03	606x605	100	0.964
N2DH-SIM04	673x743	56	0.964
N2DH-SIM05	597x525	76	0.9399
N2DH-SIM06	655x735	76	0.973
C2DL-MSC01	992x832	48	0.853
C2DL-MSC02	1200x782	48	0.584
N2DL-HeLa01	1100x700	92	0.82
N2DL-HeLa02	1100x700	92	0.85
N2DH-GOWT101	1024x1024	92	0.913
N2DH-GOWT102	1024x1024	92	0.914

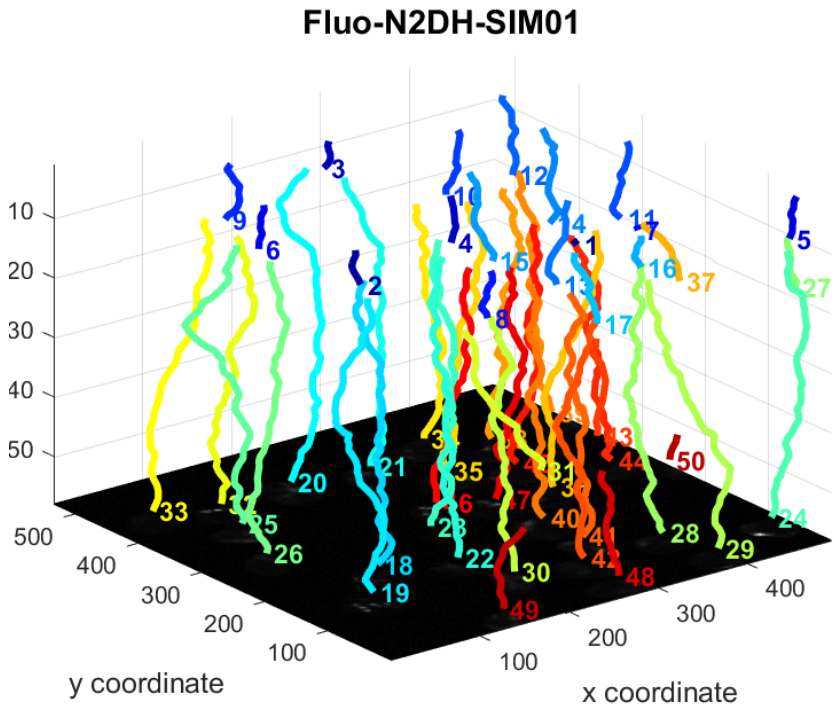

(a)

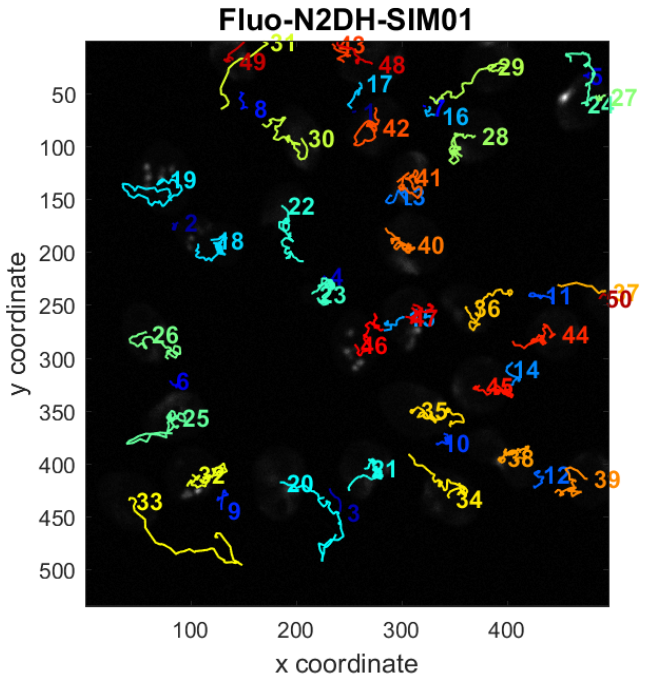

(b)

Figure 6.10: 2D+t and 2D displays of all cell trajectories of N2DH-SIM01 dataset.

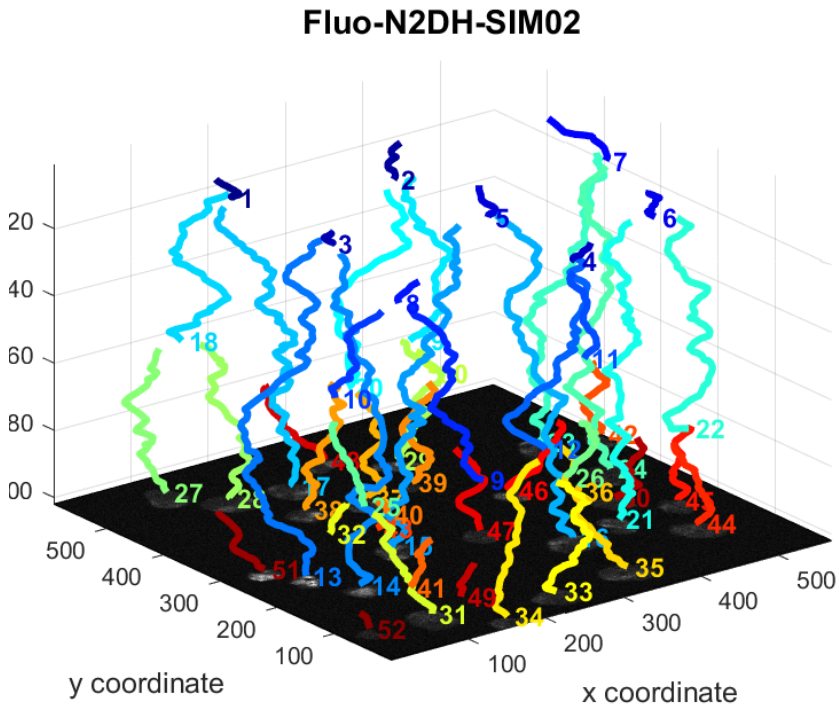

(a)

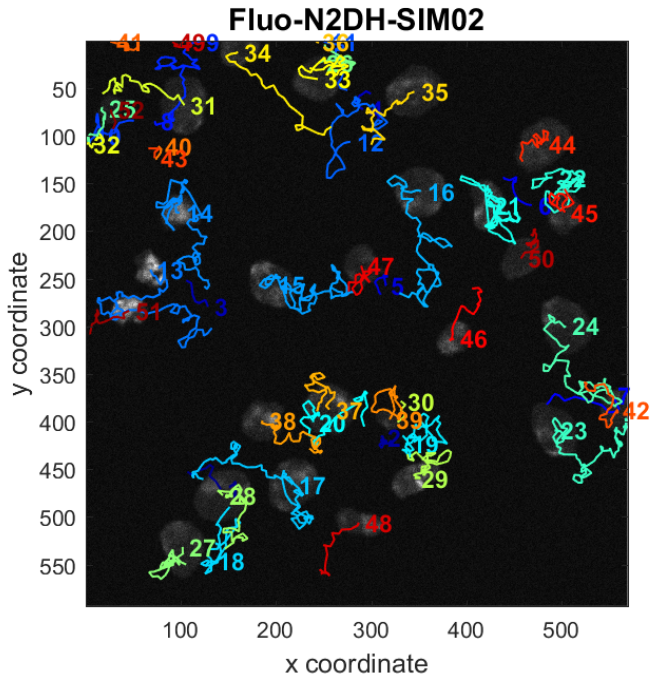

(b)

Figure 6.11: 2D+t and 2D displays of all cell trajectories of N2DH-SIM02 dataset.

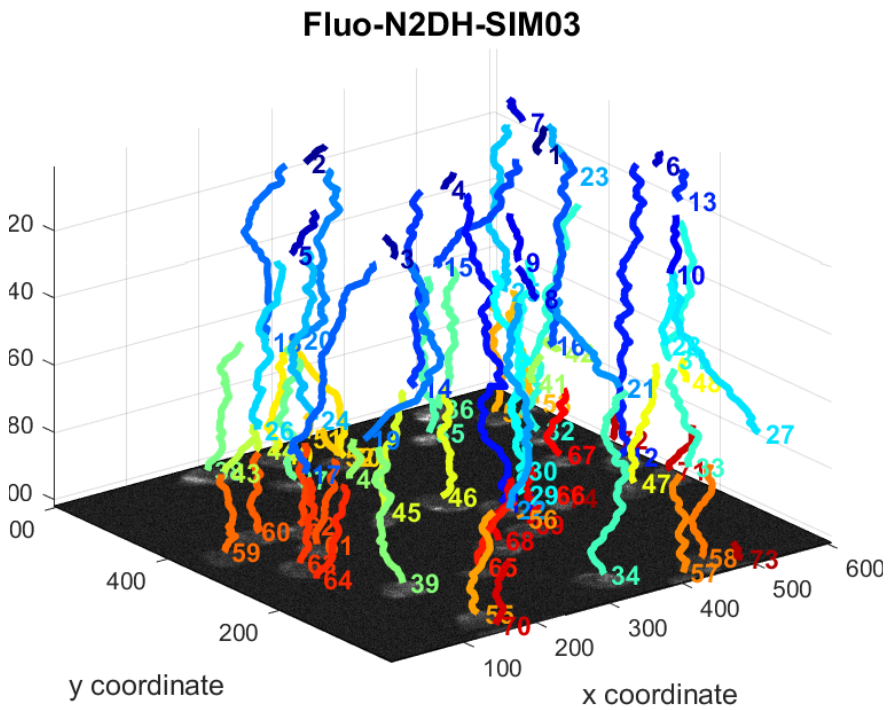

(a)

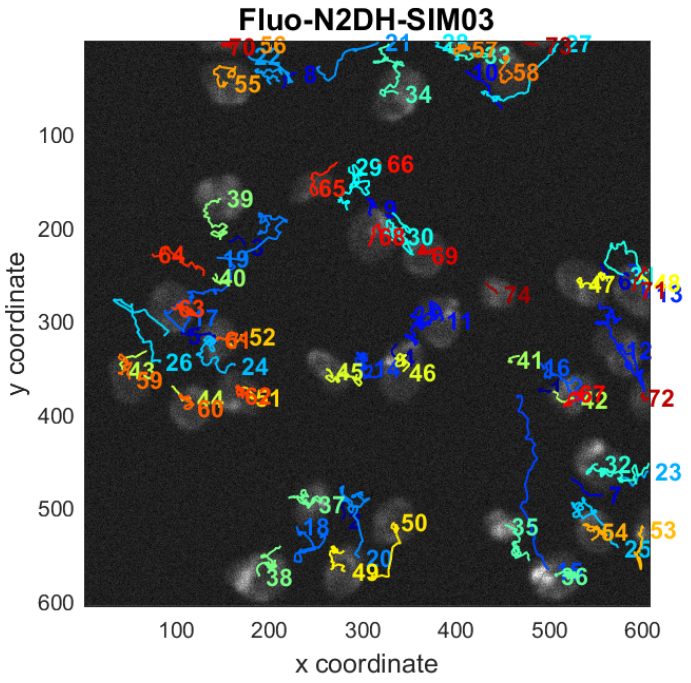

(b)

Figure 6.12: 2D+t and 2D displays of all cell trajectories of N2DH-SIM03 dataset.

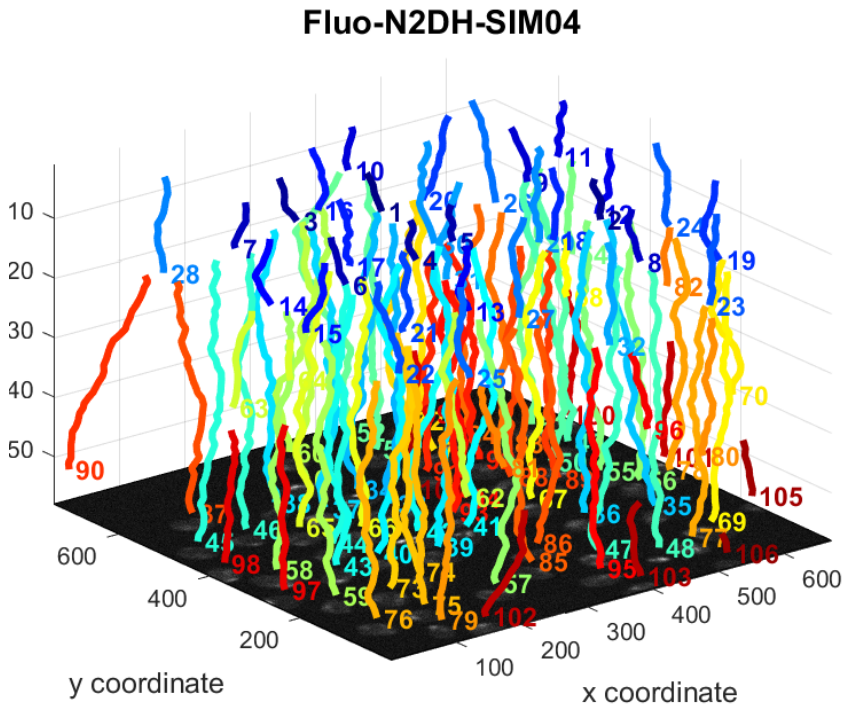

(a)

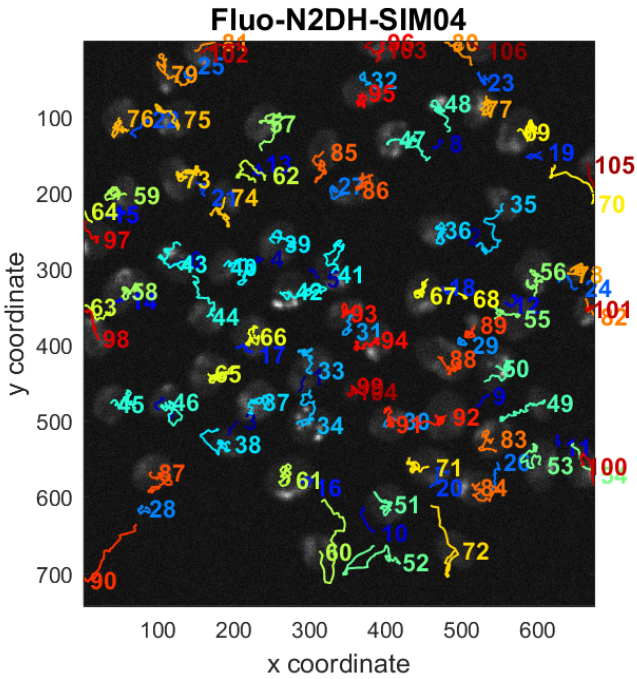

(b)

Figure 6.13: 2D+t and 2D displays of all cell trajectories of N2DH-SIM04 dataset.

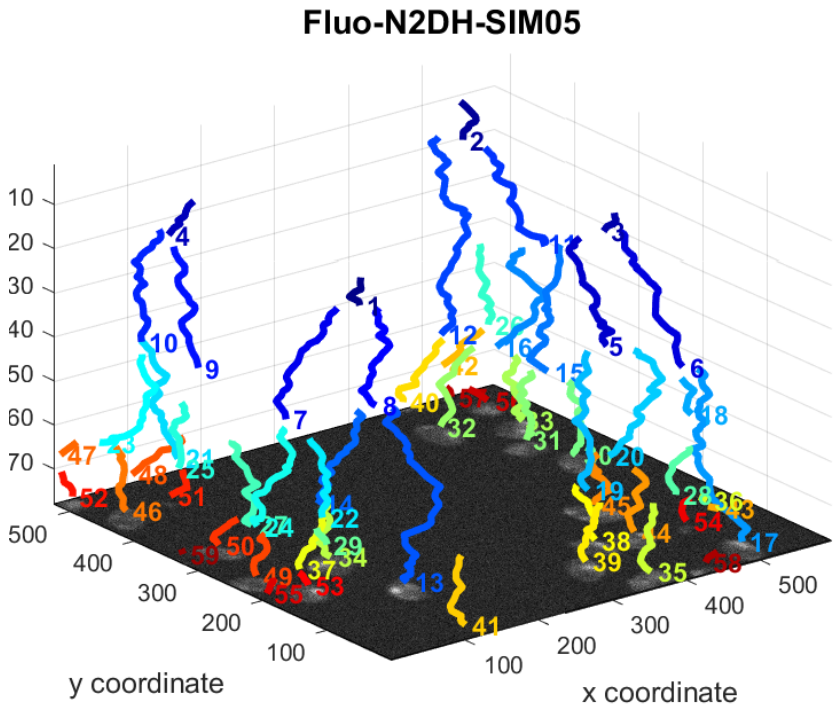

(a)

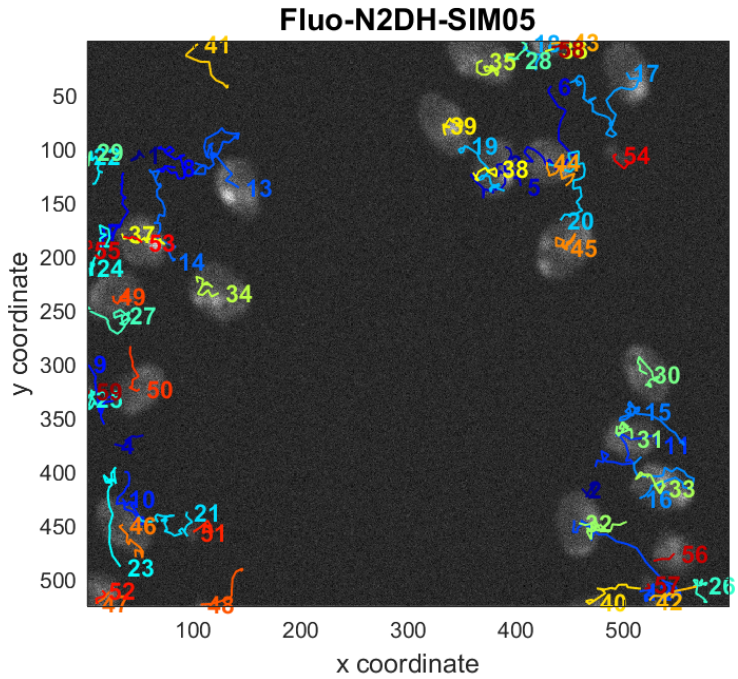

(b)

Figure 6.14: 2D+t and 2D displays of all cell trajectories of N2DH-SIM05 dataset.

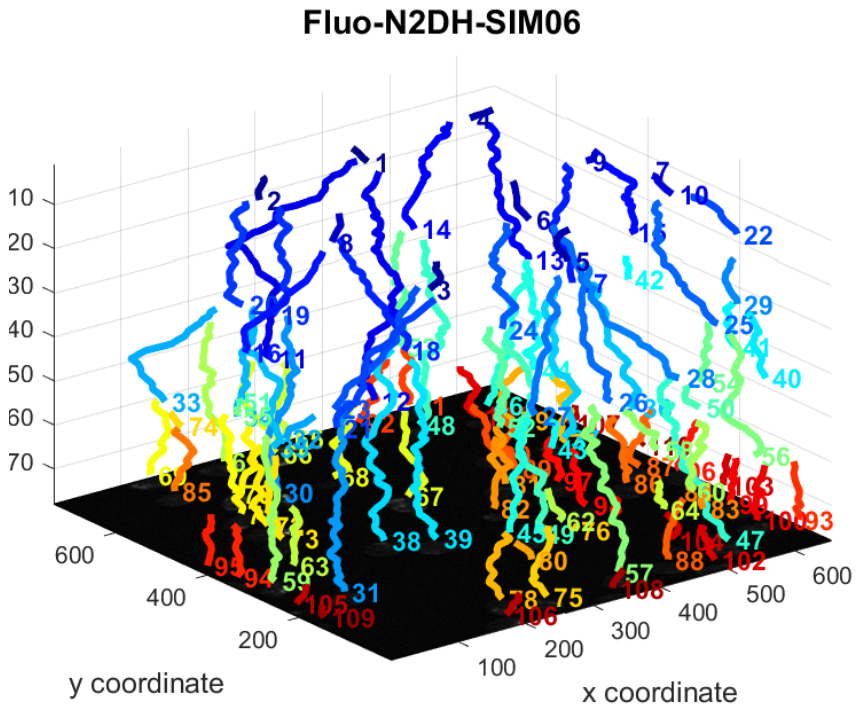

(a)

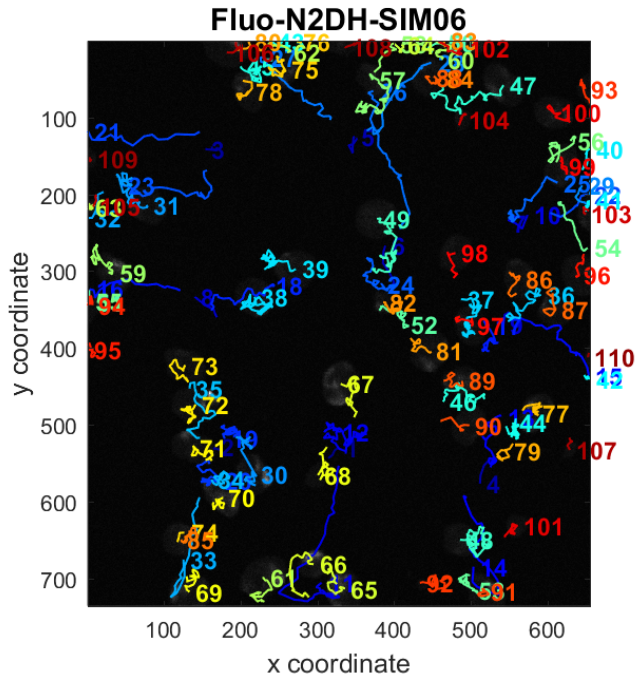

(b)

Figure 6.15: 2D+t and 2D displays of all cell trajectories of N2DH-SIM06 dataset.

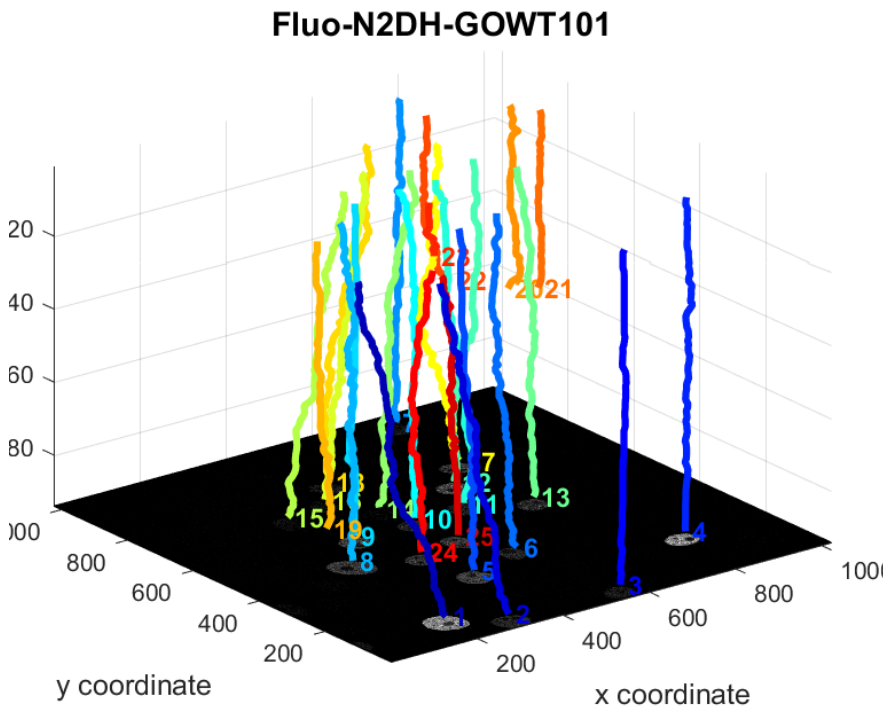

(a)

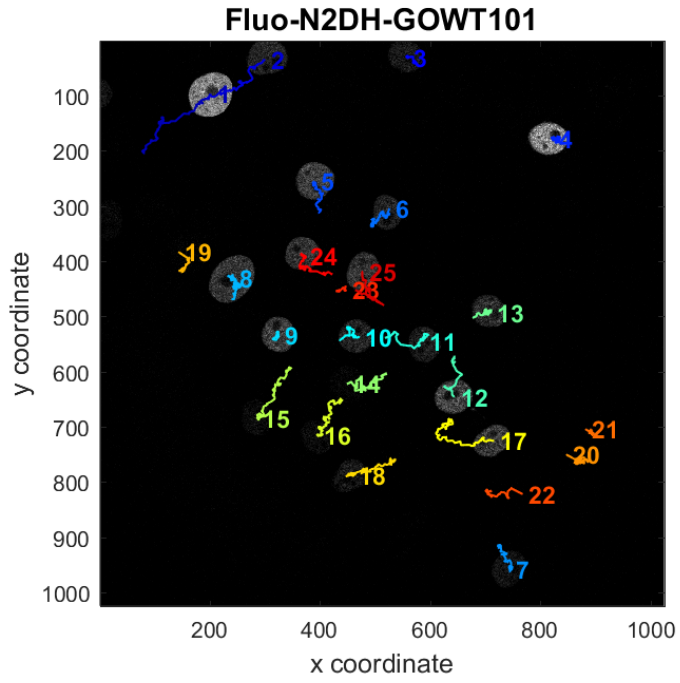

(b)

Figure 6.16: 2D+t and 2D displays of all cell trajectories of N2DH-GOWT101 dataset.

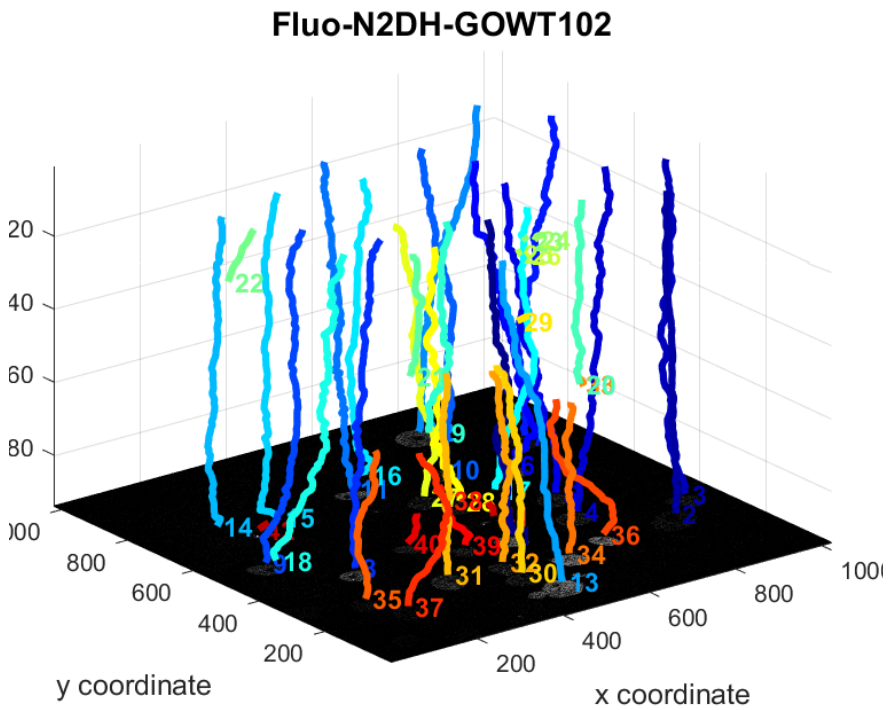

(a)

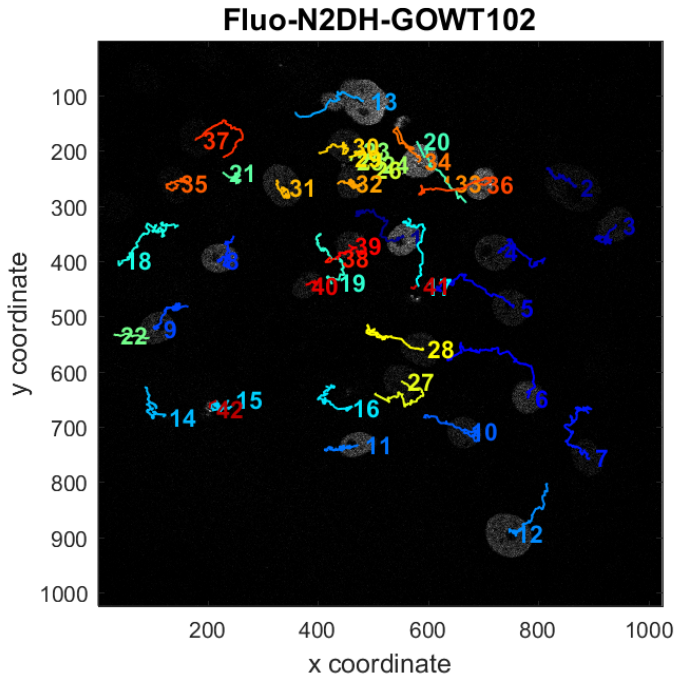

(b)

Figure 6.17: 2D+t and 2D displays of all cell trajectories of N2DH-GOWT102 dataset.

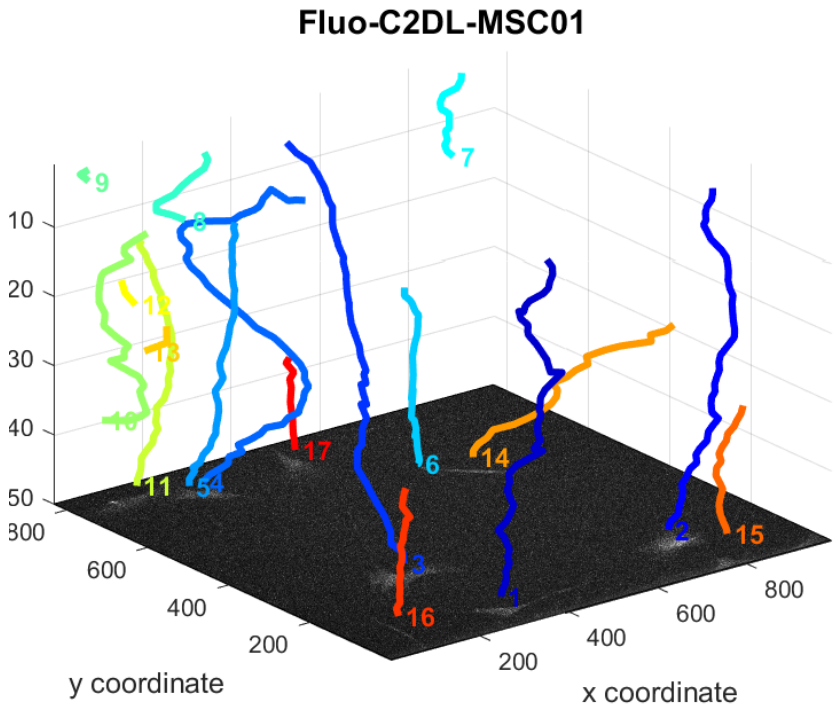

(a)

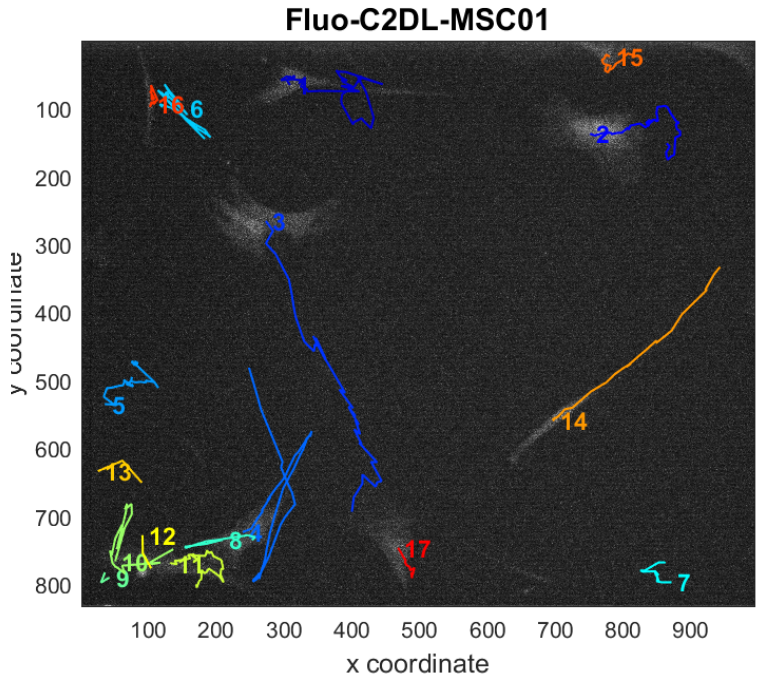

(b)

Figure 6.18: 2D+t and 2D displays of all cell trajectories of Fluo-C2DL-MSC01 dataset.

Cell Label	Life Time (min)	Total Traveled Distance (μm)	Net Traveled Distance (μm)	Mean MSD (μm^2)
1	960	247.2	39.6	1077.9
2	960	132.0	45.1	872.5
3	960	338.3	177.2	8709.3
4	960	319.1	96.2	2597.7
5	800	106.7	30.8	363.2
6	540	229.2	12.4	347.8
7	280	53.7	12.3	113.7
8	200	67.5	17.3	533.6
9	60	12.1	4.0	26.3
10	540	175.5	34.7	721.2
11	700	101.3	19.3	308.9
12	60	20.7	20.1	255.5
13	60	32.8	26.6	489.7
14	440	146.6	132.3	6506.4
15	380	45.5	13.4	106.2
16	400	41.4	7.8	26.8
17	260	28.4	16.2	108.1

Table 6.3: Dynamic cell features for Fluo-C2DL-MSC01. This is sample subset of the features computed by the proposed methodology over the complete frame sequence. The listed features are utilized to quantify motility and diffusivity.

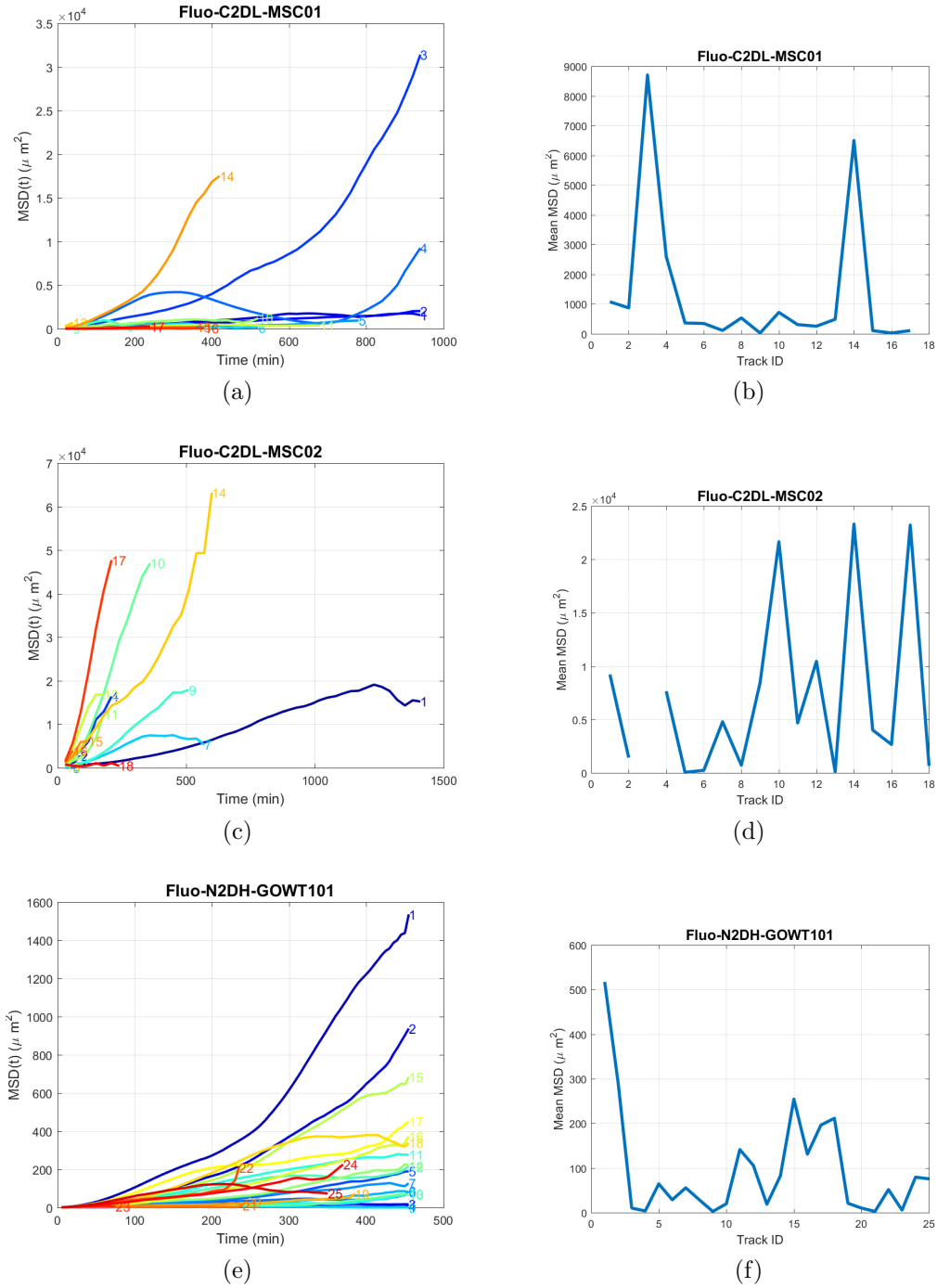

Figure 6.19: MSD function versus time and the MSD mean over time for each cell of the C2DL-MSC01 in (a) and (b), C2DL-MSC02 in (c) and (d), and N2DH-GOWT101 datasets in (e) and (f).

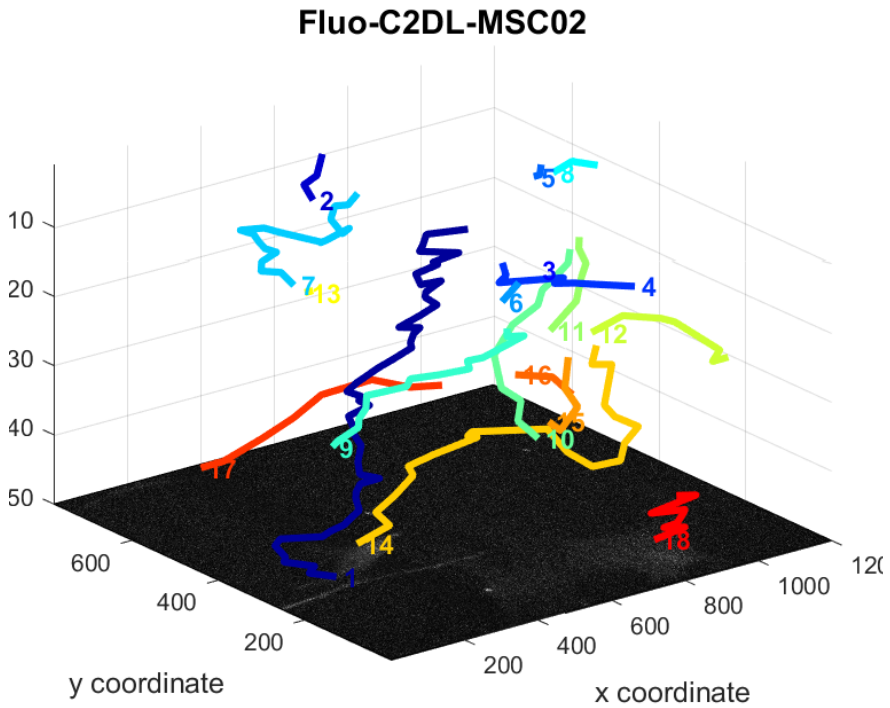

(a)

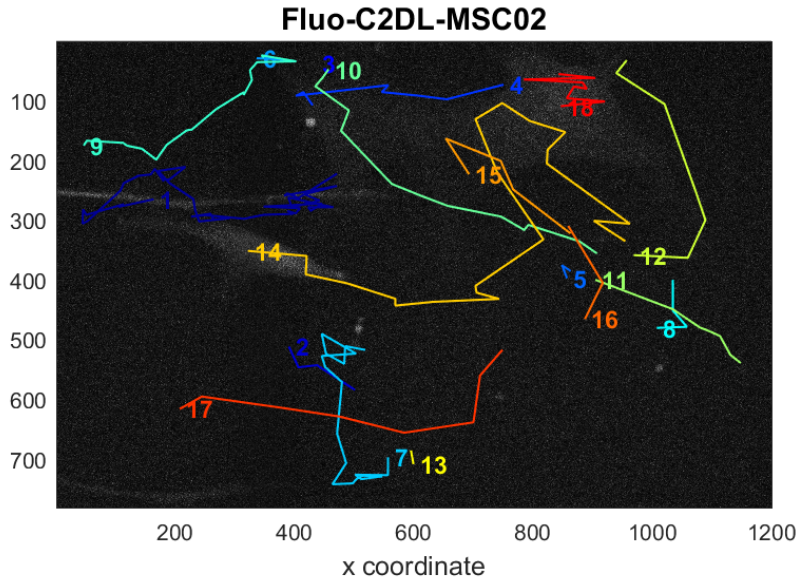

(b)

Figure 6.20: 2D+t and 2D displays of all cell trajectories of Fluo-C2DL-MSC02 dataset.

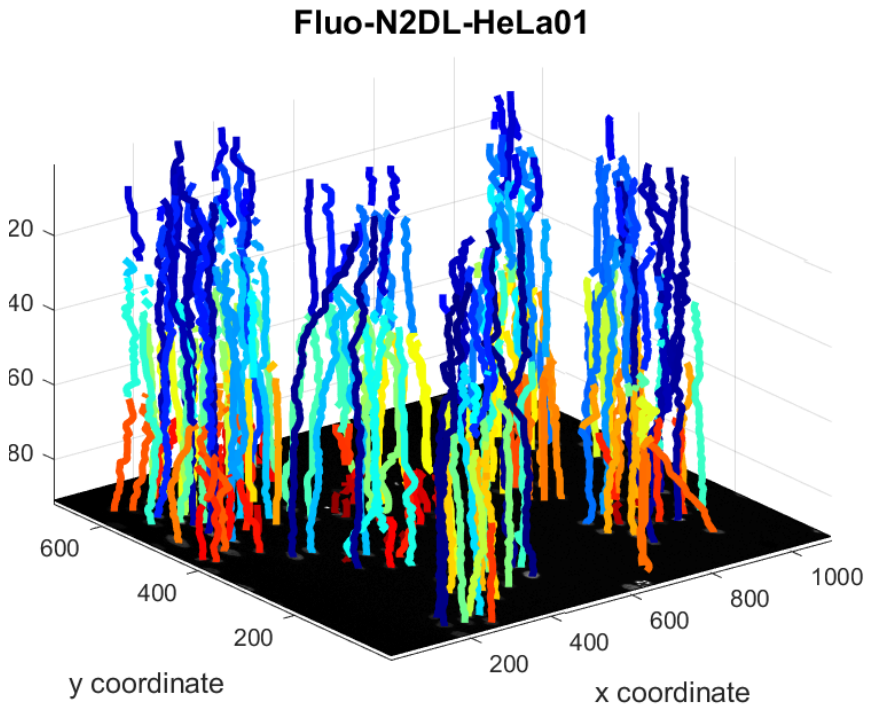

(a)

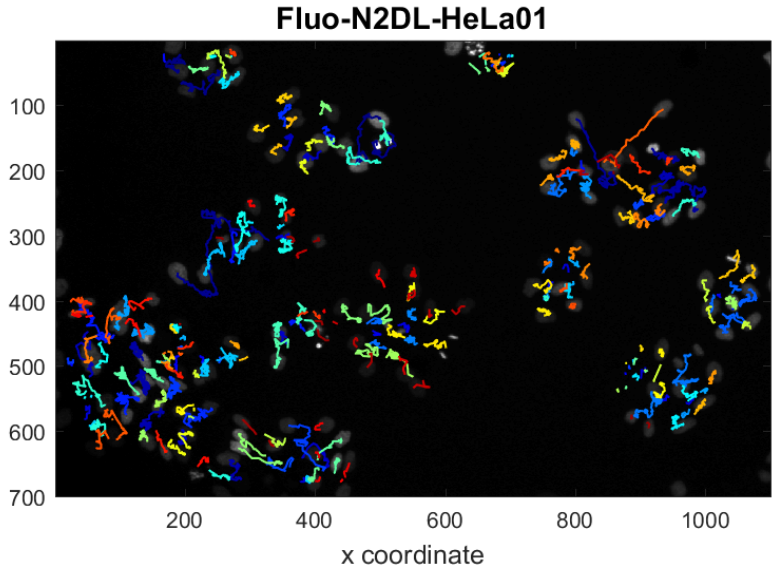

(b)

Figure 6.21: 2D+t and 2D displays of all cell trajectories of Fluo-N2DL-HeLa01 dataset.

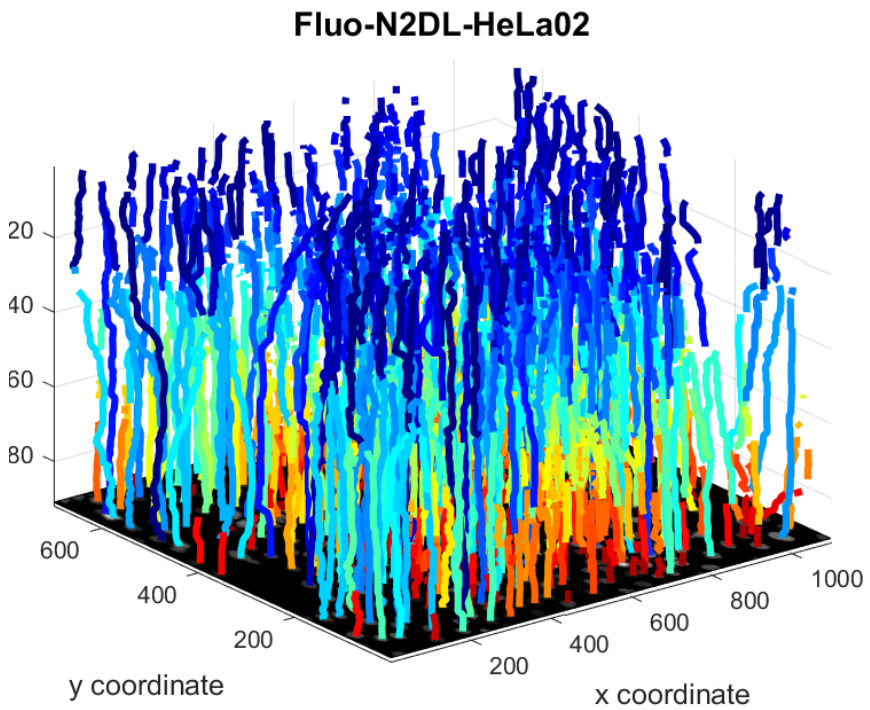

(a)

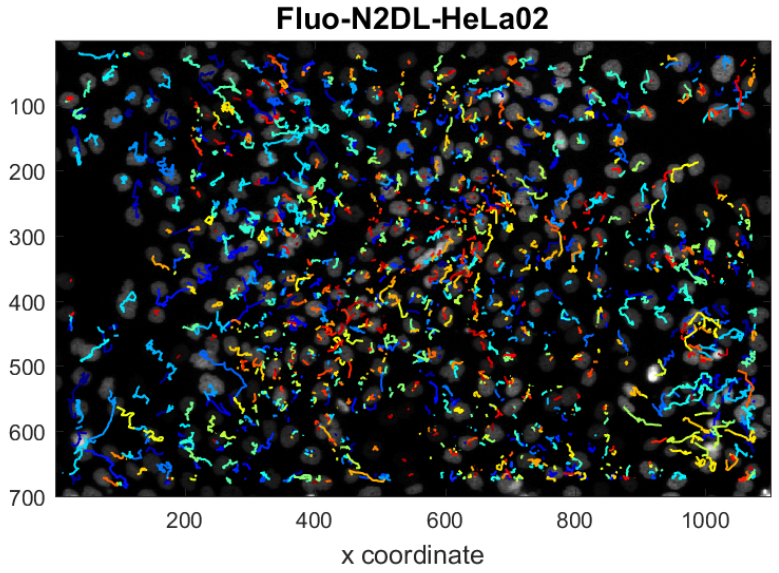

(b)

Figure 6.22: 2D+t and 2D displays of all cell trajectories of Fluo-N2DL-HeLa02 dataset.

Chapter VII: CONCLUSION

This dissertation focuses on the development of mathematical methods and algorithms for automated cell segmentation and tracking. This topic holds particular significance because it enables the analysis of large volumes of data and the quantification of biological processes and the development of novel approaches to observation of biological processes, diagnosis of diseases, and evaluation of drug performance among others.

In this work we first introduced a level-set and motion analysis co-operative approach to dynamic cell segmentation. One component of this approach performs nonlinear spatio-temporal diffusion-based motion analysis, Parzen kernel-based detection of discontinuities, and watershed-based foreground-background separation. This spatio-temporal analysis generates a delineation that we use as the initial level-set in a region-based temporally linked level-set model. The improvement in segmentation accuracy is mainly achieved by using both the local motion and the global statistical information for segmenting cells with heterogeneous intensity levels. We compared the performance of our approach denoted by ST-Diff-TCV, with two level-set based methods denoted by CV and TCV, and the ST-Diff method on simulated and real image sequences obtained from the online Cell Tracking challenge [25]. We validated the performances of all methods against reference manual cell delineations using the Dice coefficient. Every image sequence in our dataset addresses a different type of challenge for segmentation.

In comparison to CV and TCV, both ST-Diff and ST-Diff-TCV perform more robust cell segmentation, especially for cells undergoing mitosis, leaving and entering the field of view, and cells with lower mean intensity than the background intensity level. ST-Diff-TCV further improves the segmentation accuracy yielding and average Dice coefficient of 89% compared to ST-Diff average score of 85% by refining the cell delineation. Still, this method is dependent on some parameter retuning to optimize segmentation accuracy for different

types of imaging sequences. Overall, this approach is beneficial for quantification of a wide range of types of image sequences.

The second focal area of this dissertation was the design, development and validation of automated cell tracking approaches. We propose a probabilistic bi-frame matching approach that maximizes the likelihood measure derived from area overlapping between the cells of each frame and the warped cells of the previous frame. To estimate and predict the cell positions for cell correspondence analysis, we use a joint local-global optical flow method. In the next stage we propose to create the cell tracks by backtracking the cell correspondences from the last frame to the first and creating cell linked lists. Finally, we detect cell divisions by traversing the created cell linked lists, identifying common ancestors and eliminating intersections of cell tracks to create a new group of cell tracks. These operations ensure that the set of cell entities is divided into a formal partition. Then we construct a cell lineage tree that is used for visualization and validation. Finally, we compute morphological, diffusivity, motility and velocity cell measures for quantification.

We evaluated the performance of our segmentation and tracking approaches on datasets obtained from the online Cell Tracking challenge [25] using the TRA measure. Every dataset includes reference tracking results consisting of cell markers and cell acyclic graphs that we use to validate our approach. The results are encouraging even for datasets that include intensity variations, low intensity contrast, and high cell density. Our tracking method produces an average TRA measure of 99%, while the fully automated segmentation and the tracking performed at 89%.

In summary, the innovative parts of our work are:

- Intensity Standardization to address variability and differences in SNR and CNR by incorporating a histogram transformation approach for a robust and less sensitive parameter selection method and increase generalization capability of this approach that allows us to track diverse fluorescent cell types

- The refined cell detection method in the joint spatio-temporal domain instead of the spatial domain exclusively, can detect and segment cells that are hardly detectable using previous methods because they are rather detected by their high activity process
- The use of predicted cell motion by means of a Combined Local-Global Optical Flow technique with coarse to fine solution search strategy in a probabilistic Maximum Likelihood Bayesian decision framework to find cell correspondences between consecutive frames results in a very efficient tracking solution, while overcoming temporal sampling limitations of the image sequences
- Fully Automated cell tracking and lineage construction system enables the use of very large volumes of data for analysis.

REFERENCE LIST

[1] V. C. Abraham, D. Taylor, and J. R. Haskins. "High content screening applied to large-scale cell biology". In: *Trends in Biotechnology* 22.1 (2004), pp. 15–22. ISSN: 0167-7799. DOI: http://dx.doi.org/10.1016/j.tibtech.2003.10.012. URL: http://www.sciencedirect.com/science/article/pii/S0167779903003068.

[2] O. Al-Kofahi, R. J. Radke, S. K. Goderie, Q. Shen, S. Temple, and B. Roysam. "Automated cell lineage construction: a rapid method to analyze clonal development established with murine neural progenitor cells." eng. In: *Cell Cycle* 5.3 (2006), pp. 327–335.

[3] L. Ambrosio. "Regularity of solutions of a degenerate elliptic variational problem". In: *manuscripta mathematica* 68.1 (Dec. 1, 1990), pp. 309–326. DOI: 10.1007/BF02568766. URL: http://dx.doi.org/10.1007/BF02568766.

[4] L. Ambrosio. "Variational problems in SBV and image segmentation". In: *Acta Applicandae Mathematica* 17.1 (Oct. 1, 1989), pp. 1–40. DOI: 10.1007/BF00052492. URL: http://dx.doi.org/10.1007/BF00052492.

[5] V. L. A. Aubert G. "A variational method in image recovery". In: *SIAM* 34.5 (1997), pp. 1948–1979.

[6] J. L. Barron, D. J. Fleet, and S. S. Beauchemin. "Performance of optical flow techniques". In: *International Journal of Computer Vision* 12.1 (1994), pp. 43–77. ISSN: 1573-1405. DOI: 10.1007/BF01420984. URL: http://dx.doi.org/10.1007/BF01420984.

[7] R. Bise, T. Kanade, Z. Yin, and S. i. Huh. "Automatic cell tracking applied to analysis of cell migration in wound healing assay". In: *Proc. Annual Int. Conf. of the IEEE Engineering in Medicine and Biology Society*. Aug. 2011, pp. 6174–6179. DOI: 10.1109/IEMBS.2011.6091525.

[8] M. J. Black, G. Sapiro, D. H. Marimont, and D. Heeger. "Robust anisotropic diffusion." eng. In: *IEEE Trans Image Process* 7.3 (1998), pp. 421–432. DOI: 10.1109/83.661192. URL: http://dx.doi.org/10.1109/83.661192.

[9] F. Boukari and S. Makrogiannis. "Joint level-set and spatio-temporal motion detection for cell segmentation". In: *BMC Medical Genomics* 9.2:49 (Aug. 10, 2016). ISSN: 1755-8794. DOI: 10.1186/s12920-016-0206-5. URL: http://dx.doi.org/10.1186/s12920-016-0206-5.

[10] F. Boukari and S. Makrogiannis. "Spatio-temporal diffusion-based dynamic cell segmentation". In: *Bioinformatics and Biomedicine (BIBM), 2015 IEEE International Conference on*. 2015, pp. 317–324. DOI: 10.1109/BIBM.2015.7359701.

[11] F. Boukari and S. Makrogiannis. "Spatio-temporal Level-Set Based Cell Segmentation in Time-Lapse Image Sequences". English. In: *Advances in Visual Computing*. Ed. by G. Bebis, R. Boyle, B. Parvin, D. Koracin, R. McMahan, J. Jerald, H. Zhang, S. Drucker, C. Kambhamettu, M. El Choubassi, Z. Deng, and M. Carlson. Vol. 8888. Lecture Notes in Computer Science. Springer International Publishing, 2014, pp. 41–50. ISBN: 978-3-319-14363-7.

[12] F. Boukari, S. Makrogiannis, R. Nossal, and H. Boukari. "Imaging and tracking HIV viruses in human cervical mucus". In: *Journal of Biomedical Optics* 21.9 (2016), pp. 096001–1–096001–7. DOI: 10.1117/1.JBO.21.9.096001. URL: http://dx.doi.org/10.1117/1.JBO.21.9.096001.

[13] A. Braides. "Free discontinuity problems and their non-local approximation". In: *Calculus of Variations and Partial Differential Equations* (Jan. 1, 2000). DOI: 10.1007/978-3-642-57186-2_6. URL: http://dx.doi.org/10.1007/978-3-642-57186-2_6.

[14] A. Braides and G. Dal Maso. "Non-local approximation of the Mumford-Shah functional". In: *Calculus of Variations and Partial Differential Equations* 5.4 (May 1, 1997), pp. 293–322. ISSN: 1432-0835. DOI: 10.1007/s005260050068. URL: http://dx.doi.org/10.1007/s005260050068.

[15] A. Braides. "Examples of approximation". In: *Approximation of Free-Discontinuity Problems* (Jan. 1, 1998). DOI: 10.1007/BFb0097348. URL: http://dx.doi.org/10.1007/BFb0097348.

[16] K. M. Braun, C. Niemann, U. B. Jensen, J. P. Sundberg, V. Silva-Vargas, and F. M. Watt. "Manipulation of stem cell proliferation and lineage commitment: visualisation of label-retaining cells in wholemounts of mouse epidermis". In: *Development* 130.21 (2003), pp. 5241–5255. ISSN: 0950-1991. DOI: 10.1242/dev.00703. eprint: http://dev.biologists.org/content/130/21/5241.full.pdf. URL: http://dev.biologists.org/content/130/21/5241.

[17] T. Brox, A. Bruhn, N. Papenberg, and J. Weickert. "High accuracy optical flow estimation based on a theory for warping". In: *European Conference on Computer Vision (ECCV)*. Vol. 3024. Lecture Notes in Computer Science. Springer, 2004, pp. 25–36. URL: http://lmb.informatik.uni-freiburg.de//Publications/2004/Bro04a.

[18] A. Bruhn, J. Weickert, C. Feddern, T. Kohlberger, and C. Schnorr. "Variational optical flow computation in real time". In: *IEEE Transactions on Image Processing* 14.5 (May 2005), pp. 608–615. ISSN: 1057-7149. DOI: 10.1109/TIP.2005.846018.

[19] A. Bruhn, J. Weickert, and C. Schnörr. "Lucas/Kanade Meets Horn/Schunck: Combining Local and Global Optic Flow Methods". In: *International Journal of Computer Vision* 61.3 (2005), pp. 211–231. ISSN: 1573-1405. DOI: 10.1023/B:VISI.0000045324.43199.43. URL: http://dx.doi.org/10.1023/B:VISI.0000045324.43199.43.

[20] F. Bunyak, K. Palaniappan, S. K. Nath, T. L. Baskin, and G. Dong. "Quantitative cell motility for in vitro wound healing using level set-based active contour tracking". In: *Proc. 3rd IEEE Int. Symp. Biomedical Imaging: Nano to Macro*. Apr. 2006, pp. 1040–1043. DOI: 10.1109/ISBI.2006.1625099.

[21] M. Carriero, A. Leaci, and F. Tomarelli. "A Second Order Model in Image Segmentation: Blake & Zisserman Functional". In: *Variational Methods for Discontinuous Structures* (Jan. 1, 1996). DOI: 10.1007/978-3-0348-9244-5_5. URL: http://dx.doi.org/10.1007/978-3-0348-9244-5_5.

[22] M. Carriero, A. Leaci, and F. Tomarelli. "A Survey on the BlakeZisserman Functional". In: *Milan Journal of Mathematics* 83.2 (Dec. 1, 2015), pp. 397–420. ISSN: 1424-9294. DOI: 10.1007/s00032-015-0246-x. URL: http://dx.doi.org/10.1007/s00032-015-0246-x.

[23] M. Carriero, A. Leaci, and F. Tomarelli. "Local Minimizers for a Free Gradient Discontinuity Problem in Image Segmentation". In: *Variational Methods for Discontinuous Structures* (Jan. 1, 2002). DOI: 10.1007/978-3-0348-8193-7_5. URL: http://dx.doi.org/10.1007/978-3-0348-8193-7_5.

[24] V. Caselles, R. Kimmel, and G. Sapiro. "Geodesic Active Contours". In: *International Journal of Computer Vision* 22.1 (Feb. 1, 1997), pp. 61–79. ISSN: 1573-1405. DOI: 10.1023/A:1007979827043. URL: http://dx.doi.org/10.1023/A:1007979827043.

[25] *Cell Tracking Challenge*. 2013. URL: http://www.grand-challenge.org/.

[26] A. Chambolle. "Finite differences discretizations of the Mumford Shah functional." In: *Mathematical Modeling and Numerical Analysis* 33.2 (1999).

[27] A. Chambolle. "Image segmentation by variational methods: Mumford and Shah functional and the discrete approximation". In: *SIAM Journal of Applied Mathematics* 55.3 (1995), pp. 827–863.

[28] T. F. Chan and L. A. Vese. "Active Contours Without Edges". In: *Image Processing, IEEE Transactions on image processing* 10.2 (2001), pp. 266–277. DOI: 10.1109/83.902291. URL: http://dx.doi.org/10.1109/83.902291.

[29] T. F. Chan and L. A. Vese. "An active contour model without edges". In: *Int. Conf. Scale-Space Theories in Computer Vision*. 1999, pp. 141–151.

[30] C. Chen, W. Wang, J. A. Ozolek, and G. K. Rohde. "A flexible and robust approach for segmenting cell nuclei from 2D microscopy images using supervised learning and template matching". In: *Cytometry Part A* 83A.5 (2013), pp. 495–507. ISSN: 1552-4930. DOI: 10.1002/cyto.a.22280. URL: http://dx.doi.org/10.1002/cyto.a.22280.

[31] Y. Cheng. "Mean shift, mode seeking, and clustering". In: *IEEE transactions Pattern analysis machine intelligence* 17.8 (1995). IEEE Transactions on Pattern Analysis and Machine Intelligence, pp. 790–799.

[32] N. Chenouard, I. Bloch, and J.-C. Olivo-Marin. "Multiple hypothesis tracking for cluttered biological image sequences." eng. In: *IEEE Trans Pattern Anal Mach Intell* 35.11 (2013), pp. 2736–3750. DOI: 10.1109/TPAMI.2013.97. URL: http://dx.doi.org/10.1109/TPAMI.2013.97.

[33] N. Chenouard, I. Smal, F. de Chaumont, M. Maška, I. F. Sbalzarini, Y. Gong, J. Cardinale, C. Carthel, S. Coraluppi, M. Winter, A. R. Cohen, W. J. Godinez, K. Rohr, Y. Kalaidzidis, L. Liang, J. Duncan, H. Shen, Y. Xu, K. E. G. Magnusson, J. Jaldén, H. M. Blau, P. Paul-Gilloteaux, P. Roudot, C. Kervrann, F. Waharte, J.-Y. Tinevez, S. L. Shorte, J. Willemse, K. Celler, G. P. van Wezel, H.-W. Dan, Y.-S. Tsai, C. Ortiz de Solórzano, J.-C. Olivo-Marin, and E. Meijering. "Objective comparison of particle tracking methods." eng. In: *Nat Methods* 11.3 (2014), pp. 281–289. DOI: 10.1038/nmeth.2808. URL: http://dx.doi.org/10.1038/nmeth.2808.

[34] F. Cloppet and A. Boucher. "Segmentation of overlapping/aggregating nuclei cells in biological images". In: *Proc. 19th Int. Conf. Pattern Recognition*. Dec. 2008, pp. 1–4. DOI: 10.1109/ICPR.2008.4761451.

[35] D. Comaniciu and P. Meer. "Mean shift: a robust approach toward feature space analysis". In: *Pattern Analysis and Machine Intelligence, IEEE Transactions on* 24.5 (2002), pp. 603–619. DOI: http://dx.doi.org/10.1109/34.1000236. URL: http://dx.doi.org/10.1109/34.1000236.

[36] D. Cremers and C. Schnorr. "Statistical shape knowledge in variational motion segmentation". In: *Image and Vision Computing* 21 (2003).

[37] D. Cremers. "Image Segmentation with Shape Priors: Explicit Versus Implicit Representations". In: *Handbook of Mathematical Methods in Imaging*. Springer, Jan. 1, 2011. ISBN: 978-0-387-92919-4. DOI: 10.1007/978-0-387-92920-0_33. URL: http://dx.doi.org/10.1007/978-0-387-92920-0_33.

[38] D. Cremers, M. Rousson, and R. Deriche. "A Review of Statistical Approaches to Level Set Segmentation: Integrating Color, Texture, Motion and Shape". In: *International Journal of Computer Vision* 72.2 (2006), pp. 195–215. URL: http://www.springerlink.com/index/10.1007/s11263-006-8711-1.

[39] J. S. David Mumford. "Boundary detection by minimizing functionals". In: *In Proceedings of IEEE conference on computer vision and pattern recognition*. 1985, pp. 22–26.

[40] O. Debeir, P. Van Ham, R. Kiss, and C. Decaestecker. "Tracking of migrating cells under phase-contrast video microscopy with combined mean-shift processes." eng. In: *IEEE Trans Med Imaging* 24.6 (2005), pp. 697–711. DOI: 10.1109/TMI.2005.846851. URL: http://dx.doi.org/10.1109/TMI.2005.846851.

[41] H. Delingette and J. Montagnat. "Shape and Topology Constraints on Parametric Active Contours". In: *Computer Vision and Image Understanding* 83.2 (2001), pp. 140–171. DOI: 10.1006/cviu.2001.0920. URL: http://dx.doi.org/10.1006/cviu.2001.0920.

[42] C. Direkoglu and M. S. Nixon. "Moving-edge detection via heat flow analogy". In: *Pattern Recognition Letters* 32.2 (2011), pp. 270–279. ISSN: 0167-8655. DOI: http://dx.doi.org/10.1016/j.patrec.2010.08.012. URL: http://www.sciencedirect.com/science/article/pii/S0167865510002977.

[43] P. M. Dorin Comaniciu Visvanathan Ramesh. "Real-Time Tracking of Non-Rigid Objects using Mean Shift". In: *IEEE CVPR* (2000).

[44] J. Du, S. B. Fain, T. Gu, T. M. Grist, and C. A. Mistretta. "Noise reduction in MR angiography with nonlinear anisotropic filtering." In: *Journal of magnetic resonance imaging : JMRI* 19 (5 2004), pp. 632–639. ISSN: 1053-1807.

[45] R. O. Duda, P. E. Hart, and D. G. Stork. *Pattern Classification (2Nd Edition)*. Wiley-Interscience, 2000. ISBN: 0471056693.

[46] A. Dufour, R. Thibeaux, E. Labruyere, N. Guillen, and J.-C. Olivo-Marin. "3-D Active Meshes Fast Discrete Deformable Models for Cell Tracking in 3-D Time-Lapse Microscopy". In: *IEEE transactions on image processing* 20.7 (2011). IEEE Transactions on Image Processing, pp. 1925–1937.

[47] A. Dufour, V. Shinin, S. Tajbakhsh, N. Guillén-Aghion, J.-C. Olivo-Marin, and C. Zimmer. "Segmenting and tracking fluorescent cells in dynamic 3-D microscopy with coupled active surfaces." eng. In: *IEEE Trans Image Process* 14.9 (2005), pp. 1396–1410.

[48] O. Dzyubachyk, W. A. van Cappellen, J. Essers, W. J. Niessen, and E. H. W. Meijering. "Advanced Level-Set-Based Cell Tracking in Time-Lapse Fluorescence Microscopy". In: *IEEE Trans. Med. Imaging* 29.3 (2010), pp. 852–867. DOI: 10.1109/TMI.2009.2038693. URL: http://dx.doi.org/10.1109/TMI.2009.2038693.

[49] R. Eils and C. Athale. "Computational imaging in cell biology." eng. In: *J Cell Biol* 161.3 (2003), pp. 477–481. DOI: 10.1083/jcb.200302097. URL: http://dx.doi.org/10.1083/jcb.200302097.

[50] A. Ettinger and T. Wittmann. "Fluorescence Live Cell Imaging". In: *Methods in cell biology* 123 (2014), pp. 77–94.

[51] E. Faure, T. Savy, B. Rizzi, C. Melani, O. Stasova, D. Fabreges, R. Spir, M. Hammons, R. Cunderlik, G. Recher, B. Lombardot, L. Duloquin, I. Colin, J. Kollar, S. Desnoulez, P. Affaticati, B. Maury, A. Boyreau, J.-Y. Nief, P. Calvat, P. Vernier, M. Frain, G. Lutfalla, Y. Kergosien, P. Suret, M. Remesikova, R. Doursat, A. Sarti, K. Mikula, N. Peyrieras, and P. Bourgine. "A workflow to process 3D+time microscopy images of developing organisms and reconstruct their cell lineage". In: *Nature Communications* 7.8674 (Feb. 2016), pp. –. DOI: doi:10.1038/ncomms9674. URL: http://dx.doi.org/10.1038/ncomms9674.

[52] M. M. Frigault, J. Lacoste, J. L. Swift, and C. M. Brown. "Live-cell microscopy – tips and tools". In: *Journal of Cell Science* 122.6 (2009), pp. 753–767. ISSN: 0021-9533. DOI: 10.1242/jcs.033837. eprint: http://jcs.biologists.org/content/122/6/753.full.pdf. URL: http://jcs.biologists.org/content/122/6/753.

[53] S Gatz and J Herrmann. "Anisotropy, nonlocality, and space-charge field displacement in (2 + 1)-dimensional self-trapping in biased photorefractive crystals." In: *Optics letters* 23 (15 1998), pp. 1176–1178. ISSN: 0146-9592.

[54] G Gerig, O Kubler, R Kikinis, and F. A. Jolesz. "Nonlinear anisotropic filtering of MRI data." In: *IEEE transactions on medical imaging* 11 (2 1992), pp. 221–232. ISSN: 0278-0062.

[55] R. C. Gonzalez and R. E. Woods. *Digital Image Processing (3rd Ed.)* Prentice Hall, 2008.

[56] N. Harder, F. Mora-Bermúdez, W. J. Godinez, J. Ellenberg, R. Eils, and K. Rohr. "Automated analysis of the mitotic phases of human cells in 3D fluorescence microscopy image sequences." eng. In: *Med Image Comput Comput Assist Interv* 9.1 (2006), pp. 840–848.

[57] B. K. P. Horn and B. G. Schunck. "Determining Optical Flow". In: *ARTIFICAL INTELLIGENCE* 17 (1981), pp. 185–203.

[58] A. Izenman. "Recent Developments in Nonparametric Density Estimation". In: *Journal of The American Statistical Association* 86 (1991), pp. 205–224.

[59] C. Jung and C. Kim. "Segmenting Clustered Nuclei Using H-minima Transform-Based Marker Extraction and Contour Parameterization". In: *IEEE Transactions on Biomedical Engineering* 57.10 (Oct. 2010), pp. 2600–2604. ISSN: 0018-9294. DOI: 10.1109/TBME.2010.2060336.

[60] T. Kanade and K. Li. "Tracking of Migrating and Proliferating Cells in Phase-Contrast Microscopy Imagery for Tissue Engineering". In: *Computer Vision for Biomedical Image Applications*. Springer, Jan. 1, 2005. ISBN: 978-3-540-29411-5. DOI: 10.1007/11569541_4. URL: http://dx.doi.org/10.1007/11569541_4.

[61] M. Kass, A. Witkin, and D. Terzopoulos. "Snakes: Active contour models". In: *International Journal of Computer Vision* 1.4 (1988), pp. 321–331. DOI: http://dx.doi.org/10.1007/BF00133570. URL: http://dx.doi.org/10.1007/BF00133570.

[62] R. Kimmel, N. Kiryati, and A. M. Bruckstein. "Sub-pixel distance maps and weighted distance transforms". In: *Journal of Mathematical Imaging and Vision* 6.2-3 (2 June 1, 1996), pp. 223–233. ISSN: 1573-7683. DOI: 10.1007/BF00119840. URL: http://dx.doi.org/10.1007/BF00119840.

[63] K. Kretzschmar and F. Watt. "Lineage Tracing". In: *Cell* 148.12 (2012), pp. 33–45. ISSN: 0092-8674. DOI: http://dx.doi.org/10.1016/j.cell.2012.01.002. URL: http://www.sciencedirect.com/science/article/pii/S0092867412000037.

[64] M. Leventon, O. Faugeras, and W. Grimson. "Level set based segmentation with intensity and curvature priors". In: *IEEE Workshop on Mathematical Methods in Biomedical Image Analysis Proceedings*. 2000, pp. 4–11. URL: citeseer.comp.nus.edu.sg/484457.html.

[65] F. Li, X. Zhou, J. Ma, and S. T. C. Wong. "Multiple Nuclei Tracking Using Integer Programming for Quantitative Cancer Cell Cycle Analysis". In: *IEEE Transactions on Medical Imaging* 29.1 (2010), pp. 96–105. ISSN: 0278-0062. DOI: 10.1109/TMI.2009.2027813.

[66] K. Li, E. D. Miller, M. Chen, T. Kanade, L. E. Weiss, and P. G. Campbell. "Cell population tracking and lineage construction with spatiotemporal context." eng. In: *Med Image Anal* 12.5 (2008), pp. 546–566. DOI: 10.1016/j.media.2008.06.001. URL: http://dx.doi.org/10.1016/j.media.2008.06.001.

[67] K. Li, E. D. Miller, L. E. Weiss, P. G. Campbell, and T. Kanade. "Online Tracking of Migrating and Proliferating Cells Imaged with Phase-Contrast Microscopy". In: *IEEE Proc. Conf. Computer Vision and Pattern Recognition Workshop (CVPRW'06)*. June 2006, pp. 65–72. DOI: 10.1109/CVPRW.2006.150.

[68] L. Liang, H. Shen, P. Rompolas, V. Greco, P. De Camilli, and J. S. Duncan. "A multiple hypothesis based method for particle tracking and its extension for cell segmentation." eng. In: *Inf Process Med Imaging* 23 (2013), pp. 98–109.

[69] Liang Liang, Hongying Shen, P. De Camilli, and J. S. Duncan. "A novel multiple hypothesis based particle tracking method for clathrin mediated endocytosis analysis using fluorescence microscopy." eng. In: *IEEE Trans Image Process* 23.4 (2014), pp. 1844–1857. DOI: 10.1109/TIP.2014.2303633. URL: http://dx.doi.org/10.1109/TIP.2014.2303633.

[70] C. Liu, W. T. Freeman, E. H. Adelson, and Y. Weiss. "Human-assisted motion annotation". In: *2008 IEEE Conference on Computer Vision and Pattern Recognition*. Anchorage, AK, USA: IEEE, June 2008, pp. 1–8. ISBN: 978-1-4244-2242-5. DOI: 10.1109/cvpr.2008.4587845. URL: http://dx.doi.org/10.1109/cvpr.2008.4587845.

[71] B. D. Lucas and T. Kanade. "An Iterative Image Registration Technique with an Application to Stereo Vision (IJCAI)". In: *Proceedings of the 7th International Joint Conference on Artificial Intelligence (IJCAI '81)*. 1981, pp. 674–679.

[72] K. E. G. Magnusson, J. Jalden, P. M. Gilbert, and H. M. Blau. "Global linking of cell tracks using the Viterbi algorithm." eng. In: *IEEE Trans Med Imaging* 34.4 (2015), pp. 911–929. DOI: 10.1109/TMI.2014.2370951. URL: http://dx.doi.org/10.1109/TMI.2014.2370951.

[73] S. Makrogiannis and N. Bourbakis. "Motion analysis with application to assistive vision technology". In: *Tools with Artificial Intelligence, 2004. ICTAI 2004. 16th IEEE International Conference on*. 2004, pp. 344–352. DOI: 10.1109/ICTAI.2004.89.

[74] S. Makrogiannis, R. Bhotika, J. V. Miller, J. Skinner, and M. Vass. "Nonparametric Intensity Priors for Level Set Segmentation of Low Contrast Structures". In: *Medical Image Computing and Computer-Assisted Intervention – MICCAI 2009: 12th International Conference, London, UK, September 20-24, 2009, Proceedings, Part I*. Ed. by G.-Z. Yang, D. Hawkes, D. Rueckert, A. Noble, and C. Taylor. Berlin, Heidelberg: Springer Berlin Heidelberg, 2009, pp. 239–246. ISBN: 978-3-642-04268-3. DOI:

10.1007/978-3-642-04268-3_30. URL: http://dx.doi.org/10.1007/978-3-642-04268-3_30.

[75] R. Malladi, J. A. Sethian, and B. C. Vemuri. "Shape Modeling with Front Propagation: A Level Set Approach". In: *IEEE Transactions on Pattern Analysis and Machine Intelligence* 17 (1995), pp. 158–175. ISSN: 0162-8828. DOI: http://doi.ieeecomputersociety.org/10.1109/34.368173.

[76] H. Mao, H. Liu, and P. Shi. "Neighbor-constrained active contours without edges". In: *Proc. IEEE Computer Society Conf. Computer Vision and Pattern Recognition Workshops CVPRW '08*. June 2008, pp. 1–7. DOI: 10.1109/CVPRW.2008.4562995.

[77] M. Maska, V. Ulman, D. Svoboda, P. Matula, P. Matula, C. Ederra, A. Urbiola, T. Espana, S. Venkatesan, D. M. W. Balak, P. Karas, T. Bolckova, M. Streitova, C. Carthel, S. Coraluppi, N. Harder, K. Rohr, K. E. G. Magnusson, J. Jalden, H. M. Blau, O. Dzyubachyk, P. Kizek, G. M. Hagen, D. Pastor-Escuredo, D. Jimenez-Carretero, M. J. Ledesma-Carbayo, A. Munoz-Barrutia, E. Meijering, M. Kozubek, and C. Ortiz-de Solorzano. "A benchmark for comparison of cell tracking algorithms." eng. In: *Bioinformatics* 30.11 (2014), pp. 1609–1617. DOI: 10.1093/bioinformatics/btu080. URL: http://dx.doi.org/10.1093/bioinformatics/btu080.

[78] C. R. Maurer, R. Qi, and V. Raghavan. "A linear time algorithm for computing exact Euclidean distance transforms of binary images in arbitrary dimensions". In: *IEEE Transactions on Pattern Analysis and Machine Intelligence* 25.2 (Feb. 2003), pp. 265–270. ISSN: 0162-8828. DOI: 10.1109/TPAMI.2003.1177156.

[79] T. McInerney and D. Terzopoulos. "T-snakes: Topology adaptive snakes". In: *Medical Image Analysis* 4.2 (2000), pp. 73 –91. ISSN: 1361-8415. DOI: http://dx.doi.org/10.1016/S1361-8415(00)00008-6. URL: http://www.sciencedirect.com/science/article/pii/S1361841500000086.

[80] E. Meijering, I. Smal, and G. Danuser. "Tracking in molecular bioimaging". In: *IEEE Signal Processing Magazine* 23.3 (May 2006), pp. 46–53. ISSN: 1053-5888. DOI: 10.1109/MSP.2006.1628877.

[81] E. Meijering, O. Dzyubachyk, and I. Smal. "Methods for cell and particle tracking." eng. In: *Methods Enzymol* 504 (2012), pp. 183–200. DOI: 10.1016/B978-0-12-391857-4.00009-4. URL: http://dx.doi.org/10.1016/B978-0-12-391857-4.00009-4.

[82] M. Moraschi, G. E. Hagberg, M. Di Paola, G. Spalletta, B. Maraviglia, and F. Giove. "Smoothing that does not blur: effects of the anisotropic approach for evaluating diffusion tensor imaging data in the clinic." In: *Journal of magnetic resonance imaging : JMRI* 31 (3 2010), pp. 690–697. ISSN: 1522-2586. DOI: 10.1002/jmri.22040.

[83] R. B. M.Sonka V. Hlavac. *Image processing, Analysis, and Machine Vision*. Ed. by T. Learning. 3rd ed. THOMSON Learning, 2008.

[84] D. P. Mukherjee, N. Ray, and S. T. Acton. "Level set analysis for leukocyte detection and tracking." eng. In: *IEEE Trans Image Process* 13.4 (2004), pp. 562–572.

[85] D. Mumford and J. Shah. "Optimal approximations by piecewise smooth functions and associated variational problems". In: *Comm. on Pure and Applied Mathematics* 42.5 (1989), pp. 577–685. ISSN: 00103640. DOI: 10.1002/cpa.3160420503. URL: http://doi.wiley.com/10.1002/cpa.3160420503.

[86] S. K. Nath, K. Palaniappan, and F. Bunyak. "Cell segmentation using coupled level sets and graph-vertex coloring." eng. In: *Med Image Comput Comput Assist Interv* 9.Pt 1 (2006), pp. 101–108.

[87] S. K. Nath, K. Palaniappan, and F. Bunyak. "Medical Image Computing and Computer-Assisted Intervention – MICCAI 2006: 9th International Conference, Copenhagen, Denmark, October 1-6, 2006. Proceedings, Part I". In: ed. by R. Larsen, M. Nielsen, and J. Sporring. Berlin, Heidelberg: Springer Berlin Heidelberg, 2006. Chap. Cell Segmentation Using Coupled Level Sets and Graph-Vertex Coloring, pp. 101–108. ISBN: 978-3-540-44708-5. DOI: 10.1007/11866565_13. URL: http://dx.doi.org/10.1007/11866565_13.

[88] D. Padfield, J. Rittscher, and B. Roysam. "Spatio-temporal cell segmentation and tracking for automated screening". In: *Proc. 5th IEEE Int. Symp. Biomedical Imaging: From Nano to Macro*. May 2008, pp. 376–379. DOI: 10.1109/ISBI.2008.4541011.

[89] D. Padfield, J. Rittscher, and B. Roysam. "Coupled minimum-cost flow cell tracking for high-throughput quantitative analysis." eng. In: *Med Image Anal* 15.4 (2011), pp. 650–668. DOI: 10.1016/j.media.2010.07.006. URL: http://dx.doi.org/10.1016/j.media.2010.07.006.

[90] D. Padfield, J. Rittscher, N. Thomas, and B. Roysam. "Spatio-temporal cell cycle phase analysis using level sets and fast marching methods." eng. In: *Med Image Anal* 13.1 (2009), pp. 143–155. DOI: 10.1016/j.media.2008.06.018. URL: http://dx.doi.org/10.1016/j.media.2008.06.018.

[91] E. Parzen. "On Estimation of a Probability Density Function and Mode". English. In: *The Annals of Mathematical Statistics* 33.3 (1962), pp. 1065–1076. ISSN: 00034851. URL: http://www.jstor.org/stable/2237880.

[92] P. Perona and J. Malik. "Scale-space and edge detection using anisotropic diffusion". In: *Pattern Analysis and Machine Intelligence, IEEE Transactions on* 12.7 (1990), pp. 629–639. ISSN: 0162-8828. DOI: 10.1109/34.56205.

[93] F. Preteux. "Watershed and Skeleton by Influence Zones: A Distance-Based Approach". In: *Journal of Mathematical Imaging* 1 (1992), pp. 239–255.

[94] G. W. Pulford and B. F. L. Scala. "Multihypothesis Viterbi Data Association: Algorithm Development and Assessment". In: *IEEE Transactions on Aerospace and Electronic Systems* 46.2 (Apr. 2010), pp. 583–609. ISSN: 0018-9251. DOI: 10.1109/TAES.2010.5461643.

[95] X. Qi, F. Xing, D. J. Foran, and L. Yang. "Robust Segmentation of Overlapping Cells in Histopathology Specimens Using Parallel Seed Detection and Repulsive Level Set". In: *IEEE Transactions on Biomedical Engineering* 59.3 (Mar. 2012), pp. 754–765. ISSN: 0018-9294. DOI: 10.1109/TBME.2011.2179298.

[96] F. Raimondo, M. A. Gavrielides, G. Karayannopoulou, K. Lyroudia, I. Pitas, and I. Kostopoulos. "Automated evaluation of her-2/neu status in breast tissue from fluorescent in situ hybridization images". In: *IEEE Transactions on Image Processing* 14.9 (Sept. 2005), pp. 1288–1299. ISSN: 1057-7149. DOI: 10.1109/TIP.2005.852806.

[97] Y. Rathi, N. Vaswani, A. Tannenbaum, and A. Yezzi. "Tracking Deforming Objects Using Particle Filtering for Geometric Active Contours". In: *IEEE Transactions on Pattern Analysis and Machine Intelligence* 29.8 (2007), pp. 1470–1475. ISSN: 0162-8828. DOI: 10.1109/TPAMI.2007.1081.

[98] Y. Rathi, N. Vaswani, A. Tannenbaum, and A. Yezzi. "Particle filtering for geometric active contours with application to tracking moving and deforming objects". In: *2005 IEEE Computer Society Conference on Computer Vision and Pattern Recognition (CVPR'05)*. Vol. 2. 2005, pp. 2–9. DOI: 10.1109/CVPR.2005.271.

[99] N. Ray, S. T. Acton, and K. Ley. "Tracking leukocytes in vivo with shape and size constrained active contours." eng. In: *IEEE Trans Med Imaging* 21.10 (2002), pp. 1222–1235. DOI: 10.1109/TMI.2002.806291. URL: http://dx.doi.org/10.1109/TMI.2002.806291.

[100] R. Ronfard. "Region-based Strategies for Active Contour Models". In: *Int. J. Comput. Vision* 13.2 (Oct. 1994), pp. 229–251. ISSN: 0920-5691. DOI: 10.1007/BF01427153. URL: http://dx.doi.org/10.1007/BF01427153.

[101] G. Sapiro. *Geometric Partial Differential Equations and Image Analysis*. New York, NY, USA: Cambridge University Press, 2006. ISBN: 0521685079.

[102] R. E. Sequeira and F. J. Preteux. "Discrete Voronoi diagrams and the SKIZ operator: a dynamic algorithm". In: *IEEE Transactions on Pattern Analysis and Machine Intelligence* 19.10 (Oct. 1997), pp. 1165–1170. ISSN: 0162-8828. DOI: 10.1109/34.625128.

[103] J. A. Sethian. "A fast marching level set method for monotonically advancing fronts". In: *Proc. National Academy of Science USA* 93 (1996), pp. 1591–1595.

[104] J. Shah. "Uses of Elliptic Approximations in Computer Vision". In: *Variational Methods for Discontinuous Structures* (Jan. 1, 1996). DOI: 10.1007/978-3-0348-9244-5_3. URL: http://dx.doi.org/10.1007/978-3-0348-9244-5_3.

[105] H. Shen, G. Nelson, S. Kennedy, D. Nelson, J. Johnson, D. Spiller, R. H. White, and D. B. Kell. "Automatic Tracking of Biological Cells and Compartments using Particle Filters and Active Contours". In: *Chemometrics and Intelligent Laboratory Systems* 82.1-2 (2006), pp. 276–282.

[106] I. Smal and E. Meijering. "Quantitative comparison of multiframe data association techniques for particle tracking in time-lapse fluorescence microscopy." eng. In: *Med Image Anal* 24.1 (2015), pp. 163–189. DOI: 10.1016/j.media.2015.06.006. URL: http://dx.doi.org/10.1016/j.media.2015.06.006.

[107] I. Smal, I. Grigoriev, A. Akhmanova, W. J. Niessen, and E. Meijering. "Accurate estimation of microtubule dynamics using kymographs and variable-rate particle filters." eng. In: *Conf Proc IEEE Eng Med Biol Soc* 2009 (2009), pp. 1012–1015. DOI: 10.1109/IEMBS.2009.5333350. URL: http://dx.doi.org/10.1109/IEMBS.2009.5333350.

[108] I. Smal, I. Grigoriev, A. Akhmanova, W. J. Niessen, and E. Meijering. "Microtubule dynamics analysis using kymographs and variable-rate particle filters." eng. In: *IEEE Trans Image Process* 19.7 (2010), pp. 1861–1876. DOI: 10.1109/TIP.2010.2045031. URL: http://dx.doi.org/10.1109/TIP.2010.2045031.

[109] I. Smal, K. Draegestein, N. Galjart, W. Niessen, and E. Meijering. "Particle filtering for multiple object tracking in dynamic fluorescence microscopy images: application to microtubule growth analysis." eng. In: *IEEE Trans Med Imaging* 27.6 (2008), pp. 789–804. DOI: 10.1109/TMI.2008.916964. URL: http://dx.doi.org/10.1109/TMI.2008.916964.

[110] I. Smal, K. Draegestein, N. Galjart, W. Niessen, and E. Meijering. "Rao-Blackwellized marginal particle filtering for multiple object tracking in molecular bioimaging." eng. In: *Inf Process Med Imaging* 20 (2007), pp. 110–121.

[111] P. Soille. *Morphological Image Analysis: Principles and Applications*. 2nd ed. Secaucus, NJ, USA: Springer-Verlag New York, Inc., 2003. ISBN: 3540429883.

[112] J. A. S. Stanley Osher. "Fronts propagation with curvature dependant speed: Algorithm based on Hamilton-Jacobi Formulations". In: *Journal of Computational Physics* 79 (1988), pp. 12–49. DOI: 10.1016/0021-9991(88)90002-2.

[113] D. J. Stephens and V. J. Allan. "Light microscopy techniques for live cell imaging." eng. In: *Science* 300.5616 (2003), pp. 82–86. DOI: 10.1126/science.1082160. URL: http://dx.doi.org/10.1126/science.1082160.

[114] D. Sun, S. Roth, J. P. Lewis, and M. J. Black. "Learning Optical Flow". In: *Computer Vision – ECCV 2008: 10th European Conference on Computer Vision, Marseille, France, October 12-18, 2008, Proceedings, Part III*. Ed. by D. Forsyth, P. Torr, and A. Zisserman. Vol. 5304. Berlin, Heidelberg: Springer Berlin Heidelberg, 2008, pp. 83–97. ISBN: 978-3-540-88690-7. DOI: 10.1007/978-3-540-88690-7_7. URL: http://dx.doi.org/10.1007/978-3-540-88690-7_7.

[115] K. Thirusittampalam, M. J. Hossain, O. Ghita, and P. F. Whelan. "A Novel Framework for Cellular Tracking and Mitosis Detection in Dense Phase Contrast Microscopy Images". In: *IEEE Journal of Biomedical and Health Informatics* 17.3 (May 2013), pp. 642–653. ISSN: 2168-2194. DOI: 10.1109/TITB.2012.2228663.

[116] A. Tsai, A. Yezzi, and A. S. Willsky. "Curve evolution implementation of the Mumford-Shah functional for image segmentation, denoising, interpolation, and magnification". In: *IEEE Transactions on Image Processing* 10.8 (Aug. 2001), pp. 1169–1186. ISSN: 1057-7149. DOI: 10.1109/83.935033.

[117] C. Tsiotsios and M. Petrou. "On the choice of the parameters for anisotropic diffusion in image processing". In: *Pattern Recognition* 46.5 (2013), pp. 1369–1381. ISSN: 0031-3203. DOI: http://dx.doi.org/10.1016/j.patcog.2012.11.012. URL: http://www.sciencedirect.com/science/article/pii/S0031320312004748.

[118] R. K. V. Casseles and G. Sapiro. "Geodesic Active Contours". In: *International Journal of Computer Vision* 22.1 (1997). 1997 Kluwer Academic Publishers., pp. 61–79.

[119] G. Vegas-Snchez-Ferrero, G. Ramos-Llordn, R. de Luis-Garca, A. Tristn-Vega, and S. Aja-Fernndez. "Anisotropic diffusion filtering for correlated multiple-coil MRI." In: *Conference proceedings : ... Annual International Conference of the IEEE Engineering in Medicine and Biology Society. IEEE Engineering in Medicine and Biology Society. Annual Conference* 2013 (2013), pp. 2956–2959. ISSN: 1557-170X. DOI: 10.1109/EMBC.2013.6610160.

[120] L. A. Vese and T. F. Chan. "A multiphase level set framework for image segmentation using the mumford shah model". In: *International journal of computer vision* 50.3 (2002). 2002 Kluwer Academic Publishers. Manufactured in The Netherlands., pp. 271–293.

[121] L. Vincent and P. Soille. "Watersheds in Digital Spaces: An Efficient Algorithm Based on Immersion Simulations". In: *IEEE Trans. Pattern Anal. Mach. Intell.* 13.6 (June 1991), pp. 583–598. ISSN: 0162-8828. DOI: 10.1109/34.87344. URL: http://dx.doi.org/10.1109/34.87344.

[122] C. Wählby, I.-M. Sintorn, F. Erlandsson, G. Borgefors, and E. Bengtsson. "Combining intensity, edge and shape information for 2D and 3D segmentation of cell nuclei in tissue sections". In: *Journal of Microscopy* 215.1 (2004), pp. 67–76. ISSN: 1365-2818. DOI: 10.1111/j.0022-2720.2004.01338.x. URL: http://dx.doi.org/10.1111/j.0022-2720.2004.01338.x.

[123] A. Wedel and D. Cremers. "Optical Flow Estimation". In: *Stereo Scene Flow for 3D Motion Analysis* (Jan. 1, 2011). DOI: 10.1007/978-0-85729-965-9_2. URL: http://dx.doi.org/10.1007/978-0-85729-965-9_2.

[124] J. Weickert. "A review of nonlinear diffusion filtering". In: *Scale-Space Theory in Computer Vision: First International Conference, Scale-Space'97 Utrecht, The Netherlands, July 2–4, 1997 Proceedings*. Ed. by B. ter Haar Romeny, L. Florack, J. Koenderink, and M. Viergever. Berlin, Heidelberg: Springer Berlin Heidelberg, 1997, pp. 1–28. ISBN: 978-3-540-69196-9. DOI: 10.1007/3-540-63167-4_37. URL: http://dx.doi.org/10.1007/3-540-63167-4_37.

[125] J. Weickert. *Anisotropic Diffusion in Image Processing*. ECMI Series. Stuttgart: Teubner, 1998. URL: http://www.mia.uni-saarland.de/weickert/book.html.

[126] J. Weickert. "Scale-Space Theory in Computer Vision". In: Lecture notes in computer science 1252. Springer, 2005. Chap. A review of nonlinear diffusion filtering, pp. 1–28.

[127] C. Xu and J. L. Prince. "Snakes, shapes, and gradient vector flow". In: *IEEE Transactions on Image Processing* 7.3 (1998), pp. 359–369. DOI: 10.1109/83.661186. URL: http://dx.doi.org/10.1109/83.661186.

[128] X. Yang, H. Li, and X. Zhou. "Nuclei Segmentation Using Marker-Controlled Watershed, Tracking Using Mean-Shift, and Kalman Filter in Time-Lapse Microscopy". In: *Circuits and Systems I: Regular Papers, IEEE Transactions on* 53.11 (2006), pp. 2405–2414. ISSN: 1549-8328. DOI: 10.1109/TCSI.2006.884469.

[129] X. Yang, H. Li, X. Zhou, and S. Wong. "Automated segmentation and tracking of cells in time-lapse microscopy using watershed and mean shift". In: *Proc. Int. Symp. Intelligent Signal Processing and Communication Systems*. Dec. 2005, pp. 533–536. DOI: 10.1109/ISPACS.2005.1595464.

[130] A. Yezzi, A. Tsai, and A. Willsky. "A statistical approach to snakes for bimodal and trimodal imagery". In: *Proc. Seventh IEEE Int Computer Vision Conf. The*. Vol. 2. 1999, pp. 898–903. DOI: 10.1109/ICCV.1999.790317.

[131] Y. L. You, W. Xu, A. Tannenbaum, and M. Kaveh. "Behavioral analysis of anisotropic diffusion in image processing." eng. In: *IEEE Transactions on Image Processing* 5.11 (1996), pp. 1539–1553. DOI: 10.1109/83.541424. URL: http://dx.doi.org/10.1109/83.541424.

[132] B. Zhang, C. Zimmer, and J. C. Olivo-Marin. "Tracking fluorescent cells with coupled geometric active contours". In: *Proc. 2nd IEEE Int. Symp. Biomedical Imaging: Nano to Macro (IEEE Cat No. 04EX821)*. Vol. 1. Apr. 2004, pp. 476–479. DOI: 10.1109/ISBI.2004.1398578.

[133] X. Zhou, F. Li, J. Yan, and S. T. C. Wong. "A Novel Cell Segmentation Method and Cell Phase Identification Using Markov Model". In: *IEEE Transactions on Information Technology in Biomedicine* 13.2 (2009), pp. 152–157. ISSN: 1089-7771. DOI: 10.1109/TITB.2008.2007098.

[134] S. C. Zhu and A. Yuille. "Region competition: unifying snakes, region growing, and Bayes/MDL for multiband image segmentation". In: *IEEE Transactions on Pattern Analysis and Machine Intelligence* 18.9 (Sept. 1996), pp. 884–900. ISSN: 0162-8828. DOI: 10.1109/34.537343.

[135] C. Zimmer and J. C. Olivo-Marin. "Coupled parametric active contours". In: *IEEE Transactions on Pattern Analysis and Machine Intelligence* 27.11 (Nov. 2005), pp. 1838–1842. ISSN: 0162-8828. DOI: 10.1109/TPAMI.2005.214.

[136] C. Zimmer, E. Labruyère, V. Meas-Yedid, N. Guillén, and J.-C. Olivo-Marin. "Segmentation and tracking of migrating cells in videomicroscopy with parametric active contours: a tool for cell-based drug testing." eng. In: *IEEE Trans Med Imaging* 21.10 (2002), pp. 1212–1221. DOI: 10.1109/TMI.2002.806292. URL: http://dx.doi.org/10.1109/TMI.2002.806292.